PHYSICAL AND CHEMICAL ADHESION OF COMPLEX STRUCTURED BIOMATERIAL PARTICLES: POLLEN EXINE AND CELLULOSE NANOCRYSTAL

A Dissertation
Presented to
The Academic Faculty

by

Zihao Qu

In Partial Fulfillment
of the Requirements for the Degree
Doctor of Philosophy in the
School of Chemical and Biomolecular Engineering

Georgia Institute of Technology
December 2017

PHYSICAL AND CHEMICAL ADHESION OF COMPLEX STRUCTURED BIOMATERIAL PARTICLES: POLLEN EXINE AND CELLULOSE NANOCRYSTAL

Approved by:

Dr. J. Carson Meredith, Advisor
School of Chemical and
Biomolecular Engineering
Georgia Institute of Technology

Dr. Peter J. Ludovice
School of Chemical and
Biomolecular Engineering
Georgia Institute of Technology

Dr. Sven H. Behrens
School of Chemical and
Biomolecular Engineering
Georgia Institute of Technology

Dr. Min Zhou
School of Mechanical Engineering
Georgia Institute of Technology

Dr. Elsa Reichmanis
School of Chemical and
Biomolecular Engineering
Georgia Institute of Technology

Date Approved: [October 24th, 2017]

This work is dedicated to my family.

ACKNOWLEDGEMENTS

I would like to thank my family for giving me the courage and support needed to pursue a Ph.D. degree, I would not be where I am today without your endless love. I would like to thank my mother and father for teaching me to always have a positive altitude, for allowing me to grow up with great freedom and choose my own path. Their encouragement and support have always been there whenever I need. I would like to thank my elder brother, Qu Yang. I feel so lucky to have a brother like you, who always give support and protection throughout my life. Finally, I would like to thank my grandmother, for unconditional love, teaching me to have a strong will, and watching over me from heaven.

I would like to sincerely thank my advisor, Dr. Carson Meredith, for all his guidance, patience and inspiration throughout my journey as a graduate student at Georgia Tech. I feel fortunate to have had him as my advisor. He set a great example for me to learn, with his great personality, high work ethic and strong integrity. I am especially grateful to his support and concern when I had to go back home for my family.

I would like to thank my committee members. Dr. Sven Behrens, Dr. Elsa Reichmanis, Dr. Peter J. Ludovice, and Dr. Min Zhou for their support and valuable feedback throughout my Ph.D. education. Special appreciation is given to Dr. Meisha Shofner, Dr. Greg Schueneman and Dr. Eric Mintz for their regular support and collaboration. Additionally, I would like to acknowledge the organizations that provided funding for my research: the U.S. Air Force Office for Scientific Research, and the U.S.D.A. Forest Products Laboratory

I would like to thank all the past and current members of the Meredith research group, Dr. Haisheng Lin, Dr. Ismael Gomez, Dr. Jie Wu, Dr. Zifu Li, Dr. Oluwatimilehin Fadiran, Dr. Natalie Girouard, Dr. Yi Zhang, Dr. Donglee Shin, Songcheng Wang, Chinmay Satam, Scott Essenmacher, Ezgi M. Dogan Guner, for sharing their knowledge and support along with enjoyable moments.

Last but not least, I would like to thank my girlfriend, Xi Yizhao, whose love and support have made this work possible.

TABLE OF CONTENTS

LIST OF TABLES

LIST OF FIGURES

SUMMARY

Micro- and nano-particle adhesion plays an important role in many industrial fields, for example, in microelectromechanical systems (MEMS, affecting fabrication yield and operation), in printing (transfer toner particles onto substrates), in coating and paints applications (adhesion of powder paint), or in composite materials (reduce filler-filler adhesion and enhance filler-matrix adhesion). In all of these examples, the particle-particle and particle-substrate interactions govern many aspects of process and product design. These complex interactions are determined by material properties (for example, the Hamaker constant and elastic modulus), particle size and shape, surface properties (e.g., surface energy and roughness), external load, humidity and electrostatic charges. Particle-particle and particle-substrate adhesion have been the focus of intense study; however, they have not been fully understood. The purposes of this study are to 1) understand particle-particle adhesion mechanisms of complex structured microparticles, and 2) tailor particle-polymer matrix adhesion for enhanced mechanical performance of polymer composites. Two biomaterial particles, micro-sized pollen grains and nano-sized cellulose nanocrystals (CNCs), were used as model particles for these two purposes, respectively.

In this work, the morphology effect of pollen exine on pollen-pollen interaction was characterized with atomic force microscopy to reveal the unique interaction mechanism. A hybrid interaction model was developed to capture the effect of the micro-structured morphology. Meanwhile, the elastic modulus of pollen exine was analyzed for the first time to understand the effect of mechanical properties on pollen-pollen interaction. In the second part of this work, cellulose nanocrystals (CNCs) were chemically modified and

rendered acrylic functional groups on the surfaces. The particle-matrix interaction was tuned to utilize the reinforcing effect of the modified CNCs. Three different processing methods were developed to optimize the reinforcing benefits from the modified CNCs.

Overall, this work presents new insights for effects of surface physical (morphology and mechanical property) and chemical properties on particle-particle and particle-matrix adhesion. Pollen grains were investigated as a model of complex structured microparticles, and a unique particle-particle interaction due to the complex morphology was revealed. The elastic moduli of pollen shells were firstly characterized with direct measurements. In the second part of this work, a chemical modification route was developed for cellulose nanocrystals to improve the particle-matrix adhesion and compatibility. The results of his work provided new considerations for material applications including paints, coatings, drug delivery, and composites, among others.

CHAPTER 1. INTRODUCTION

1.1 Background

Particles are all around us in the environment in great abundance, including but not limited to pollens, dusts, bacteria, fibers, metals, metal oxides, etc. They are related to many natural phenomena like pollination process[1], surface contamination[2, 3] and allergen transportation[4, 5]. Particles are also often involved in various industrial processes, such as pharmaceutical industry[6], coating and paints industry[7], printing industry[8], and composite material industry[9], etc. Particle-particle and particle-surface adhesion are of great importance in these natural phenomena and industry processes. For example, in microelectromechanical system (MEMS), particle-surface adhesion has a dramatic effect on the performance of MEMS device and is a major fabrication yield loss factor.[10] In pharmaceutical industry, particle-particle adhesion has a great influence on powder handling process such as granulation, milling and powder inhaled drugs.[6] In composite materials, good particle-matrix adhesion enhances tensile strength dramatically.[11] Complex particle-particle and particle-surface interactions are determined by material properties (for example, the Hamaker constant and elastic modulus), particle size and shape, surface properties (surface chemistry and roughness), external load, humidity and electrostatic charges, etc. Both physical and chemical interactions can affect particle adhesion. Physical interactions include van der Waals forces, mechanical interlocking, and electrostatic forces. Chemical interactions include ionic forces, covalent bonding and hydrogen bonding. Although particle-particle and particle-surface adhesion have gained intense investigations, there is still a large blank field to be explored on both physical and

chemical aspects of adhesion. For physical adhesion, one example is that the adhesion between smooth microparticles with simple shape (spheres, cylinders and cones) has been well studied and predicted with either experimental or computational method.[12] [13-16] However, the adhesion of microparticles with complex morphology or irregular shape is still unclear. Another example for chemical aspect of adhesion, material scientists keep seeking ways to tailor particle-matrix adhesion to continuously improve properties of composite materials.[11, 12, 17, 18] Therefore, this work aims to explore both physical and chemical aspects of micro/nano particle adhesion. Two bio-particles with great emerging potentials in various application, pollen and cellulose nanocrystals (CNCs), were studied. Herein, we introduce some backgrounds and prior researches of particle adhesion, pollen grains, and CNCs. In section 2, basic physical principles of adhesion are discussed. In section 3, properties of pollen grains are discussed in terms of structure, chemistry, mechanical properties and applications. In section 4, basic background of CNCs and CNCs/polymer composites are introduced.

1.2 Basic physical principles of adhesion

1.2.1 Dry adhesion based on van der Waals approach

The adhesion between microparticles can be generally classified into two categories: dry adhesion dominated by van der Waals (vdW) force[19]， and wet adhesion governed by capillary force and viscous force[20]. Some other forces may also give contributions to either dry or wet adhesion, such as electrostatic force and hydrogen bonding[21, 22]. Although vdW force is usually much smaller than hydrogen bonding, ionic bonding or covalent bonding, it makes the most contributions to the attractive forces

between surface and micro/nano-sized particles, due to its longer interaction range (0.2~10 nm) than the other inter- or intramolecular bondings (0.1~0.2 nm)[22, 23]. VdW forces are the main source of dry adhesion between neutral mircoparticles in air, as well as the adhesion of many insects and reptiles that is governed by nano- to micro-scale contacts of fibrillar structures, on arbitrary surfaces in nature[19, 24]. The total vdW forces consist of three contributions: permanent dipole-dipole (Keesom force), dipole-induced dipole (Debye force) and induced-induced dipole (London dispersion force) interaction. London dispersion forces make the most important contribution, since they are always present.

In order to predict the dry adhesion force based on vdW forces, especially dispersion forces, different models were developed. In 1937, Hamaker investigated the adhesion between two spherical particles. By assuming pairwise non-retarded additivity of the interaction energy, the vdW interaction was computed by summing the energies of all atoms in one particle with all the atoms in the other, and thus obtain the adhesion force (or adhesion energy) as a function of the diameters and the distance separating particles[13]. According to Hamaker's theory, the vdW force between two spherical particles can be derived in terms of the conventional Hamaker constant:

$$F_{adh} = \frac{-A_{132}}{6D^2}\frac{R_1 R_2}{R_1 + R_2} \tag{1-1}$$

$$A = \pi^2 C \rho_1 \rho_2 \tag{1-2}$$

Where A_{132} is the non-retarded Hamaker constant, which represents the interacting strength between particle 1 and 2 consisting of atoms with induced dipoles across a medium 3; R is the radius of the interacting particles, D is the cutoff separation distance between two

contacting particles, which is approximated as 0.165 nm,[25] C is the London-van der Waals constant, ρ is the number density of the atoms in the two particles. Although the adhesion force is negatively proportional to D^2 as equation 1-1 suggested, it begins to decay more rapidly at distances beyond about 5 nm due to the retardation effects[23] (Figure 1.1). Theoretically, Hamaker's method can be applied to arbitrary geometries. Figure 1.2 shows the vdW interaction and force between common geometries.

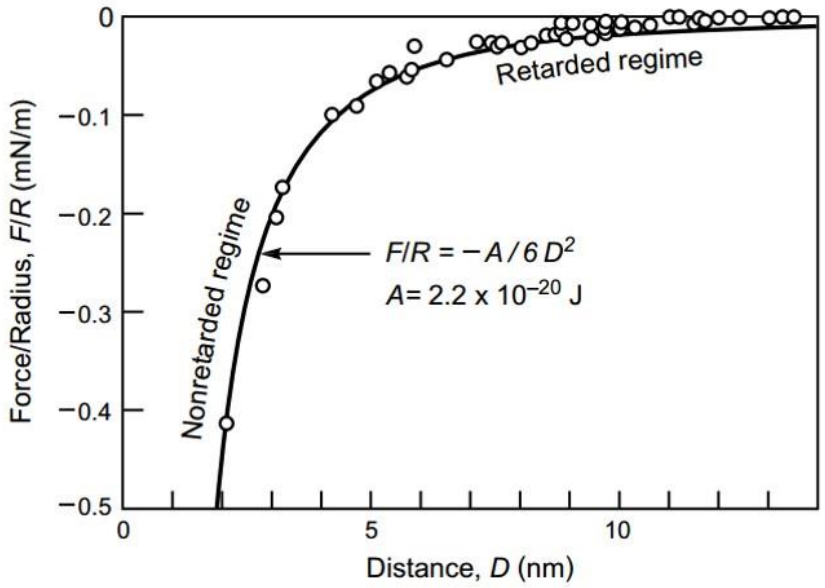

Figure 1.1 Attractive van der Waals force F between two curved mica surfaces of radius $R \approx 1\ cm$ measured in water and aqueous electrolyte solutions. It showed retardation effect beyond about 5 nm. This figure is taken from reference [23].

Geometry of bodies with surfaces D apart ($D \ll R$)		Van der Waals Interaction*	
		Energy, W	Force, $F = -dW/dD$
Two atoms or small molecules	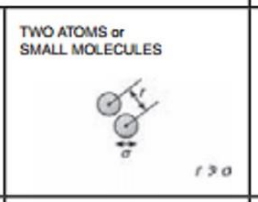	$-C/r^6$	$-6C/r^7$
Two flat surfaces (per unit area)	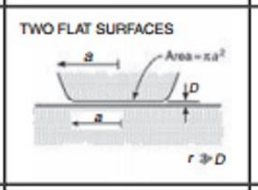	$W_{flat} = -A/12\pi D^2$	$-A/6\pi D^3$
Two spheres or macromolecules of radii R_1 and R_2	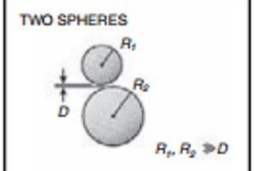	$\frac{-A}{6D}\left(\frac{R_1R_2}{R_1+R_2}\right)$	$\frac{-A}{6D^2}\left(\frac{R_1R_2}{R_1+R_2}\right)$ Also $F = 2\pi\left(\frac{R_1R_2}{R_1+R_2}\right)W_{flat}$
Sphere or macromolecule of radius R near a flat surface	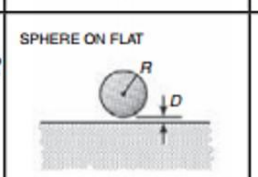	$-AR/6D$	$-AR/6D^2$ Also $F = 2\pi RW_{flat}$
Two parallel cylinders or rods of radii R_1 and R_2 (per unit length)	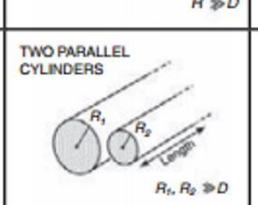	$\frac{-A}{12\sqrt{2}D^{3/2}}\left(\frac{R_1R_2}{R_1+R_2}\right)^{1/2}$	$\frac{-A}{8\sqrt{2}D^{5/2}}\left(\frac{R_1R_2}{R_1+R_2}\right)^{1/2}$
Cylinder of radius R near a flat surface (per unit length)	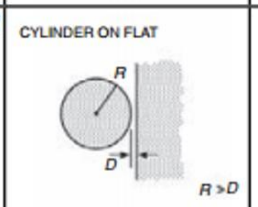	$\frac{-A\sqrt{R}}{12\sqrt{2}D^{3/2}}$	$\frac{-A\sqrt{R}}{8\sqrt{2}D^{5/2}}$
Two cylinders or filaments of radii R_1 and R_2 crossed at 90°	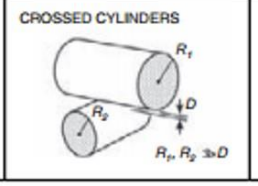	$\frac{-A\sqrt{R_1R_2}}{6D}$	$\frac{-A\sqrt{R_1R_2}}{6D^2}$ Also $F = 2\pi\sqrt{R_1R_2}W_{flat}$

Figure 1.2 Van der Waals interaction energy and force between macroscopic bodies of common geometries. This figure is taken from reference [23].

However, Hamaker's method and definition of *A* in equation 1-2 ignore the influence of neighbouring atoms on the interaction between any pair of atoms. In order to avoid the problem of additivity, in 1956, Lifshitz reported another method, where the atomic structure was neglected and the contacting bodies were treated as continuous media.[26] Lifshitz's method is based on quantum field theory. Hamaker constant is derived as a function of the dielectric constants of contacting bodies and medium in equation 1-3:

$$A \approx \frac{3}{4}kT\left(\frac{\varepsilon_1-\varepsilon_3}{\varepsilon_1+\varepsilon_3}\right)\left(\frac{\varepsilon_2-\varepsilon_3}{\varepsilon_2+\varepsilon_3}\right)+\frac{3}{4}\frac{h}{\pi}\int_{\nu_1}^{\infty}\left(\frac{\varepsilon_1(iv)-\varepsilon_3(iv)}{\varepsilon_1(iv)+\varepsilon_3(iv)}\right)\left(\frac{\varepsilon_1(iv)-\varepsilon_3(iv)}{\varepsilon_1(iv)+\varepsilon_3(iv)}\right)dv \quad (1\text{-}3)$$

where ε_1, ε_2 and ε_3 are the static dielectric constants of the three media, *ε(iv)* are the values of ε at imaginary frequencies, and $\nu_n = (2\pi kT/h)n = 4\times10^{13}n\ s^{-1}$ at 300K. It is worth noting that all the expressions in Figure 1.2 for the interaction energies and forces remain unchanged even within the frame work of continuum theories.

When surface roughness, i.e. the asperities on a smaller scale compared to the characteristic length of the contacting bodies, are considered, the problem is more complicated than the adhesion between particles with common simple geometries. It is well-known that surface roughness can reduce dry adhesion and increase the standard deviation of the pull-off force measured by atomic force microscopy(AFM) [27-29]. Given the universality of Hamaker's method for arbitrary geometries, two models were developed based on Hamaker theory to take the effect of surface roughness into account. Rumpf treated the surface roughness as hemispherical asperities, of which the centre is located at the surface[30]. However, Rabinovich et al. found that Rumpf's model is not accurate,

since the center of asperities are usually not at the surface. Instead, they introduced the root-mean-square (RMS) roughness into Rumpf's model with the center of asperities lying on the surface. Rabinvoich's model was further modified by introducing new parameters like the breadth of asperities and the second order roughness.[31, 32] However, all of these models were specifically developed for the nanoscale roughness of the surface, which is much smaller than the systematic scale. That means, when the asperity size approaches the particle size itself, these models are not sufficient to describe the adhesion between these particles anymore. In addition, few models considered the roughness on both particles and surfaces, whereas the roughness is not limited on the only one of the contacting particles or surfaces.

1.2.2 Dry adhesion based on contact mechanics

In 1882, Heinrich Hertz developed a contact model to describe the deformation (δ_{Hertz}) versus contact radius (a) between two elastic spheres[33]:

$$\delta_{Hertz} = \frac{a^2}{R} \tag{1-3}$$

where (R) is the radius of the spheres. The relationship between the applied force (F) and the contact radius (a) is as follows:

$$F_{Hertz} = \frac{4Ea^3}{3R} \tag{1-4}$$

where E is the reduced Young's modulus:

$$E = (\frac{1 - v_1^2}{E_1} + \frac{1 - v_2^2}{E_2})^{-1} \quad (1\text{-}5)$$

where E_1, E_2 are the Young's moduli, and v_1, v_2 are the Poisson ratios of two spheres, respectively. In Hertzian theory, the contact area is zero when there is no external load, since the intermolecular forces between contacting bodies were ignored. Derjaguin firstly considered the adhesion of elastic particles with their deformation[34]. In, 1971, Johnson, Kendall, and Roberts (JKR) developed a model based on the Hertz model, and assumed that the intermolecular forces act only within the contact area (Figure 1.3a).[35] The authors deduced that the force of adhesion between a sphere and a flat surface is determined by the following equation:

$$F_{JKR} = \frac{3}{2}\pi R W_{12} \quad (1\text{-}6)$$

where F_{JKR} is the adhesion, R is the radius of sphere, and W_{12} is work of adhesion. An alternative approach was suggested by Derjaguin, Muller and Toporov (DMT)[36]. The DMT model considers the action of van der Waals forces along the contact area (Figure 1.3b). In this case, equation 1-6 becomes:

$$F_{JKR} = 2\pi R W_{12} \quad (1\text{-}7)$$

In 1992, an intermediate model was developed by Maugis [37]. The Maugis model considers the effect of surface forces in a ring zone surrounding the Hertzian region of contact. A factor λ was introduced as:

$$\lambda = 2\sigma_0(\frac{R}{\pi W_{12}E^2})^{1/3} \quad (1\text{-}7)$$

where the JKR model applies at λ>5 and the DMT model applies at λ>0.1. Nevertheless, all these Hertz-based model didn't take the influence of separation distance into account for adhesion. When contact surfaces have roughness or complex morphology, the assumption of complete contact doesn't stand any more. Therefore, these Hertz-based model were not valid for rough or structured surfaces. Instead, the Hamaker method is often used to deal with rough surfaces and complex geometries.

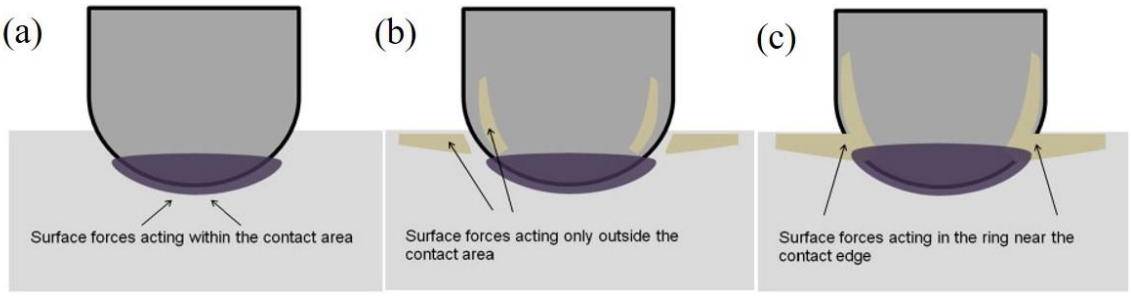

Figure 1.3 Regions of surface forces action according to (a) the JKR model, (b) the DMT model, and (c) Maugis model. Figures are taken from reference [33].

1.2.3 Adhesion theories in composite materials

For enhanced polymer composite performance, a good dispersion of fillers in polymer matrix and strong filler-matrix adhesion are desired. The degree of particle dispersion is highly dependent on the surface chemistry of particles and particle-polymer matrix interaction. From a surface energy view, good adhesion can be achieved with optimized interfacial energy of the particle and polymer matrix, as well as sufficient wetting of the particle with the polymer. As shown in Figure 1.4, the interfacial adhesion

between two bodies of the same material can be considered as the energy required to create two new interfaces of a homogeneous material (work of cohesion, W_c), and the interfacial adhesion between two bodies of different materials can be considered as the energy required to separate two dissimilar surfaces (work of adhesion, *Wa*). The relation between work of cohesion/adhesion and surface energy can be presented as[38]:

$$W_c = W_{11} = 2\gamma_1 \tag{1-8}$$

$$W_a = W_{12} = \gamma_1 + \gamma_2 - \gamma_{12} \tag{1-9}$$

Where in as composite system, γ_1 represents the surface energy of the polymer, γ_2 represents the surface energy of the particle, and γ_{12} represents the interfacial energy of the particle/polymer interface. It is worth noting based on equation 1-9 that minimizing the particle/polymer interfacial energy would give a maximum work of adhesion. Previous studies have showed that the minimum value of the interfacial energy can be achieved by equating the surface energy of the particle and polymer. Given the surface energy of certain polymers, the surface energy of filler particles is often optimized to enhance the interfacial adhesion by modifying the filler surface chemistry.

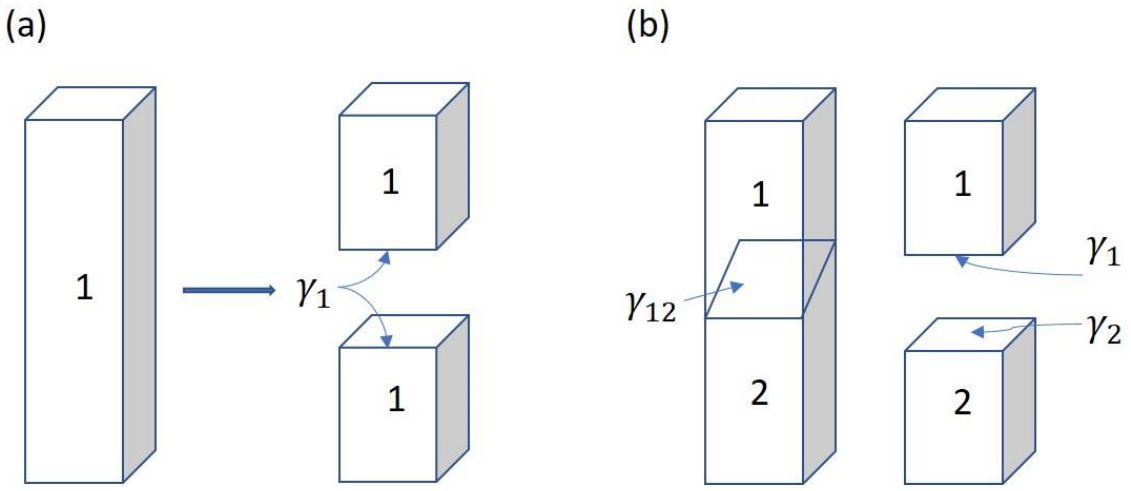

Figure 1.4 A schematic illustration representing the theoretical work of cohesion (a); and adhesion (b).

In addition to the work of adhesion, sufficient wetting of the polymer solution/melt on filler particles is also critical to achieve an intimate interfacial contact. Spreading coefficient is usually used to describe the wetting behavior as:

$$S_{12} = \gamma_2 - \gamma_1 - \gamma_{12} = W_{12} - W_{11} \quad (1\text{-}10)$$

A positive or zero spreading coefficient would result in spontaneous spreading, while a negative spreading coefficient leads to insufficient spreading. Therefore, maximizing the surface energy of the particle (γ_2), and minimizing the surface energy of the polymer solution/melt and the particle/polymer interfacial energy would lead to the most favorable wetting condition. However, comparing equation 1-9 with 1-10, there is a tradeoff between the maximum work of adhesion (Wa) by maximizing the surface energy of the polymer (γ_1), and the maximum spreading coefficient by minimizing the surface energy of the polymer (γ_1). Even though, minimizing the interfacial energy (γ_{12}) and maximizing the surface energy of the particle (γ_2) would result in favorable adhesion and wetting condition.

A common method to analyze the surface energy and work of adhesion of polymer surface is by employing the Van Oss Chaudhury-Good method (three-liquid acid-base method).[39] In the Van Oss-Good theory, the work of adhesion is analyzed with a van der Waals (γ^{vW}), acidic (γ^{+}), and basic (γ^{-}) contribution. The contact angle of three test liquids are measured on the solid surface of interest, including an apolar liquid and two bipolar liquid, which have similar contributions to the acidic and basic components of surface energy. Thus, the following equation can be used to calculate the solid surface energy:

$$W_a = \gamma_l + \gamma_s - \gamma_{ls} = 2(\gamma_s^{vW}\gamma_l^{vW})^{\frac{1}{2}} + 2(\gamma_s^{+}\gamma_l^{-})^{\frac{1}{2}} + (\gamma_s^{-}\gamma_l^{+})^{\frac{1}{2}} \quad (1\text{-}11)$$

$$W_a = \gamma_l(1 + cos\theta) \quad (1\text{-}12)$$

Three equations can be generated based on the surface tensions and contact angles of three test liquids on the solid surface. The dispersive, acid and base component of the surface energy of the solid surface can be determined. Then, the total surface energy is given by:

$$\gamma_s = \gamma_s^{vW} + 2(\gamma_s^{+}\gamma_s^{-})^{\frac{1}{2}} \quad (1\text{-}13)$$

1.3 Pollen exine as a model particle with complex microstructured morphology

1.3.1 Pollen grains structure

Pollen grains carry male gametes for plant reproduction. The size of pollen grains typically ranges from 5 microns to larger than 200 microns[40]. Pollen grains have evolved a highly chemical and thermal resistant shell, varied surface features, and pollenkitt, a liquid substance on the surface, to promote transmission and germination. Mature pollen

grains possess a number of extracellular and intracellular features as shown in Figure 1.5, which can be divided into three domains from outside to inside: 1) pollenkitt, 2) exine and 3) intine. Pollenkitt is a viscous adhesive coating on pollen shells, which is mainly located in the cavities and surface of the exine. It is known to provide protections for pollen against water loss and facilitate pollen dispersal. Beneath the exine, there is a layer called intine, which is primarily composed of cellulose.[41] The most of the interior of the pollen grain is a large vegetative cell.

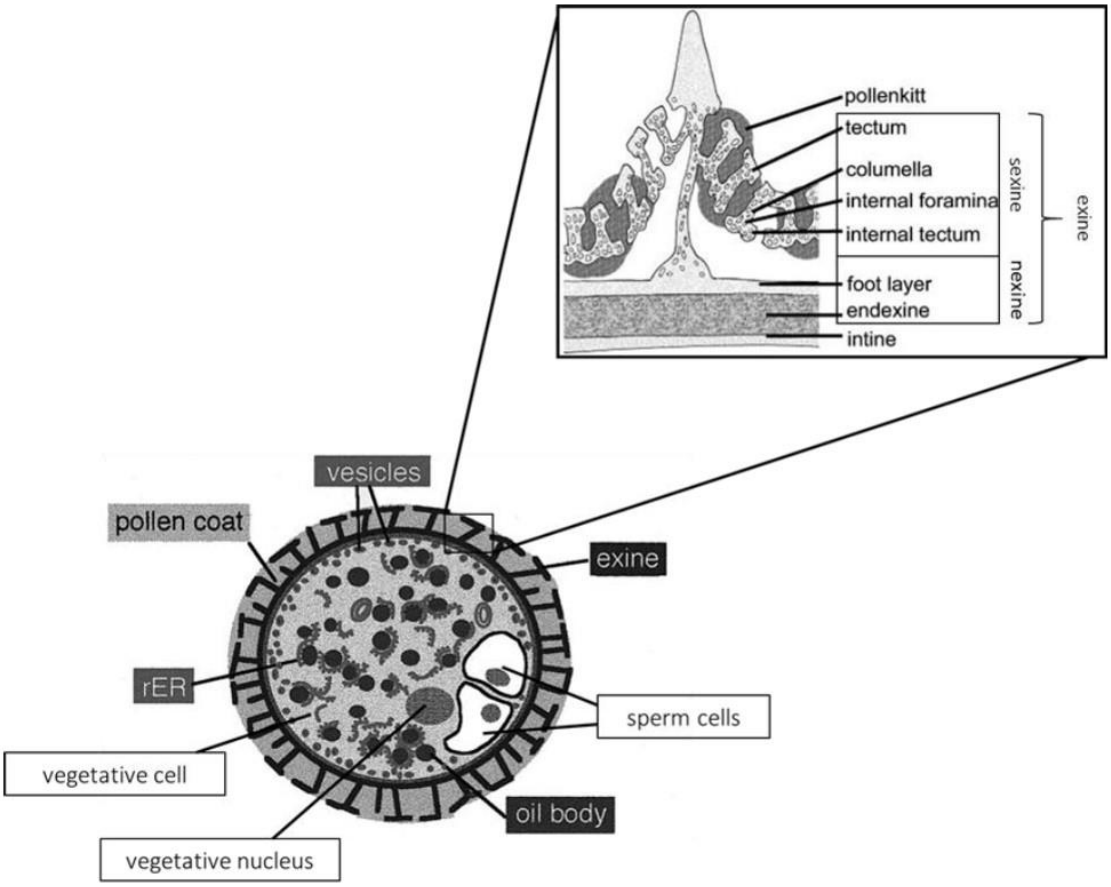

Figure 1.5 Ultrastructure of a typical mature pollen grain. Extracellular features include the inner intine, outer exine, and pollen coat (pollenkitt) filling the cavities of the exine sculpture. The image is taken from reference [42, 43].

The most interesting domain is exine, i.e. the outer pollen wall. The exine layer exhibits a great diversity of surface morphology and intricate sculptured patterns. It is believed that these evolutionary-optimized surface structures are critical for successful dispersal and transport. The exine wall of anemophilous (wind-aided dispersal) pollen species is often modified to enhance buoyancy. While the exine wall of entomophilous (insect dispersal) and zoophilous (vertebrate dispersal) pollen species often bears surface spines to enhance the adhesion[40]. Recently, the morphology effect of pollen exine on pollen-substrate adhesion has gained intense investigations. Thio et al. studied the adhesive behavior of ragweed (*A. artemisiifolia*) pollen on common indoor surfaces[44]. It was proven that van der Waals foces dominates the pollen adhesion on those studied surfaces. In addition, it was pollen spines which mainly contacted with surfaces, and the total adhesion scaled with the number of spine contacts. Lin et al. performed quantitative studies of the effects of exine surface structures and pollenkitt on pollen adhesion[45]. The results indicated that with pollenkitt removed, pollen adhesion is scalable with the tip radius of the pollens surface features (spines or rods). In addition, the adhesion of clean pollens is independent of surface chemistry. In another work by Lin et al., the species-specific morphology of pollen grains was demonstrated to facilitate the pressure-sensitive adhesion with plant stigma, which is critical for the pollination process[46]. Moreover, the morphology of pollen exine was utilized as bio-template for fabricating metal-oxide magnetic replicas[47],[48] magnetic-core particles[49] and metallized shells[50] with unique combinations of multimodal adhesion and optical properties.

Although the morphology effect of pollen exine on pollen-surface interaction has been studied, there exist no quantitative studies of the morphology effect on pollen-pollen

interaction. Furthermore, the ornamentation feature on pollen exine presents greater size than common surface roughness, and bears complex hierarchical structures, which are hard to be captured by existing adhesion models.

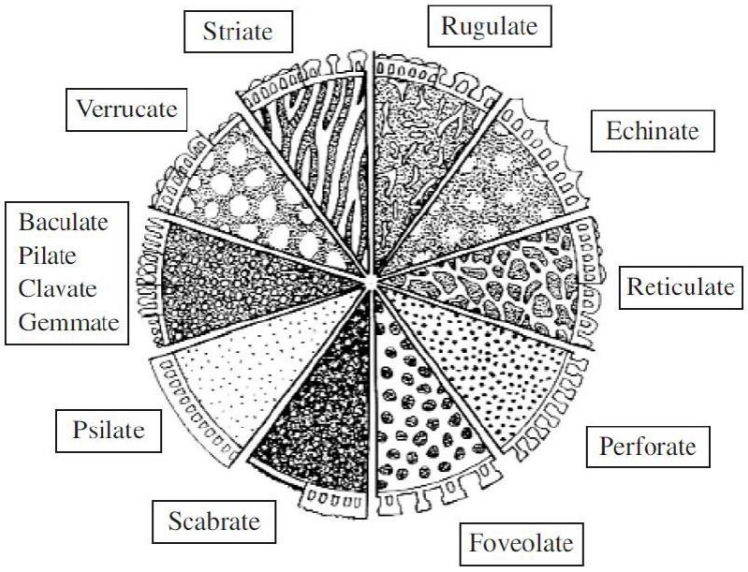

Figure 1.6 Surface sculpturing elements of pollen taken from reference [51].

1.3.2 Pollen exine chemistry

The exine layer of pollen grains is composed of sporopollenin. It has been demonstrated that sporopollenin is insoluble to known solvents and extremely resistant to non-oxidative physical, biological and chemical degradation[52]. Sporopollenin is a generic term for the constituents of exine and may kinds of spores. Distinct NMR spectra of the exines from different plant species indicate that sporopollenin from different pollen species are distinct substances[53]. Therefore, sporopollenin is a class of biopolymers rather than a specific macromolecule. Due to the insolubility of sporopolleinin in most acids and solvents, the chemical analysis of sporopollenin is limited to solid state techniques. Many efforts have been taken to unveil the structure of sporopollenin with

FTIR, solid state NMR and pyrolysis techniques. FTIR spectra suggest that the main structure of sporopollenin is a simple aliphatic polymer with aromatic and conjugated groups in the side chains[54]. Phenols are identified specifically trough the detection of 4-hydroxy-cinnamic acid from NMR spectra[55]. Alkyl chains containing at least ten CH_2 groups are detected and the polymers are linked via ether bridges[56]. Pyrolysis GC-MS indicated the presence of both p-coumaric acid and ferulic acid[57]. Solid state NMR and pyrolysis results indicated a tentative structure for sporopollenin, shown in Figure 1.7, in which long-chain (C_{24}-C_{28}) highly aliphatic units form the backbone of sporopollenin with cinnamic acids as cross-linking units

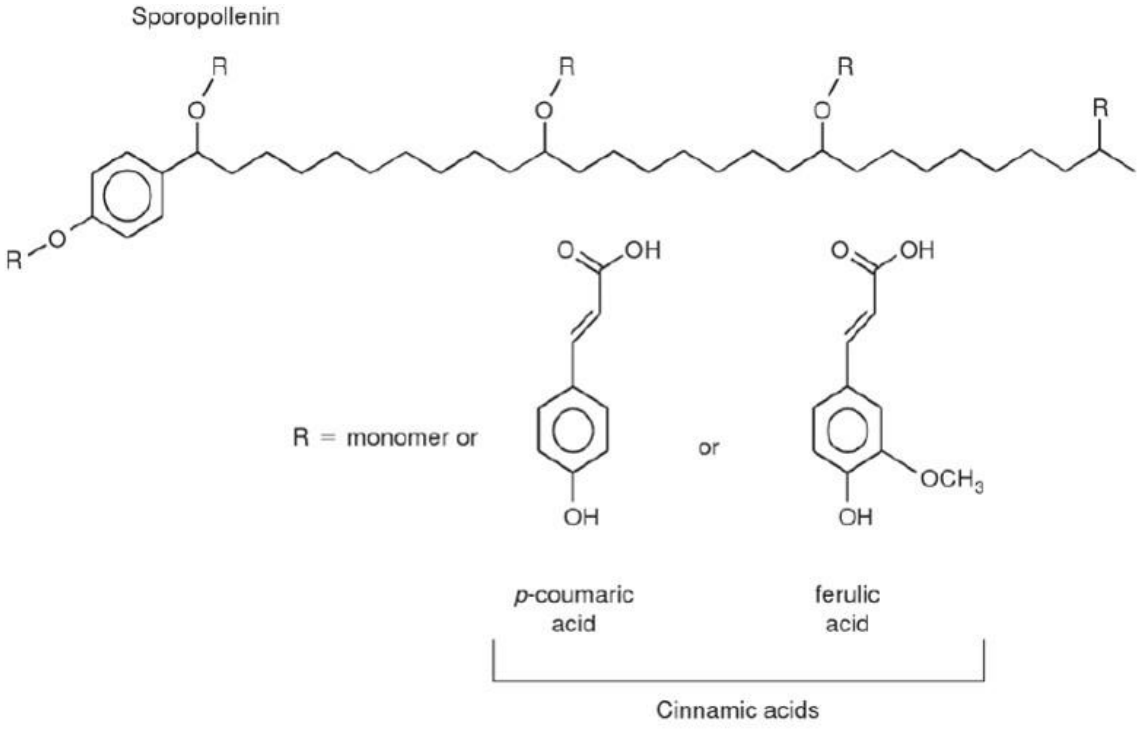

Figure 1.7 Proposed structure of sporopollenin building blocks taken from reference [58].

1.3.3 Mechanical property of pollen exine

The mechanical properties of sporopollenin are rarely reported in the literature, but they are of great importance to the natural protective performance and adhesion behavior of pollen shells. For example, it was shown recently that the spines on sunflower and ragweed pollen particles can lock onto similarly-sized features on flower stigma surfaces, resulting in pressure-dependent adhesion behavior.[46] High modulus could support this unusual particle adhesive function, because of the frictional forces that would arise when pollens are pressed onto stigma hair features. In addition, some researchers reported that the mechanical properties of pollen shells were of great importance to understanding the contaminant adhesion on gecko skin.[3] The pollen modulus and its dependence on relative humidity are also expected to be important in the process of harmomegathy, in which desiccating pollen grains fold inwardly and lessen water loss by blocking pollen apertures.[59] This water-induced folding and its reversal upon rehydration at the stigma is dependent on modulus, and yet the dependence of sporopollenin modulus on water vapor exposure is unknown. Two somewhat-indirect measurements of the modulus of pollen shells have been reported. Liu et al. used a micromanipulation technique to measure the product of the Young's modulus and wall thickness ($E \times h$) of desiccated ragweed pollen to be 1653 ± 36 N/m under compression.[60] To obtain this value from compression data, a model of the pollen shell was required, and the pollen grain was treated as a smooth, spherical capsule with an air-filled core and an impermeable wall. On the other hand, while the pollen shell is actually a porous wall with elaborate surface morphology, thus a technique that does not require a morphological model would be desirable. Another paper used the Halpin-Tsai model with mechanical measurements of polymer-pollen composites to estimate the Young's modulus of acid-base treated ragweed pollen to be 70 MPa.[61]

However, this approach depends on assumptions of the model, which neglects particle surface morphology and imperfections in the adhesive interface between pollen and polymer. A direct method that does not make assumptions about pollen shape or adhesion with a matrix is preferable for achieving accurate measurements of pollen exine mechanical properties.

1.3.4 Atomic force microscopy for adhesion measurements

Soon after the atomic force microscopy (AFM) was invented by Binnig, Quate and Gerber in 1986 for imaging, it was also used to directly measure the interaction between particles and surfaces[62]. Then, the so-called "colloidal probe technique" was introduced by Ducker et al. and Butt to use a specific particle with better defined geometry than AFM tip[63]. Thus, the interaction between particles and surfaces could be better interpreted. The combination of AFM and colloidal probe technique provides a powerful and versatile tool for the study of surface forces, especially for adhesion force.

The process of measuring adhesion force by colloidal probe is identical to that of a standard AFM. The colloidal probe is mounted on the scanner, where the piezoelectric translator will bring the probe down to the substrate by applying a voltage onto the piezo actuator. Thus, the position of the probe will be recorded as the applied voltage, which can be converted to distance. Furthermore, a laser beam is reflected by the cantilever and monitored by a position sensitive photodiode, where the defection of the cantilever can be recorded and converted to the interacting force between the tip and the substrate. Finally, a force-distance curve can be obtained. The force-distance can be analyzed for different

types of forces and physical characteristics of particles and surfaces, such as adhesion, Hamaker constant and elasticity[64].

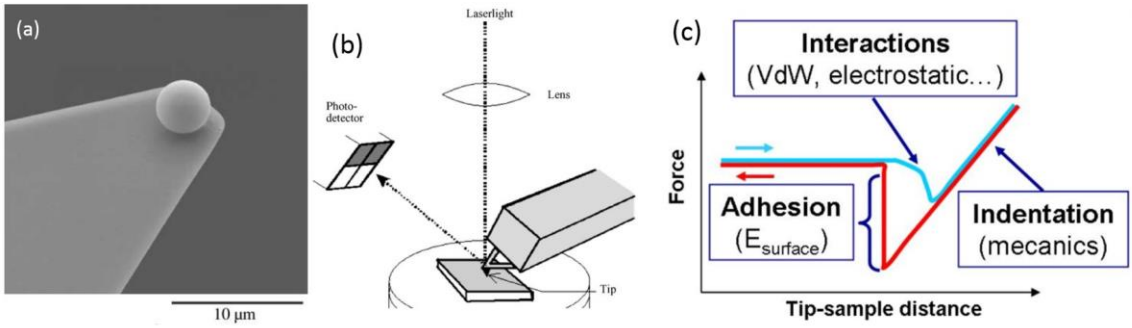

Figure 1.8 (a) SEM image of a colloidal probe; (b) schematic of an AFM[64]; (c) a typical force-distance curve.

1.4 Polymer composite and cellulose nanocrystal

1.4.1 Polymer composite overview

Composite materials are defined as "solid product consisting of two or more distinct phases, including a binding material (matrix) and a particulate or fibrous material", and filler is defined as "a relatively inert material added to a plastic to modify its strength, permanence, working properties, or other qualities, or to lower costs", according to the ASTM standard D883-17. Although filler may bring financial benefits by reducing the volume of a more costly matrix if the filler is less expensive, the main motivation of developing composite materials is to achieve superior properties, for example, in mechanical performance. In many cases, there is a tradeoff between performance and cost. Therefore, an active research area is to tailor filler dispersion and filler-matrix interaction to optimized composite properties. As a result of the growth of plastics industry and the polymers commonly used with filler (polyvinyl chloride, polypropylene, and polyester),

global polymer filler market is expected to reach an estimated $49.1 billion by 2021. The growing filler industry provides a unique opportunity for scientific researches. Some of emerging areas of great importance include: nano-sized, low cost, conductive fillers, and surface modification technology. One example is to utilize carbon fiber and carbon nanotube for high performance composite applications such as automotive and aerospace parts. However, some weaknesses of the utilization of carbon nanotube and carbon fiber materials limited further advancements. For example, the toxicity of carbon nanotube can influence the manufacturing cost. Another example is that the extreme manufacturing condition of carbon fiber leads to high production costs and extra energy consumption. Therefore, more efforts are taken to explore more sustainable filler from bio-resources. One alternative bio-filler can be used to substitute carbon fiber and nanotube is cellulose nanocrystal (CNC). Cellulose nanocrystals possess attractive properties including: high mechanical strength and modulus, low density (higher strength than steel and 5 times less dense), high surface area, high aspect ratio, and a low coefficient of thermal expansion. The promising potential of CNCs has led to a great number of researches trying to incorporate CNCs into polymer matrix to achieve superior mechanical performance.

In order to understand the limitation of reinforcing the mechanical properties of polymer matrix with filler particles, it is important to discuss how the mechanical performance can be enhanced by adding filler particles. The most relevant mechanical properties to this work is tensile strength, and the relevant particle variables include, but not limited to: particle size, particle loading, particle dispersion and particle-matrix adhesion. Fu *et al.* gives a comprehensive review of such property relations with polymer composites and low aspect ratio particles, where the general trends hold for all types of

particle[9]. To begin with, the tensile strength of a material is defined as the maximum stress that can be sustained under uniaxial tensile loading. Thus, the stress transfer between particle and matrix can determine the quality of reinforcement effect. It is intuitive that smaller particle size can result in higher surface area and thus a more efficient stress transfer. Moreover, a good particle-matrix adhesion is critical to transfer the stress between two distinct domains. When a discontinuity between particle and matrix exists, the particles cannot take any of the external load experienced by polymer, resulting in a weaker composite. Finally, higher particle loading usually increases the tensile strength until a critical point is reached. Beyond the specific critical point, larger particle aggregates can be formed, leading to a larger effective particle size. The lager particle aggregates can also reduce the particle-matrix adhesion by interacting with neighboring particles.

All particle variables discussed above have a significant role in the reinforce performance of composite materials. Although particle loading is easy to control, much more research efforts are taken to achieve better dispersion, avoid aggregations and improve particle-matrix adhesion for enhanced mechanical properties of composite materials.

1.4.2 Cellulose nanocrystals as composite fillers

Cellulose is the most abundant biopolymer in the world with an estimated production of 90 billion tons annually. The chemical structure of cellulose is known as a linear homopolymer composed of ringed anhydroglucose unit (AGU) as shown in Figure 1.9. The repeat units are connected by covalently oxygen to C1 of one AGU and C4 of another AGU, known as the 1,4 β-glucosidic linkage. Each AGU has three hydroxyl

groups, belonging to C2, C3 and C6, respectively. Due to the large content of hydroxyl group and oxygen atoms, cellulose is very likely to form intermolecular hydrogen bonding with itself and other molecules containing electron donor and/or accepter groups. The formation of intermolecular hydrogen bonding between cellulose has been utilized for many products, while the most well-known product is paper.

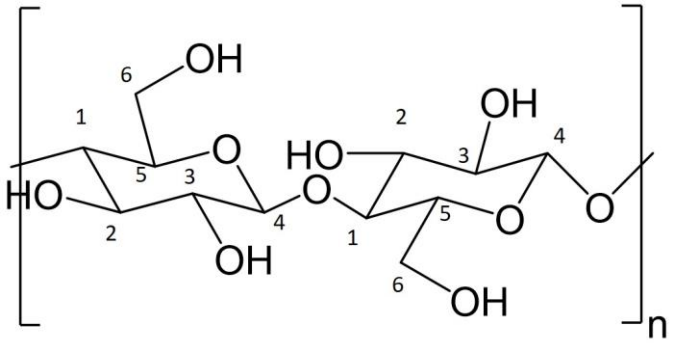

Figure 1.9 Chemical structure of cellulose.

Biosynthesized cellulose molecules are assembled into larger units, such as elementary fibrils, microfibrils, and cell walls, etc. One of the building blocks of the hierarchical cellulose structures is cellulose nanocrystals (CNCs). CNCs are individual crystalline cellulose, which are extracted from bulk cellulose by separating amorphous cellulose from crystalline region with mechanical or chemical treatment. Sulfuric acid hydrolysis is one of the most common method to extract CNCs. The resulted CNCs has certain part of hydroxyl groups modified, and result in sulfate half-ester group. After neutralization, the resulted CNCs bears a negative charge ($-SO_3^-$), leading to a stable aqueous suspension of CNCs due to double layer repulsion between CNC particles[65]. Moon et al. have given a comprehensive review for cellulose nanomaterials in terms of particle morphology, crystal structure, properties as well as an emphasis on cellulose

composites[66]. The unique properties of CNCs is responsible for its diverse range of applications. These properties include, but not limited to: high specific strength and modulus, high aspect ratio, low density, biocompatibility, low coefficient of thermal expansion, reactive hydroxyl surface, and especially renewability and sustainability[66]. Some of these properties make CNCs as a promising candidate as polymer composite fillers, such as high strength and modulus, low density and nano-size. CNCs have been used to reinforce a variety of polymer matrix, including both thermoplastic polymers such as polyethylene, polypropylene, polylactic acid and polymethylmethacrylate[67-70], and thermosetting polymers such as epoxy and polyurethane[71, 72].

However, the largest obstacle of utilizing CNC for composite reinforcement is incompatible nature and difficult dispersion of CNC in polymer matrix, as well as poor interfacial adhesion between CNCs as polar, hydrophilic materials and polymer matrix as non-polar, hydrophobic materials[73]. Therefore, various surface modifications of CNCs have been explored to tune the surface chemistry of CNCs and optimized the compatibility. Among those methods, covalently attachment of molecules by utilizing the abundant hydroxyl groups on CNCs is one of the most useful approach to introduce hydrophobicity on CNCs surface. Esterification is one common approach where a variety of chemicals can form ester linkages with -OH groups, such as acid anhydrides and carboxylic acid halides[74]. Silane based surface modification is another way to change the CNCs surface from hydrophilic to hydrophobic. Mabrouk et al. used methacryloxypropyl trimethoxylsilane (MPMS) a coupling agent in the mini-emulsion polymerization of acrylic monomers with CNCs. It was proven to be an efficient approach for the one-pot synthesis of a stable nanocomposite latex[75]. Finally, isocyanate is also used as an alternative

chemical for esterifying agent, since it can with -OH groups to form urethane linkages. Siqueira et al. compared the surface modification of CNC and microfibril cellulose (MFC) by N-octadecyl isocyanate on thermal and mechanical properties of polycaprolactone (PCL) composite. Although the degree of substitution for CNC was only 0.07, the results proved that the modification considerably improved the composite properties[76].

1.4.3 Acrylic polymer composite

Acrylic polymers represent a major class of commercial plastics and are utilized in a wide range of products and industries. Two of the most significant are the paints and coatings and transparent high-strength plastics for windows (such as Plexiglas® and housewares). For example, acrylic surface coatings are the leading material used in the paint and coatings industry and are utilized in all three major market categories: architectural coatings, OEM product finishes, and special-purpose coatings. Acrylics are one of the fastest-growing sectors in the coatings industry; global sales of acrylic coatings were valued at roughly $20 billion (manufacturer's level), in 2012. Acrylic coatings now account for about 25% of all coatings. Waterborne acrylic coating (WACs) formulations have been developed over several decades to address mounting concerns over volatile organic compounds. The applications of WACs include industrial anti-corrosive primers for steel surfaces, topcoats to adjust sheen, and direct-to-metal primer finish coatings for appliances, automobiles, other equipment, and industrial maintenance. In addition, acrylic latex coatings are used in commercial and residential architectural paints to protect or decorate wood, metal, and other surfaces.

The objective of this invention is to develop scalable technology for the commercial utilization of cellulosic nanomaterials (CNs) and other cellulosic materials in acrylic-containing products.

In this work, polymethylmethacrylate (PMMA) is used as a model polymer to demonstrate the reinforcing effect of vinyl group functionalized CNCs in acrylic matrix. PMMA, also known as acrylic glass or trade name Plexiglas, is a transparent thermoplastic often used in sheet form as a light-weight or shatter-resistant alternative to glass. PMMA is also an economical alternative to polycarbonate (PC), when tensile strength, transparency and UV tolerance are more important than impact strength, chemical and heat resistance. Previously, A variety of organo-modified inorganic fillers have been incorporated in PMMA matrix, such as zinc oxide nanoparticles, titanium dioxide nanoparticles and montmorillonite (MMT) clay.[77-79] The results showed enhanced mechanical and thermal properties. Recently, CNCs were also incorporated in PMMA matrix with or without surface modification. Liu et al. prepared PMMA/CNC nanocomposite by first blending PMMA solution with unmodified CNC and then casting the mixture followed by drying processes.[80] The storage modulus of the nanocomposite showed evident enhancement. However, the transparency of composite material was significantly decreased. Sain et al. modified CNF with maleic anhydride followed by in situ polymerizing the modified particles with monomer.[81] Anzlovar et al. modified CNC with a reversible addition-fragmentation chain transfer (RAFT) agent. PMMA chains were grafted from the modified CNC surface. The resulted PMMA grafted CNCs were bulk polymerized with monomer, and showed enhanced tensile strength and impact strength. Given these researches, understanding and controlling the underlying mechanisms of

PMMA-CNC interactions to achieve desired performance is still at an early stage. It is critical to develop this understanding for future engineering applications of PMMA/CNC composites.

1.5 Thesis overview

This research aims to characterize and understand both physical and chemical adhesion of micro/nano sized particles. Two bioparticles, pollen in micro size, and CNC in nano size, are investigated in terms of particle-particle adhesion and particle-matrix adhesion, respectively. The main objectives are as follows:

I. Investigate micro particle-particle adhesion with a complex morphology
    i) Characterize the morphology effect on pollen-pollen interaction
    ii) Develop models to explain the effect of complex morphology
    iii) Characterize the mechanical properties of sporopollenin
II. Investigate nano particle-matrix adhesion with tailored surface chemistry
    i) Chemically modify the CNC surface
    ii) Formulate polymer composites compatible with modified CNCs

In Chapter 2, the unique interaction behavior between pollen exines will be characterized with AFM and colloidal probe. A mathematical model based on Hamaker's approach will be developed to explain and predict the characteristics of pollen-pollen interaction. Chapter 3 will investigate the elastic modulus of sporopollenin through a direct method, AFM nanoindentation. The effect of acid-base treatment and water exposure will be discussed. The mechanical properties of sporopollenin will be compared and analyzed with common non-crystalline organic biomaterial. In Chapter 4, vinyl functionalization of the CNC

surface will be explored by utilizing a versatile hydroxyl/isocyanate chemistry. The efficiency of the chemical modification will be evaluated by attenuated total reflectance-Fourier transform infrared analysis (ATR-FTIR), elementary analysis, X-ray diffraction (XRD) and solid-state NMR. The introduced hydrophobicity on CNCs surface will be tested by contact angle measurement. Chapter 5 will compare and discuss three different preparation methods for PMMA and modified CNC (m-CNC) composites. The mechanical, thermal and optical properties of PMMA composite made of unmodified CNCs (um-CNCs) and m-CNC will be compared.

CHAPTER 2. INTERACTION OF COMPLEX MICROSTRUCTURED PARTICLES: ROLES OF ADHESION, GEOMETRY AND FRICTION

2.1 Overview

The interaction between microparticles or between microparticles and surfaces has been a subject of intense study for a long time, due to its significant role in many natural phenomena (pollination, dispersal of spores, etc.) and industrial processes (powder handling, biofouling, colloidal aggregation and dispersal, etc.). Although the interaction between smooth particles with simple shape (spheroidal, ellipsoidal and rod-like particles, etc.) has been well studied, many microparticles encountered have rough surfaces and complex shape, of which the interaction is much less investigated. This chapter characterized and simulated the interaction between microparticles with complex morphology. Sunflower pollen grains were used as a model particle due to their naturally-evolved complex surface morphology. Atomic force microscopy (AFM) combined with pollen colloidal probes were utilized to investigate the interaction between pollen grains. The force-distance curves obtained from AFM were analyzed to give the adhesion force and specific interacting mechanisms. The results showed that the pollen-pollen adhesion can vary from extremely high (~450 nN) to very low, even lower than that of the pollen-flat surface interaction (~30 nN). This large variation resulted from the orientation-dependent interactions of spines on the opposing sunflower pollens. Five typical force-distance curves were identified from pollen-pollen interactions, suggesting that multiple adhesion mechanisms may govern the interactions between spiny microparticles. A hybrid

model was developed based the Hamaker approach and Amontons' law of friction to explain the unique pollen-pollen interaction. The results suggest that the interaction between spiny pollen grains was governed by both adhesion and friction. Different orientations of spines lead to different relative contributions from adhesion and friction, and is proposed to be the source of variation in the force-distance curves. This work provided new insights into the tuning of adhesion over forces from 10 nN to 1000 nN between micro-sized particles. These results are helpful to understand natural phenomena such as transport of allergens and pollination process. They are also useful in advanced material applications including paints, coatings, bio-sensors, drug delivery, pharmaceutical industry, and composite materials.

2.2 Introduction

Microparticles usually refer to particles between 0.1 and 100μm in size[82], which are encountered in daily life, including pollen, dust, flour, powdered sugar, etc. Microparticles are involved in many application fields, such as catalysis[83], electronics[84], biosensor[85], drug delivery[86] and separation.[87] In these fields, the adhesion between microparticles or between particles and surfaces has been the subject of intense investigation for several decades, as adhesion plays a significant role in many natural process (pollen-stigma interaction, the dispersal of fungal spores and the infection of virus, etc.) as well as industrial applications such as, medical implants, semiconductor manufacturing, surface coating, and fouling control.[19, 88, 89]

The dry adhesion between neutral microparticles or between particles and substrates in air can be influenced by (a) the geometry of particles and substrates, (b) surface

roughness and (c) material properties (viscoelasticity, Hamaker constant, etc.). For the geometry, spherical particles and flat surfaces are the most common geometries in the literature. Although some phenomena can be captured by these simple geometries, most natural phenomena and industry processes usually involve non-spherical particles and structured surfaces.[90-94] Besides the geometries of particles and surfaces, surface roughness also plays an important role in the adhesion. Even if the interacting bodies have simple or regular geometries like sphere or cylinder, the interaction of the contacting partners could be complicated by the surface roughness, i.e. the asperities on a smaller scale compared to the characteristic length of the particles or surfaces.[3, 27, 31, 91, 95-98] Moreover, the material properties are also of great importance in the particle adhesion. For example, soft microparticles usually have a larger contacting area than hard ones under the same load, thus have higher adhesion forces.

A variety of non-spherical particles and micro-structured surfaces are fabricated by polymerization or lithography[99-102], to investigate the geometry effect of particles or surfaces on the adhesion. However, it remains challenging to fabricate particles with complex morphology and hierarchical roughness. Few studies regarding to microparticles with complex geometry are reported to date. Meanwhile, various models have been developed to predict the dry adhesion/Van der Waals force, including Hamaker's method[13], Lifshitz' method[26] and modified model by other researchers[27, 28, 30-32] to take surface roughness into account. Theoretically, these models can be applied on arbitrary geometries. However, the integral will be extremely complicated with structured surface or irregular morphology. Thus, the application of these models are limited within some basic geometries, such as spherical and cylindrical geometries.[23]

In order to unveil the effect of complex geometry/morphology on microparticle adhesion, plant pollens are used as model particles. Comparing with synthetic particles, pollen grains are easily obtained and have complex evolutionary-optimized morphology, which can be used to investigate the geometry and roughness effect on the adhesion between particles and surfaces. Meanwhile, it has been demonstrated that pollen adhesion is critical to plant reproduction, inspiring for biomimicry to engineer tunable adhesion between particles and micro-patterned surface, and relevant to topics such as transport of allergens and atmospheric phenomena.[46] The objective of this study was to understand the effect of the spiny morphology on particle-particle interaction in air by using sunflower pollen as a model. Atomic force microscope (AFM) was used with colloidal probes to directly investigate the pollen-pollen interaction. A mathematic model based on Hamaker's method was developed to interpret the unique pollen-pollen interaction behavior, and the function of sunflower pollen spines during the interaction.

2.3 Experimental methods

2.3.1 Materials

The native non-defatted sunflower pollen grains were purchased from Greer Laboratories (Lenoir, NC) and stored at 0 °C. Methanol, ethanol and chloroform were purchased from Sigma-Aldrich and used as received. Tipless rectangular cantilevers (FORT-TL, Applied NanoStructures, Inc., Santa Clara, CA) with the nominal spring constant of 0.6~3.7N/m were used to prepare the colloidal probe. Silicon wafers were purchased from UniversityWafer Inc. (South Boston, MA). Epoxy glues (LOCTITE®, 2 h setting time) were purchased from Henkel Corporation (Rocky Hill, CT) to fix pollen gains

on AFM cantilevers and silicon wafers. Sulfuric acid (97 wt.%, BDH Chemicals Ltd.) and hydrogen peroxide (30 wt.%, BDH Chemicals Ltd.) were used to prepare piranha solution to clean silicon wafer.

2.3.2 Pollen preparation

Commercial non-defatted (ND) sunflower pollen grains (Greerer) have more intact shape and straight spines, while commercially defatted sunflower pollens (pollenkitt was partially removed by the manufacturer with an ethyl ether washing step) have many broken or bended spines, as shown in **Error! Reference source not found.**. In order to isolate the effects of morphology on adhesion, we obtained non-defatted sunflower pollen grains and applied a solvent washing procedure to remove the pollenkitt. Non-defatted pollen samples were washed in a mixture of chloroform and methanol, a solvent for external pollenkitt, but a nonsolvent for the sporopollenin exine.[103] Chloroform and methanol were mixed first with a volumetric ratio of 3:1. Then, approximately 1 g of ND sunflower pollen were dispersed in ~33mL chloroform/methanol mixture. After 30 minutes, the suspension was centrifuged with the rate of 3000 rpm for 10 minutes. The supernatant was poured out and the sediments were dispersed in chloroform/methanol mixture again. This procedure was repeated three times. Then the pollen grains were washed with ethanol three times to remove any residual solvent. After washed and re-dispersed with ethanol, a small amount of the pollen suspension was spread on a glass slide and dried in air for 24 hours. Pollens subjected to this solvent washing procedure are referred to as “cleaned pollen” (CP). Cleaned sunflower pollen (CPsf) were used to prepare the colloidal probe and substrates for AFM measurement.

2.3.3 Colloidal probe and substrate preparation

Tipless rectangular cantilevers (FORT-TL, Applied NanoStructures, Inc., Santa Clara, CA) with the nominal spring constant of 0.6~3.7N/m were used to prepare the colloidal probe. By using a micromanipulator (NARISHIGE, Japan) and an optical microscope (Olympus BX51), a small amount of epoxy resin will be put on the end of the tipless cantilever.[44] Then a single pollen grain will be attached on the epoxy resin. After curing for 24 hours, the pollen grain will be immobilized on the end of the cantilever (**Error! Reference source not found.**). The actual spring constants for the cantilevers with the attached pollen need to be determined on a rigid substrate by the methods of Burnham and Hutter et al.[104, 105]

Silicon wafer is rigid enough to calibrate the spring constant of the colloidal probe. A silicon wafer was cut into 10mm×10mm pieces and treated by piranha solution, 75 vol.% sulfuric acid (98 wt.%) and 25 vol.% hydrogen peroxides (30 wt.%), to remove the organic impurities on the surface. Afterwards, several CPsf grains were immobilized on the silicon wafer according to the similar procedure described above (**Error! Reference source not found.**).

2.3.4 Scanning electron microscopy (SEM)

The surface morphology of the pollen grains was characterized by scanning electron microscopy (SEM) (Zeiss Ultra60 FE-SEM, Zeiss, Germany) at accelerating the

potential of 5.0 kV. Cleaned defatted and non-defatted pollens were deposited on a piranha-etched silicon wafer and mounted on metal stubs using carbon tape. Samples were then sputtered with gold/palladium in a Hummer 6 Au/Pd sputterer.

2.3.5 Interaction force measurement

Interaction forces between cleaned sunflower pollens were measured using atomic force microscopy (AFM, Veeco Dimension 3100). AFM was operated in contact mode to directly probe the interaction force between probe pollens and substrate pollens. During the measurements, the probe pollen was firstly engaged with a pollen grain on the substrate (close to the substrate pollen, but not contacted yet), then the piezo actuator was driven by applied voltage to bring the probe approach, contact and retract from the substrate pollen. Consequently, a force-distance curve between two pollen grains was obtained by AFM. The load force applied during the measurements was 2.5 nN, which is approximately the gravity felt by a single pollen grain. The humidity was controlled at around 24% by purging the chamber with nitrogen gas.

Generally, there are three contacting configurations between probe pollens and substrates as shown in Figure 2.1: 1) the probe pollen interacts with the flat silicon wafer, as "Si" configuration; 2) the probe pollen interacts with a substrate pollen, the line linking the centers of two pollen grains forms an acute angle with the flat silicon wafer; and 3) the probe pollen interacts with a substrate pollen, the line linking two pollen centers is orthogonal to the flat silicon wafer.

To begin with, one probe pollen was used to measure the adhesion forces with 10 different substrate pollen grains with "Top" configuration. Ten force-distance scans were

obtained after the probe pollen was engaged on each substrate pollen. Secondly, the adhesion forces between ac pair of pollen grains were measured with different contacting configurations, as shown in Figure 2.2. About 30 contacting positions along the center line of the substrate pollen were chosen to be measured with the probe pollen. Obtained force-distance curves were analyzed in terms of adhesion forces, interacting ranges and unique shapes.

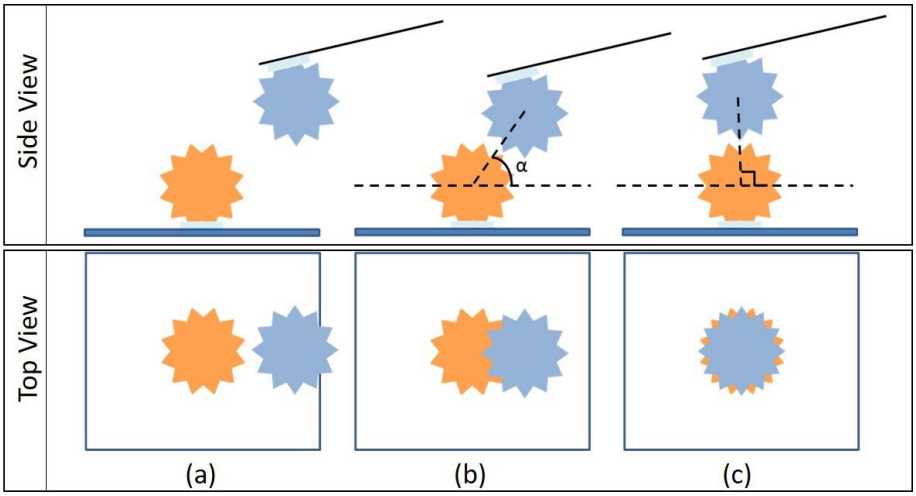

Figure 2.1 Three contacting configurations during AFM measurement: (a) "Si" configuration; (b) "Side" configuration; and (c) "Top" configuration.

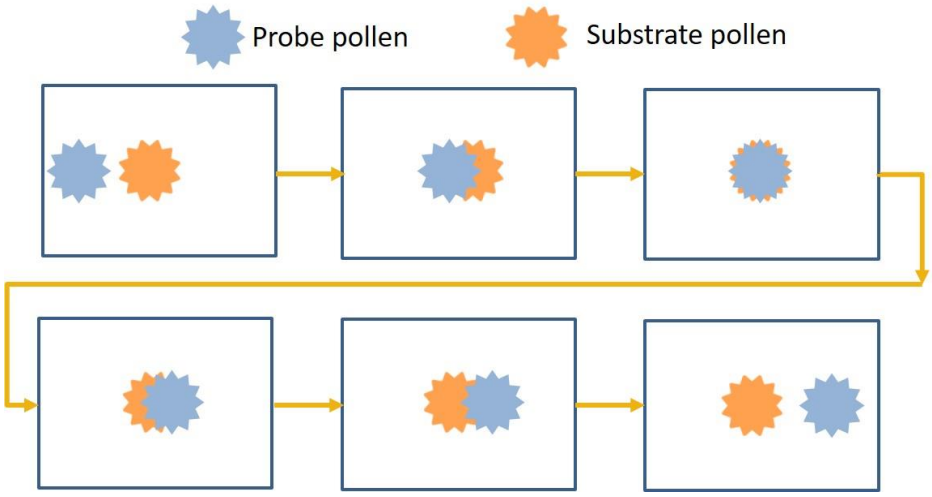

Figure 2.2 The procedure of measuring the interaction between the same pair of pollen grains with different configurations.

2.4 Results and discussions

2.4.1 Morphology of cleaned sunflower pollen

SEM images of cleaned manufacturer-defatted and non-defatted sunflower pollens are shown in Figure 2.3. The perforated exine surface of CPsf can be observed, indicating that pollenkitt coating was removed effectively with methanol/chloroform washing process. Both defatted and non-defatted CPsf have a spherical core shape with spiny asperities. However, many spines on defatted CPsf were broken or bent, due to the defatting process by the manufacturer. Therefore, non-defatted CPsf with intact shape and straight spines was used in the rest of this work. Table 2.1 shows the characteristics of sunflower pollens and surface morphology based on SEM analysis.

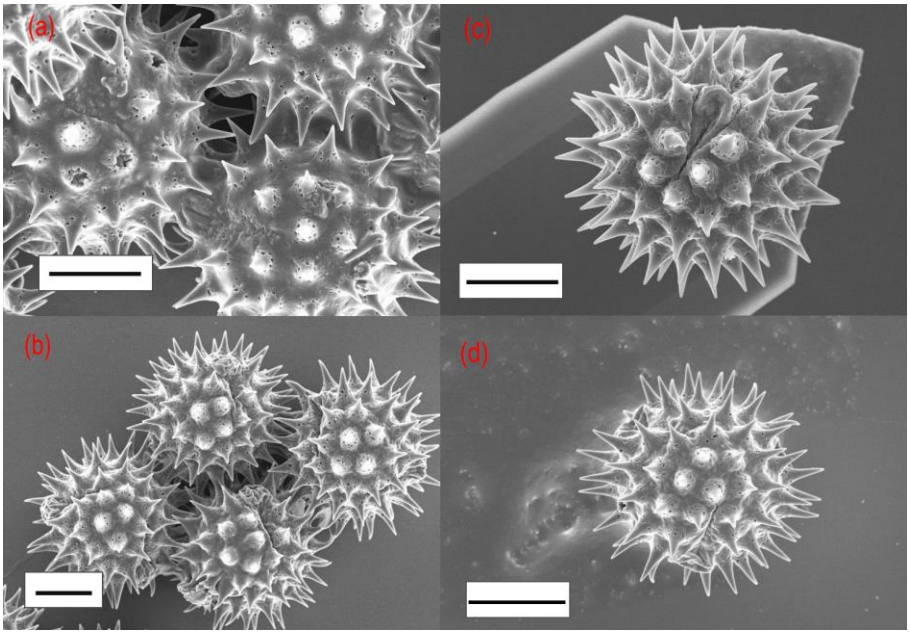

Figure 2.3 SEM images of (a) Defatted sunflower pollen after washing (D-CPsf) with the chloroform/methanol mixture (3:1); (b) Non-Defatted sunflower pollen after washing (ND-CPsf); (c) ND-CPsf immobilized on the cantilever of a AFM probe; (d) ND-CPsf immobilized on the silicon wafer; all scale bars are 10 µm.

Table 2.1 Characteristics of sunflower pollen grains and surface morphology from SEM image analysis

Pollen		Morphology				
	Shape	Size[a] (µm)	Height[b] (µm)	Radius[b] (nm)	Spine spacing (µm)	Spine density (μm^{-2})
Sunflower (Psf)	Echinate	30±4	3.5~4.0	120±10	2	0.32

a. Size means the diameter from the tip of one spine to that of the opposite spine.
b. Height and radius at the tip of reticulate bumps or echinate spines.

2.4.2 Adhesion forces between the same probe pollen and different substrate pollens in "Top" configuration

To establish a baseline for the adhesion of clean sunflower pollen, the probe was first loaded on the flat silicon surface. The adhesion of clean sunflower pollen on the flat silicon wafer is about 80 nN, which is consistent with previous results.[45] Then the probe pollen was aligned on the top center of a substrate pollen ("Top" configuration). After the engagement between the probe and the substrate, about 30 ramps (approaching and retracting once refer to a ramp) were performed and one force-distance curve was recorded subsequently every three ramps. The adhesion forces of these curves were shown in Figure 2.4. In Figure 2.4 (a), although two pollen grains were interacted at the same engaging position for all measurements, the adhesion forces varied from 330 nN to 30 nN. In Figure 2.4 (b), the same probe pollen was used to interact with another substrate pollen, and the adhesion forces ranged from 119 nN to 9.7 Nn. On the one hand, this wide varying range of the adhesion between microparticles indicates the highly rough surface of the particle as well as the complex surface ornamentation, which was also observed between spherical polystyrene microparticles.[96, 106] On the other hand, this may also because that the actual contact location is not exactly same between every ramps due to the lateral drifting of AFM.[107] In addition, the adhesion force between two pollen grains could be either higher or lower than that between the clean sunflower pollen and the flat silicon wafer. Considering Hamaker's equation (Figure 1.2) for vdW force, it is common that the sphere-sphere adhesion is smaller than the sphere-plane adhesion, due to the zero-curvature of the flat surface. Therefore, the lower limit of pollen-pollen interaction was attributed to the interaction between spines or between the spine and the core of the pollen, associated with a small contact area. However, the upper limit is too high to be interpreted by simple

models. Nevertheless, this higher adhesion force should be associated with a large contact area and result from the complex surface morphology.

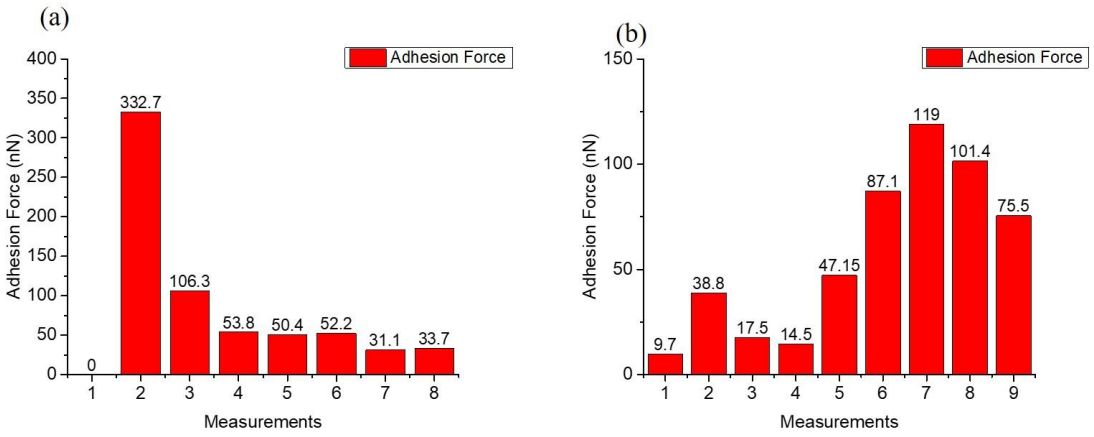

Figure 2.4 Two representative series of adhesion forces between the same probe pollen and two substrate pollens, each series was measured with "Top" configuration and single engaging position. (a) the first substrate pollen, the adhesion force ranged from 332.7 nN to 33.7 nN; (b) the second substrate pollen, the adhesion force ranged from 119 nN to 9.7 nN.

While the adhesion between a same pair of pollens varies widely as shown in Figure 2.4, the adhesion ranges between the same probe and different substrate pollens are also expected to vary, due to the different orientations of the spines on different substrate pollens. Given the relatively uniform shape and monodispersity of sunflower pollens, numerous substrate pollens were tested by the same probe with the "Top" configuration to represent different spine orientations. In each case the orientation of the substrate pollen is different than the probe. The average values and ranges of the adhesion forces of the same probe with each substrate pollen are shown in Figure 2.5. Each average value and force range was obtained from 10 measurements. The numbers at the horizontal axis represent different substrate pollens. "Si_1" and "Si_2" means the adhesion of the probe pollen on the flat silicon before and after interacting with the substrates particles. "W&E" means the

probe was withdrawn from a substrate pollen and engaged again on the same pollen to perform another 10 measurements. The measurements on the silicon wafer were taken from 10 different spots randomly chosen, while the measurements on each substrate pollen were taken at the same spot after the engagement. The varying ranges and average values of "Si_1" and "Si_2" were consistent, which indicates there was no contamination or large plastic deformation of the probe pollen during the measurements. As Figure 2.5 showed, the average values and range of the adhesion force between the same probe and different substrate pollens also varied widely. Some achieved extremely large adhesion up to 333nN, such as #7 and #11 substrate pollens, while some others had very small adhesion down to 1nN, such as #2, #3 and #8. Moreover, the varying range of the adhesion changed with different substrate pollens. The highest adhesion force of the lower bound for each substrate pollen was 95nN (#1), while the lowest value of the upper bound was 41nN (#10). Most of these force ranges overlapped from 50nN to 69nN, which is comparable with the adhesion on silicon wafer. This range may imply that one single spine of one pollen interacted with the core of the other one. The forces lower than this overlapped range may indicate the interaction between two spines or between the spine and nanoscale asperities with a smaller contact area, while the forces higher than this range may indicate an interlocking situation which enables a larger contact area. The differences of the average adhesion and the force range suggested that the interaction between pollen grains are highly dependent on the spine orientation. Different spine orientations (substrate pollens) have specific capabilities to achieve high (e.g. #6:140~95nN) or low (e.g. #10: 41~17nN) adhesion, which is evidently associated with the effect of this complex morphology.

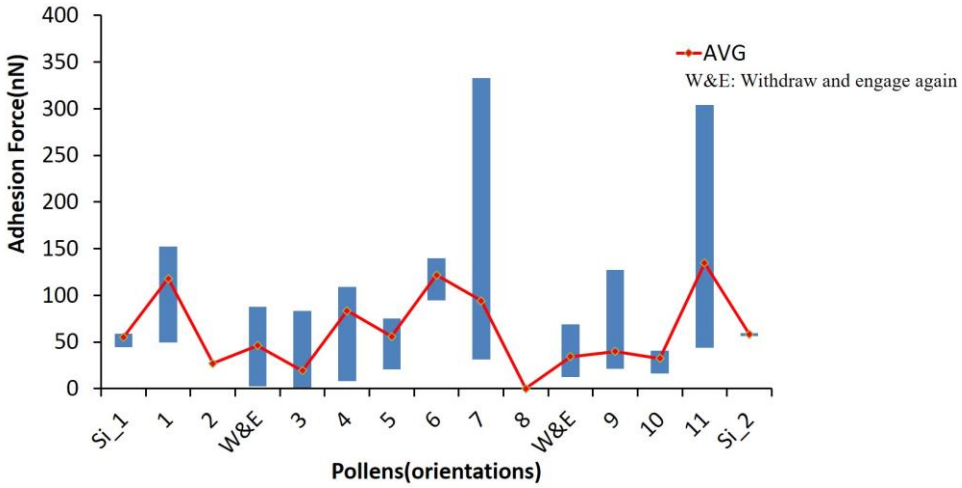

Figure 2.5 Ranges and average values of the adhesion forces between the same probe and different substrate pollens.

2.4.3 Adhesion forces between the same pair of pollens with different configurations

The effects of spine orientations on pollen-pollen adhesion were also examined with the same pair of pollens by probing a substrate pollen from various engagement positions moving from one side to the other along the center-line, as indicated in Figure 2.2 and Figure 2.6(a). The adhesion force corresponding to different engaging positions was shown in Figure 2.6(b). The adhesion force stayed at about 45nN when the probe is aligned with the substrate pollen in the "Side" configuration, while a extremely high adhesion force (>450 nN) was achieved with the "Top" configuration. This suggests that the interaction of crossed spines may lead to small adhesion, while the interaction of parallel spines would lead to a large adhesion force.

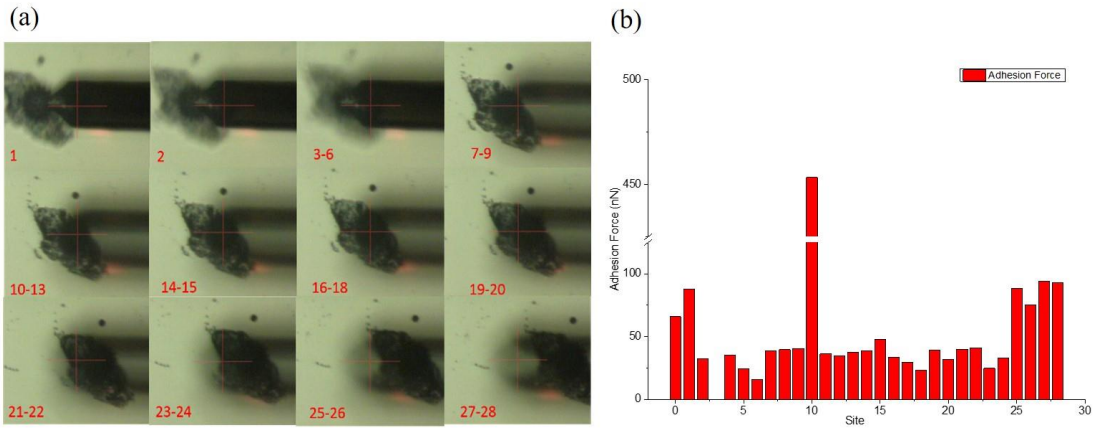

Figure 2.6 (a) the optical images by the camera on AFM, showing different engaging sites along the center line of the substrate pollen, the numbers marked the measurements on each site; (b) the adhesion force of each measurements. "0~1", "25~28" were measured on silicon wafer ("Si" configuration); "10~18" were considered as measured with the "top" configuration, all the others were in "Side" configuration.

2.4.4 Force-distance curves of pollen-pollen interaction

In order to further investigate the mechanism of pollen-pollen interaction, not only the magnitude of the adhesion force, but also the shape of the force-distance curve need to be analyzed. A typical force-distance curve was divided into several sections to be systematically analyzed as shown in Figure 2.7. In each section, two or three characteristic behaviors can be identified, as shown in Table 2.2. The approaching curve includes "Engage" and "1st Relaxation" segments, while the withdraw curve contains "Accumulating" and "2nd Relaxation" segments. For the Engage segment, both a Regular type (the approach curve directly jumps into the lowest point) and a Multiple type (the approach curve collapses more than once) were observed. In the 1st Relaxation segment, both a Regular (the slope of the curve equals to the spring constant (SC) of the cantilever) and a Slow (the slope of the curve is smaller than SC) type are identified. In the

Accumulating segment, a Regular (the slope of the curve equals to SC), a Slow (the slope of the curve is smaller than SC) and a Multiple (more than one local minimum are reached) type are identified. In the 2nd Relaxation segment, three typical behaviors were observed as Regular (the slope of the curve is larger than ten times of SC), Slow (the slope of the curve is smaller than 10×SC) and Multiple (the retract curve collapse more than once).

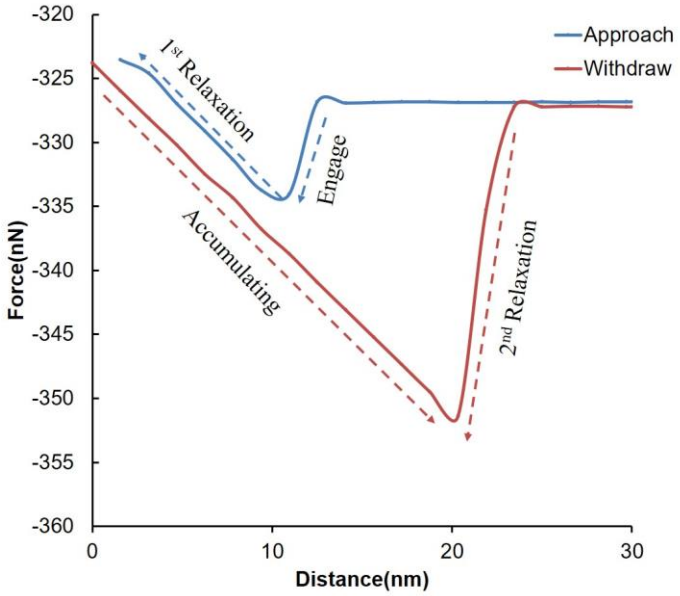

Figure 2.7 A typical force-distance curve from pollen-pollen interaction.

Table 2.2 Characteristic behaviors of the force-distance curves of pollen-pollen and pollen-silicon wafer interaction.

Engage	1st Relaxation	Accumulating	2nd Relaxation
Regular	Regular	Regular	Regular
Multiple	Slow	Slow	Slow
		Multiple	Multiple

Based on the characteristics of two sections (Accumulating and 2nd Relaxation) of withdraw curves (table 2.2), six distinctive types of force-distance profiles were identified as shown in Figure 2.8. Type RR (Accumulating = R and 2nd Relaxation =R) has only been observed with "Si" configuration, when the spike of the pollen only contacts a smooth flat surface. The slope of the "Accumulating" section is equal to the spring constant of the cantilever, which means that there is no relative motion between the probe pollen and the substrate pollen until the probe pollen is pull off from the substrate. Type SR is always associated with a relatively large adhesion (>100nN). The slope in the accumulating section is much less than the spring constant of the probe cantilever, indicating that the probe pollen moved upward relative to the substrate pollen before completely pull-off. The extremely large adhesion may be achieved by interlocking spines, which increase the contact area. Type SS is always associated with a relatively small adhesion (<50nN), which indicates the contact area is smaller than the pollen-silicon. In addition, sliding between two spines may result in slow accumulating and relaxation. SS (Plateau) is similar to SS except a plateau occurs after accumulating section. The "plateau value" indicates the spine slides along another spine, while the deflection of the cantilever does not change too much. Type SM has more than one relaxation sections in the retraction curve. After the accumulating segment, the curve jumped out and then was followed by a plateau, which indicates that a spine has become 'hooked' onto another, and the two spines slide along one another for about 100nm and then separate eventually. Type MR not only has a slower slope, but also multiple steps in the accumulating section, which may be associated with multiple deformed and sliding spines.

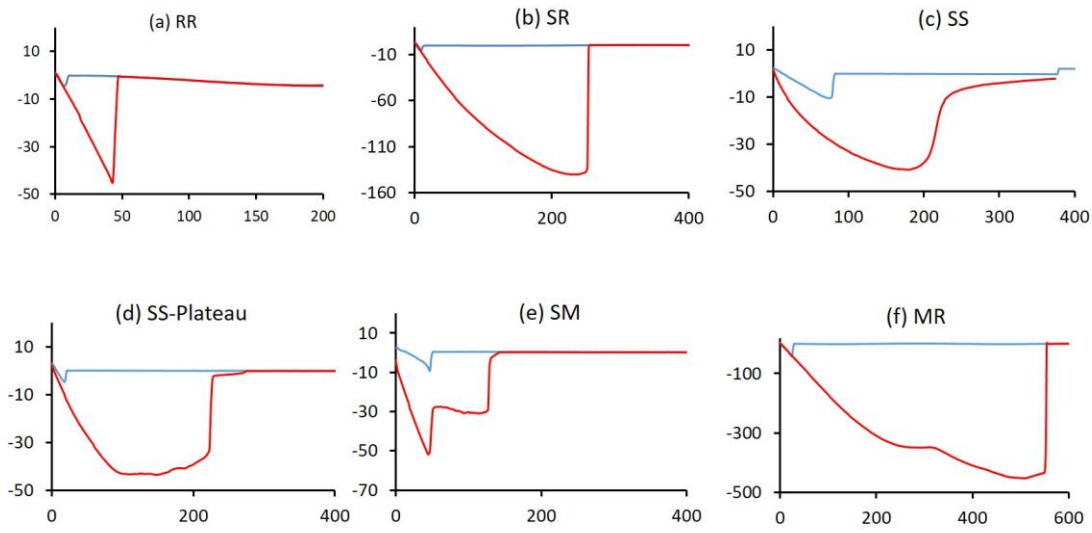

Figure 2.8 Six typical force-distance curves. The vertical axis is force (nN); the horizontal axis is distance (nm); the blue line is approach curve; the red line is withdraw curve.

2.4.5 Quantitative model for pollen-pollen interaction

2.4.5.1 Methods

The prior results with AFM measurements revealed that the interaction between pollen grains in ambient condition are highly dependent on the surface morphology and the orientation of spines. The spine-spine interaction (adhesion and friction) may lead to widely varied adhesion forces and force-distance curves. It is both fundamentally and practically important to develop a quantitative model to explore the contributions of vdW adhesion and friction. Non-retarded Hamaker method was adopted to describe the adhesion (pull-off) forces and force-distance curves of pollen-pollen interaction from AFM measurements.

In order to accurately include the morphology effect of sunflower pollens, the spines and the core of the pollen grain were treated separately, which will give three

configurations of pollen-plate and pollen-pollen interaction: a) Spine-Plate, b) Spine-Core and c) Spine-Spine interaction (Figure 2.9). These three configurations were modeled and combined to describe the adhesion between pollen grains. Therefore, the adhesion or pull-off force (F_A) between two pollen grains consists of two components as shown in equation 2-1: the adhesion (F_a) on the vertical direction, and the friction (F_f) on the vertical direction between two sliding spines.

$$F_A = F_a + F_f \tag{2-1}$$

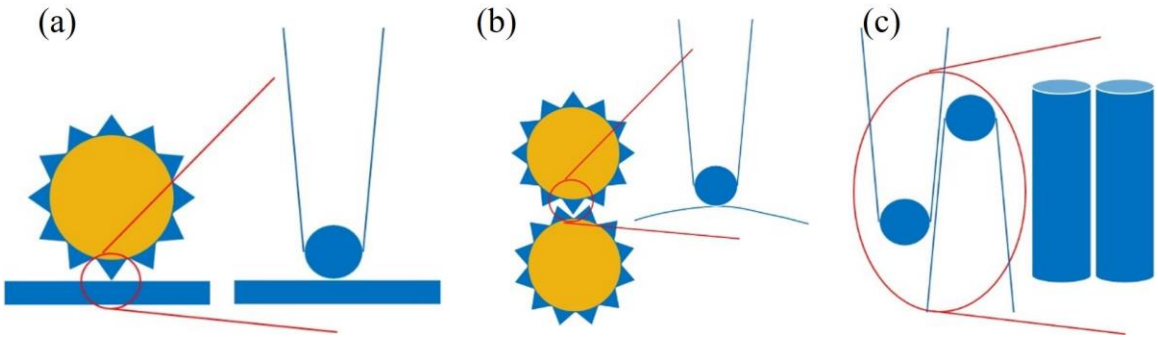

Figure 2.9 (a) Spine-Plate, (b) Spine-Core, (c) Spine-Spine-Parallel configuration and simplified geometries.

For Spine-Plate configuration (SP), the adhesion force was assumed to be equal to the adhesion between a plate and a sphere of the same radius as the spine tip, which can be modeled by equation 2-2. For Spine-Core configuration (SC), the adhesion is equal to the adhesion between two spheres, one with the radius of the spine tip, and another with the radius of the pollen core, which can be modeled by equation 2-3. For Spine-Spine configuration, the conical spines will be assumed as cylinders to further simplify the problem.

$$F_a = \frac{-A_{132}R}{6D^2} \tag{2-2}$$

$$F_a = \frac{-A_{132}}{6D^2}\frac{R_1R_2}{R_1+R_2} \tag{2-3}$$

There are three extreme limits of Spine-Spine interaction: two spine apexes interaction (SS-A), two parallel spines (SS-P) and two crossed spines (SS-C) interaction as shown in Figure 2.10. Equation 2-3, 2-4 and 2-5 were used to describe the van der Waals force between two spines in these three extreme configurations. Amontons' first law (equation 2-6) will be used to calculate the friction, F_f, between two spines. The kinetic friction coefficient will be estimated as 0.1 based on a previous study in Meredith's group, which is the coefficient between pollen and silicon wafer. This assumption should be valid, considering the smooth surface of the spines (Figure 2.3). The adhesion force between spines, F_a, was used as the loading force during sliding.

$$F_a = \frac{-A_{132}\cdot l}{8\sqrt{2}D^{5/2}}\sqrt{\frac{R_1R_2}{R_1+R_2}} \tag{2-4}$$

$$F_a = \frac{-A_{132}}{6D^2}\sqrt{R_1R_2} \tag{2-5}$$

$$F_f = \mu \cdot F_a \tag{2-6}$$

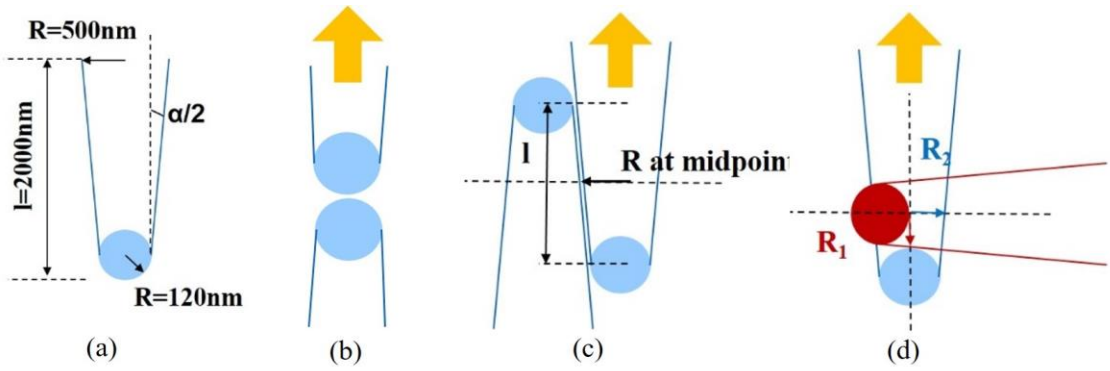

Figure 2.10 (a) Dimensions of sunflower pollen spines; (b) spine apex-apex interaction; (c) parallel and (d) crossed spines configuration.

After establishing equations for different configurations, it is important to estimate the Hamaker constant between sunflower pollens. The Hamaker constant between a pollen and a silicon wafer, A_{132}, approximates to 8.5×10^{-20} J.[45] The subscript 1 represents the exine of sunflower pollen; 2 represents silicon wafer; and 3 represents air. The Hamaker constant between silicon in vacuum, A_{22}, is 7.59×10^{-20} J, and A_{33} is 0 J.[108] Based on the combining relations of Hamaker constant, equation 2-7, the Hamaker constant between sunflower pollens in air, A_{131}, is 9.5×10^{-20}J.[109]

$$A_{132} = (\sqrt{A_{11}} - \sqrt{A_{33}})(\sqrt{A_{22}} - \sqrt{A_{33}}) \quad (2\text{-}7)$$

The separation distance between contacting partners, D, will be taken as 0.165 nm.[45] Although the spine will be simplified as a cylinder, the actual spine is a cone with blunted apex. The cross-sectional radius of the cone will increase along with the distance, l, to the apex, according to equation 2-8. The radii of the spine tip and the core of the sunflower pollen as well as other dimensions will be taken as shown in.

$$R = 120 + l \times \tan(\frac{\alpha}{2}) \quad (2\text{-}8)$$

Table 2.3 Dimensions of sunflower pollens used in the model.

Tip radius (nm)	Core radius (μm)	Open angle α(degree)	Length (μm)
120	20±1	16±4	~2

2.4.5.2 Adhesion forces between pollen grains on vertical direction

To test the Hamaker method by comparison to previous adhesion force results, the adhesion of a sunflower pollen on a flat silicon wafer was calculated by using equation 2-2. Single spine contact was assumed and the equation gave the adhesion of 62 nN, which is consistent with the previous study[45] as well as the results in this work. However, the actual adhesion should be the summation of Spine-Plate and Core-Plate interaction. The separation distance, *D*, from the core of the pollen to the silicon wafer will be about 4 microns due to the long spines of the sunflower pollen. Comparing with 0.165 nm, the separation distance between the contacting spine and surface, this large separation distance will drastically reduce the adhesion according to equation 2-2. In addition, the retardation effect at large separation distance will also reduce the adhesion. Both of these reasons lead the interaction between the spine and plate dominating the adhesion of the pollen on the silicon wafer. For the same reasons, the vdW interaction between the cores of two contacting pollens was also neglected, while the Spine-Core interaction dominated.

Furthermore, the Spine-Core interaction was computed according to equation 2-3. Firstly, we assume that there is only one spine of either the probe pollen or the substrate

pollen contacting the core of the other pollen grain. The tip radius of the spine, R_1, is 120 nm. The core radius, R_2, is 20 μm. The Hamaker constant, A_{131}, is 9.5×10^{-20} J. This gave the adhesion of the single spine-core configuration as 62 nN. A larger adhesion force may be achieved by the multiple spine-core contact. For example, two spine-core interactions may lead to the adhesion force of 124 nN. Nevertheless, this adhesion force was obtained by assuming the core of the pollen has a smooth surface, which is not true. From the SEM image (Figure 2.3), we can find many nanoscale wrinkles, asperities and pores on the core surface. This nanoscale roughness may reduce the adhesion force between the spine and the core.[31] For the spine-spine interaction, firstly, we can calculate the adhesion force when the apexes of two spines contact. In that case, the adhesion force is 35 nN. This is an extreme case since the apex has the smallest radius within the spine. Thus, if assuming the surface of the whole pollen grain is smooth, 35 nN should be the lower limit of the adhesion between two sunflower pollens. However, the experimental results showed that the smallest adhesion is 1.4 nN. This extremely small adhesion may be caused by the nanoscale asperities.

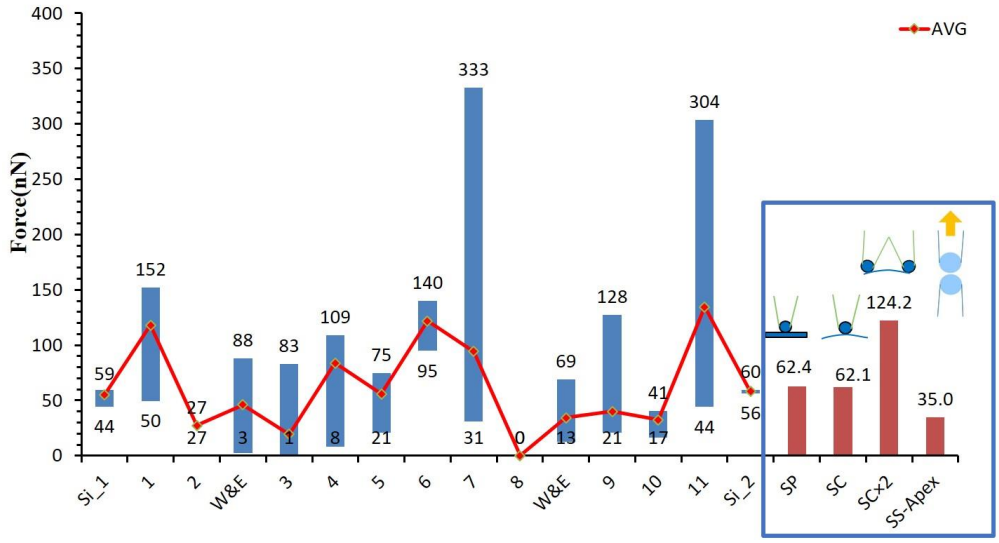

Figure 2.11 Adhesion forces on vertical direction calculated with Hamaker's method compared with experimental results in Figure 2.5.

2.4.5.3 Friction forces of spine-spine interaction

For the friction between two spines, equation 2-4 and 2-5 were used to calculate the adhesion forces between two parallel spines and between two crossing spines, respectively. For two parallel spines, R_1 and R_2 are taken as the radii of the spine at the midpoint of the contacting part. The variable l is the length of the contacting part of two spines. Since the radius of the spine will vary with the length, R_1 and R_2 can be determined according to Eqn. (2-8) with l replaced by $2/l$ to represent the midpoint. For two crossing spines, we assume R_1 is 150 nm and R_2 varies from 150 nm to 500 nm, since the tip of the spine rather than the base is more likely to interact with another spine. Figure 2.12 showed that the friction varied as a function of the contact length of parallel spines or the radius of the crossed spines at contact point. Figure 2.12(a) showed that the friction between parallel spines decreased from 800 nN to about 0 nN when the contacting length decreased from 1000 nm to 0 nm. The slope, dF/dl, is about 0.8 nN/nm, which is about 50% lower than the

spring constant of AFM cantilever. Comparing with the experimental results, which showed largest adhesion of 450 nN, this computed range can fully cover the experimental results. It implies that the actual contact length may be shorter than 700 nm. Figure 2.12(b) showed that while two crossed spines were sliding away from each other, the radius of one spine stayed constant at 150 nm, and the radius of another spine at the contact point kept decreasing from 500nm to 150nm. Meanwhile, the friction decreased from 15.96nN to 8.74nN, and the decaying rate of the friction force, d*F*/d*l*, is about 0.0035nN/nm. The friction between spines will contribute to the pull-off force obtained by AFM. Moreover, the decay rate of the friction with respect to the separation distance of the interacting pollens will affect the shape of the force-distance curve. Therefore, the slower accumulating, relaxation and plateau section could be interpreted as the combination of spine-spine friction and adhesion.

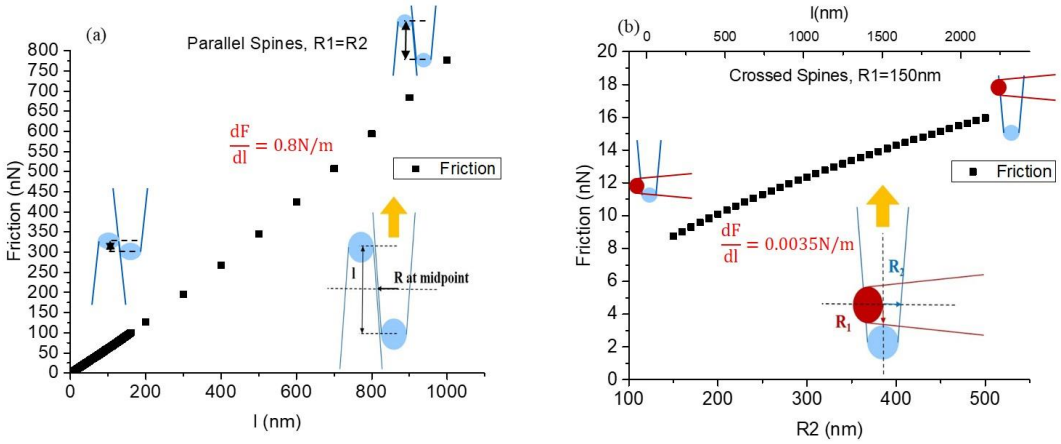

Figure 2.12 Friction force when two (a) parallel and (b) crossed spines slide against each other; (a) the X axis is the contact length; (b) the bottom X axis is the radius of the vertical spine at the contact point, the top X axis is the distance from the contact point to the apex of the vertical spine.

2.5 Conclusion

This work has revealed for the first time the detailed interaction behavior between two microparticles with complex, regular surface morphology. With micro-sized sunflower pollen as model colloidal probes particles, the particle-particle interactions were directly characterized with AFM. The adhesion (pull-off) force between two pollen grains varied from a few to hundreds of nanoNewtons. When two pollen grains were aligned as the "Top" configuration, the highest pull-off force was observed around 450 nN. However, when two pollen grains were aligned as the "Side" configuration, the adhesion forces remained around 30 nN, which is even lower than that of pollen-silicon wafer interaction ("Si" configuration). These results indicate that the orientations of pollen spines have a great influence on the strength of particle-particle adhesion. Furthermore, the analysis of force-distance curves indicates that in some cases, the spines move while in contact. Therefore, the sliding motion and friction forces between pollen spines were taken into account by using a mathematical model to simulate the pollen-pollen interaction. It was demonstrated that a combination of adhesion between pollen grains at vertical direction and friction between sliding spines led to the unusually high adhesions and special force-distance curve profiles.

CHAPTER 3. MODULUS OF SPOROPOLLENIN DETERMINED BY DIRECT NANOINDENTATION MEASUREMENT OF POLLEN EXINE

3.1 Overview

Sporopollenin, the polymer comprising the exine (outer solid shell) of pollens, is recognized as one of the most chemically- and mechanically-stable naturally-occurring organic substances. The elastic modulus of sporopollenin is of great importance to understanding the adhesion, transport, and protective functions of pollen grains. In addition, this fundamental mechanical property is of significant interest in using pollen exine as materials for drug delivery, reinforcing fillers, sensors, and adhesives. Yet, the literature reports of sporopollenin modulus are very limited. This work provides the first report of the elastic modulus of sporopollenin of pollen particles from three plant species: ragweed (*Ambrosia artemisiifolia*), pecan (*Carya illinoinensis*) and Kentucky bluegrass (*Poa pratensis*). Modulus was determined with atomic force microscopy by using direct nanomechanical mapping of the pollen shell surface. The moduli were atypically high for noncrystalline organic biomaterials, with average values of 16 ± 2.5 GPa (ragweed), 9.5 ± 2.3 GPa (pecan) and 16 ± 4.0 GPa (Kentucky bluegrass). The amorphous pollen exine has a modulus exceeding all non-crystalline biomaterials, such as lignin (6.7 GPa) and actin (1.8 GPa). In addition to native pollens, we have investigated the effects of exposure to a common preparative acid-base chemical treatment and elevated humidity on modulus. Acid-base treatment reduced the ragweed modulus by up to 58% and water vapor exposure

at 90% relative humidity reduced the modulus by 54% (pecan) and 72% (Kentucky bluegrass).

3.2 Introduction

Plant pollens are among the most unique naturally-occurring microparticles. Pollen grains are microscopic capsules carrying male gametes for plant reproduction. They have evolved optimized exine shells with remarkable structure and surface chemistry to facilitate pollination and germination. Recently, pollen grains have attracted increasing research interest due to their unique adhesion characteristics, low weight, high mechanical strength, functionalizability, fluorescence, and biocompatibility.[45, 46, 50, 61, 110] For example, the external shells of pollen grains can serve as lightweight, toughening fillers for polymers.[61] Diego-Taboada et al. used pollen shells as controlled-release drug delivery vehicles.[110] Moreover, pollens have been used as templates for fabricating metal-oxide magnetic replicas[47],[48] magnetic-core particles[49] and metallized shells[50] with unique combinations of multimodal adhesion and optical properties.

A native pollen shell consists of three domains from outside to inside: 1) pollenkitt, 2) exine and 3) intine.[111] The pollenkitt is an adhesive and viscous liquid coated on the exine. It can protect pollen from drying, promote adhesion and support pollination. The exine is the tough outer solid wall that often bears spines, bumps or grooves and exhibits an enormous species-specific diversity of morphology due to the size and shape of these surface features. The intine, made of cellulose, is a thin wall just inside the exine surrounding the generative cells inside the pollen shell. The exine influences adhesion and determines the external surface chemistry and mechanical properties of pollen grains. The

exine is mainly composed of sporopollenin, one of the most chemically-and thermally-stable biological polymers.[112, 113] The chemical composition of sporopollenin has been a subject of study and debate,[52] but the most recent consensus suggests that it consists of saturated and unsaturated aliphatic chains with conjugated aromatics that are highly cross-linked by ester or ether bonds to form a rigid structure. Meanwhile, the surface of the pollen exine contains hydroxyl groups that provide facile sites for functionalization.[114] The mechanical properties of sporopollenin are rarely reported in the literature, but they are of great importance to the natural protective performance and adhesion behavior of pollen shells. For example, it was shown recently that the spines on sunflower and ragweed pollen particles can lock onto similarly-sized features on flower stigma surfaces, resulting in pressure-dependent adhesion behavior.[46] High modulus could support this unusual particle adhesive function, because of the frictional forces that would arise when pollens are pressed onto stigma hair features. In addition, some researchers reported that the mechanical properties of pollen shells were of great importance to understanding the contaminant adhesion on gecko skin.[3] The pollen modulus and its dependence on relative humidity are also expected to be important in the process of harmomegathy, in which dessicating pollen grains fold inwardly and lessen water loss by blocking pollen apertures.[59] This water-induced folding and its reversal upon rehydration at the stigma is dependent on modulus, and yet the dependence of sporopollenin modulus on water vapor exposure is unknown. Two somewhat-indirect measurements of the modulus of pollen shells have been reported. Liu et al. used a micromanipulation technique to measure the product of the Young's modulus and wall thickness ($E \times h$) of desiccated ragweed pollen to be 1653 ± 36 N/m under compression.[60] To obtain this value from compression data, a

model of the pollen shell was required, and the pollen grain was treated as a smooth, spherical capsule with an air-filled core and an impermeable wall. On the other hand, while the pollen shell is actually a porous wall with elaborate surface morphology, thus a technique that does not require a morphological model would be desirable. Another paper used the Halpin-Tsai model with mechanical measurements of polymer-pollen composites to estimate the Young's modulus of acid-base treated ragweed pollen to be 70 MPa.[61] However, this approach depends on assumptions of the model, which neglects particle surface morphology and imperfections in the adhesive interface between pollen and polymer. A direct method that does not make assumptions about pollen shape or adhesion with a matrix is preferable for achieving accurate measurements of pollen exine mechanical properties.

Atomic force microscopy (AFM) measures the force on a cantilever tip as a function of its vertical position. The resulting "force-distance (f-d) curves" can be analyzed to determine properties of the material beneath the tip, including adhesion, topography and stiffness.[115] However, these f-d curves can only provide data at one point on the material at a time. The technique of force volume imaging can collect f-d curves from a large number of pixels to create a map of the properties across the sample.[116] Nevertheless, it is typically too slow to map properties over a large sample. To solve this problem, the so-called pulsed force mode was developed in 1997[117]. This technique improves speed by using a relatively fast sinusoidal ramping of the probe. Unfortunately, this also makes material properties measurements less quantitative.[117, 118] Peak force tapping, developed in 2010, reduces mapping time from hours (force volume mode) to minutes (peak force tapping) for a 5 μm x 5 μm area.[119] Meanwhile, it also allows one to measure

the complete f-d curve on each pixel, and precisely control peak force applied to the substrate. This technology enabled a technique known as peak force quantitative nanomechanical property mapping (PFQNM), with which mechanical properties can be mapped as a topological image containing stiffness, adhesion and topography information with nanoscale resolution.[118] By carefully selecting the AFM probe, one can measure elastic moduli from 1 MPa to 100 GPa without destroying the sample. PFQNM mode has been demonstrated to be an effective technique for characterizing both soft and hard materials in the literature, such as living cells,[120] diatoms,[121] polymer composites,[122] cement[123] and steel.[124]

In this Chapter, PFQNM AFM was used as a direct method to measure for the first time the elastic moduli of three types of pollen shells (ragweed, pecan and Kentucky bluegrass). These three types of pollen shells represent a broad variety including common flowering weeds, trees and grasses, covering a range of morphologies from echinate (spines are longer than 1 μm in length) to spinulose (spines are less than 1 μm). Meanwhile, the elastic moduli of pollen shells could be influenced by common chemical treatments and water vapor exposure, important for commercial applications or in the natural environment. Therefore, the ragweed pollen was treated with an acid followed by a base washing, commonly-used for cleaning pollen, to investigate the effect of the treatment on the elastic modulus. Furthermore, the pecan and Kentucky bluegrass moduli were measured after exposure to a 90% relative humidity environment, to understand the effect of water saturation on the elastic modulus.

3.3 Experimental methods

3.3.1 Materials

The native non-defatted pollen grains of three different species were purchased from Greer Laboratories (Lenoir, NC) and stored at 0 °C, including ragweed (*Ambrosia artemisiifolia*), pecan (*Carya illinoinensis*) and Kentucky bluegrass (*Poa pratensis*). Methanol, ethanol and chloroform were purchased from Sigma-Aldrich and used as received. Two types of silicon AFM probes, RTESPA-300 and RTESPA-525, were purchased from Bruker. A set of standard samples (PFQNM-SMPKIT-12M) was obtained from Bruker to calibrate the probes and AFM system. Silicon wafers were purchased from UniversityWafer Inc. (South Boston, MA). Epoxy glues (LOCTITE®, 2 h setting time) were purchased from Henkel Corporation (Rocky Hill, CT) to fix pollen gains on the silicon wafer. Potassium hydroxide (KOH, EMD Millipore) and phosphoric acid (H_3PO_4, BDH chemicals) were used for acid-base treatment.

3.3.2 Sample preparation

Prior to use, the pollen grains were washed with a mixture of chloroform and methanol (3:1), which is a good solvent for the pollenkitt coating on the pollen grains.[45] The washed pollen grains were rinsed with ethanol and dried at ambient conditions (20 °C and 24% relative humidity (RH)) for 24 h. The resulting pollen grains are referred to as the cleaned pollen of ragweed (CPr), pecan (CPp) and Kentucky Bluegrass (CPk), respectively. CPr was further treated with KOH and H_3PO_4 by methods described in detail elsewhere.[61] The resulting ragweed pollen was referred to as acid-base treated ragweed pollen (ABPr) and used to investigate the effect of AB treatment on Young's modulus of

ragweed pollen. In addition, exposure to elevated humidity was studied. CPp and CPk were stored in 90% RH for 24 h to prepare water saturated pollen (WSPp and WSPk). WSPp and WSPk were re-saturated in the 90% RH environment every 30 minutes for 10 minutes during AFM measurements. In order to avoid the movement of the pollen grains during the AFM measurements, pollen grains were glued onto a Piranha-cleaned Si wafer with a thin layer of epoxy resin by using a micromanipulator (NARISHIGE, Japan) and an optical microscope (Olympus BX51).[125]

3.3.3 Scanning electron microscopy (SEM)

Clean pollen grains and ABPr were characterized with a Zeiss Ultra-60 FE-SEM to reveal the morphology. Ethanol suspensions of the pollen grains were deposited by simple drop-casting and dried on silicon wafers at ambient conditions. Then, the silicon wafers were mounted on metal stubs using carbon tape and sputtered with Au/Pd in a Hummer sputtering system to prevent charge build-up during measurement. SEM was also performed on AFM probes before and after mechanical measurements to examine the radii of probe tips. The probes were mounted on metal stubs with carbon tape. The sputtering process was not conducted on the probes so that they could be used for the AFM measurement. All images were obtained under an accelerating voltage of 5.0 kV or 10.0 kV.

3.3.4 Peak Force Quantitative Mechanical Properties Mapping (PFQNM).

The elastic moduli of pollen grains were characterized with PFQNM mode on a Dimension ICON AFM (Bruker). Similar to tapping mode, peak force (PF) tapping intermittently brings the probe and sample together to contact the surface for a short period

at a high frequency (1~2 kHz). Unlike tapping mode where the amplitude of the cantilever vibration is kept constant, PF tapping controls the maximum force (i.e., the peak force) on the tip. While tapping mode is used mainly for imaging topography or qualitatively characterizing mechanical property, PF tapping mode can extract adhesion, modulus and energy dissipation information by analyzing force distance curves at every imaging pixel simultaneously. This allows measurement of the latter data with the same lateral resolution as a topographical image, which is suitable to assess the mechanical properties of micron sized pollen shells.[118]

Figure 3.1a demonstrates what happens during the interaction between the probe tip and a clean ragweed pollen, using data based on the RTESPA-300 probe and CPr. When the modulation frequency of the cantilever is about 1 Hz, the time from point A to point E is about 1 ms, which enables a fast scanning of thousands of contacts between the probe and the sample. As the tip is far away from the sample (point A), there is little or no force on the tip. When approaching the sample, the tip is pulled down to the surface of the sample (point B) by attractive forces (usually van der Waals) as represented by a negative force (below the horizontal dashed line). The tip stays on the surface and the force increases until the *z* position of the probe reaches the bottom-most position at point C, where the peak force occurs. Then, the probe starts to withdraw and the force decreases until the pull-off point (point D), where the adhesion can no longer hold the tip. Once the tip detaches from the surface, the cantilever oscillates for a period and the force is small or zero (point E). Figure 3.1b shows the same data as Figure 3.1a but with the force plotted as a function of the vertical position. This plot can be compared directly with the force-distance (f-d) curve that has been used by many researchers. The f-d curve must be converted to the force-

separation (f-s) curve (Figure 3.1c) to retrieve the mechanical properties, according to equations 3-1 and 3-2, and Figure 3.1d.

$$\Delta x = \frac{F_{tip}}{k} \tag{3-1}$$

$$\Delta d = \Delta z - \Delta x \tag{3-2}$$

In equations 3-1 and 3-2, Δx is the deflection of the cantilever, F_{tip} is the loading force applied on the sample by the probe, k is the spring constant of the cantilever, Δd is the deformation of the sample, and Δz is the distance of the movement of the probe. In Figure 3.1c, the withdrawal curve can be fitted with an appropriate model to obtain the elastic modulus.

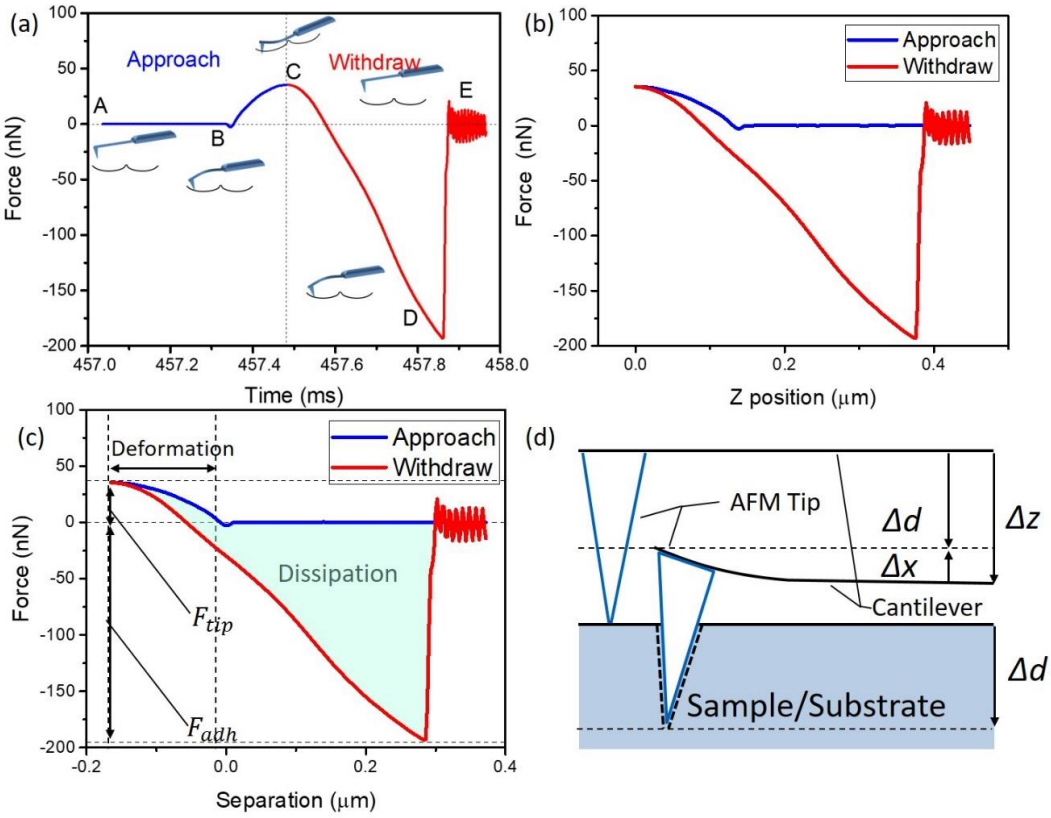

Figure 3.1 (a) Plot of force as a function of time for RTESPA-300 interacting with CPr; the insets are probe-sample I nteractions at different points of the plot, including point (B) jump-to-contact, (C) peak force, (D) pull-off, and (E) free oscillation of the probe after surface detachment; (b) Plot of force as a function of *z* (vertical) piezo position; (c) Plot of force as a function of probe-sample separation distance; (d) An illustration of the relationship between probe deflection (*Δx*) of the probe and sample deformation (*Δd*).

In PFQNM mode, the elastic or Young's modulus is calculated by using the Derjagin-Muller-Toropov (DMT) model to fit the withdrawal portion of the f-s curve.[36] This model is appropriate when deformation of the sample is lower than the tip radius, which is the case presented here. Therefore, DMT model is more suitable for hard materials than the classical Hertz model and the Johnson-Kendall-Roberts (JKR) model.[124, 126] The reduced Young's modulus, E_r, is given by

$$E_r = \frac{3(F_{tip} - F_{adh})}{4\sqrt{R(\Delta d)^3}} \tag{3-3}$$

where F_{adh} is the adhesive force at point D (negative value), and R is the radius of the AFM tip. The tip radius is calibrated by using SEM, a tip calibration grating and standard samples, as discussed in detail in the following section. The reduced elastic modulus is related to the sample elastic modulus, E_s by

$$E_r = \left[\frac{1 - v_s^2}{E_s} + \frac{1 - v_{tip}^2}{E_{tip}}\right]^{-1} \tag{3-4}$$

where v_s and v_{tip} are the Poisson's ratios of the sample and the AFM tip, respectively. In this work, we assume that E_{tip} is much larger than E_s, and so the second term on the right-hand side of equation 3-4 is negligible. For typical values of the silicon modulus (170 GPa) and Poisson ratio (0.22),[127] over the range of moduli values determined below for E_s, this assumption creates 2 % to 7 % difference between E_r and E_s. The Poisson's ratio of polymers generally ranges between 0.2 (very rigid) and 0.5 (rubber), which gives a 4%~25% difference between E_r and E_s.[118] Since we assume that pollen shells have a similar Poisson's ratio to rigid polymers, based on the heavily crosslinked structure of sporopollenin, v_s is set to be 0.35 for the pollen shells in this work. All calculations are done in real time for every f-s curve over the scanned area.

For each measurement, a 5×5 μm^2 area was scanned by the probe, resulting in 512×512 f-s curves, and the average modulus was calculated based upon these individual measurements. A larger magnification (smaller area) was investigated when artifacts were

detected due to the morphology effect, which is discussed in detail in the results section. Five pollen grains were measured for each species, and 2-4 measurements were taken from each pollen grain. Thus, for each type of pollen, the measured modulus and standard deviation were reported based on 10-20 measurements in total. All measurements were conducted at 24% relative humidity and 20 °C.

3.3.5 Probe selection

Considering the pollen shell as a rigid material, probes require a stiff cantilever to apply sufficient force to indent the sample. Two types of Bruker AFM probes, RTESPA-300 and RTESPA-525, were selected according to cover the modulus range from 200 MPa to 20 GPa. Table 3.1 shows some specifications of the probes. The probes need to be calibrated before mapping mechanical property to establish the values of spring constant (k) and tip radius (R).

Table 3.1 AFM probes used in this work.

Probe Type	Tip Material	Nominal Spring Constant (N/m)	Sample Modulus	Reference Sample (Nominal modulus)
RTESPA-300	Silicon	40	0.2-2 GPa	PS (2.7 GPa)
RTESPA-525	Silicon	200	1-20 GPa	HOPG (18.0 GPa)

3.3.6 Probe calibration

Both absolute and relative calibration methods are used to obtain required probe parameters for PFQNM. Based on eqs 1 and 3, E_r is proportional to $k/(R^{1/2})$. The absolute method requires an accurate measurement of R and k. In contrast, the relative method uses a reference sample to force the ratio of $k/(R^{1/2})$ to a known value at a given indentation depth. A combination of both methods was used in this work to ensure the accuracy of the

calibration. Both methods require measurement of the deflection sensitivity on a hard sample. In this work, a sapphire sample (SAPPHIRE-12M) from the PFQNM sample kit was used to obtain the deflection sensitivity. Then, the spring constant was calculated using Sader's method,[128] where the dimensions of the cantilever were obtained using SEM, and the resonant frequency and Q factor were obtained using the thermal tuning function of the AFM. The tip radii before and after AFM measurements were obtained by SEM. The tip radii were also calibrated on a tip characterization sample, RS-12M, from the PFQNM sample kit. For the relative method, polystyrene (PS) and highly oriented pyrolytic graphite (HOPG) films were used as the reference samples (Table 3.1). Although the nominal elastic modulus of PS slightly exceeds the suggested modulus range for RTESPA-300, it is close to the upper limit. Furthermore, the relative method requires that the deformation of the measured samples should be consistent with the deformation of the reference sample. According to the instrument manufacturer, the deformation of both the reference sample and the unknown samples are required to be larger than 2 nm and must be comparable with the deflection of the probe cantilever ($0.3\times\text{deflection} < \text{deformation} < 3\times\text{deflection}$).[118] Otherwise, the probe will be too stiff or too soft for the given samples, which can lead to cumulative errors in following model fitting. In addition, because data from PFQNM are a distribution, a MatLab code was developed and used to rule out data not conforming to these deformation guidelines.

3.4 Results and discussion

3.4.1 Pollen morphology

SEM images of CPr, CPp, CPk and ABPr are shown in Figure 3.2. Grooves and tiny pores can be observed, demonstrating that the pollenkitt has been eliminated by washing with the methanol/chloroform mixture. Acid-base treatment does not have a significant impact on the morphology. The dimensions of the pollen grains are shown in Table 3.2. CPp has small bumps sparsely distributed on the surface. While CPr and ABPr have very large spines and tiny pores. CPk also has similar bumps as CPp, but the bumps of CPk are much denser than that of CPp. In addition, CPp and CPk sometimes have folded or collapsed shells. Features including spines, pores, bumps, and folds were carefully avoided in AFM measurement and results below are based on relatively flat, featureless areas.

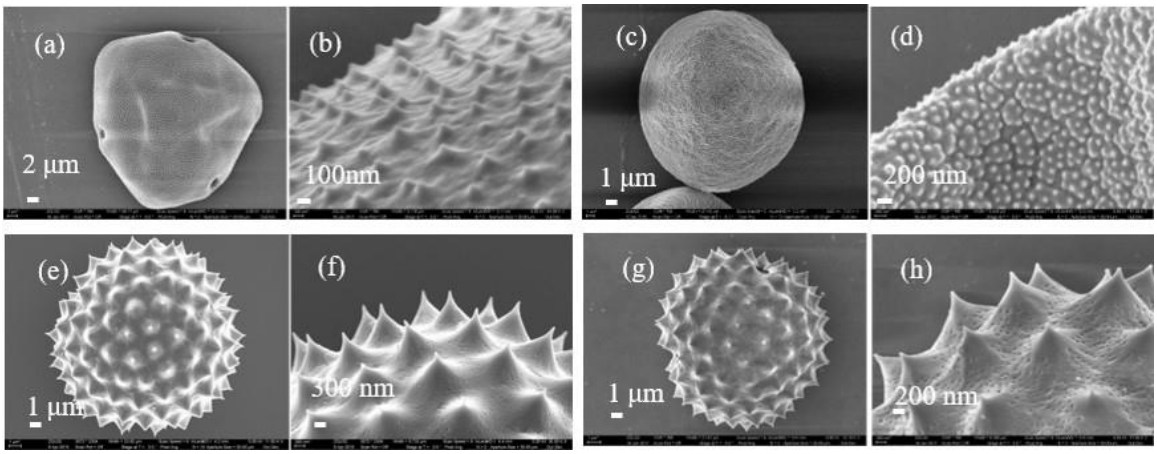

Figure 3.2 SEM images of the clean pollen shells of (a), (b) pecan (CPp); (c), (d) Kentucky bluegrass (CPk); (e), (f) ragweed (CPr), and (g), (h) acid-base treated ragweed pollen (ABPr).

Table 3.2 Dimensions of pollen grains

Type	Diameter /μm	Length of spine /nm	Radius of spine /nm
CPp	38 ± 2	190-240	45 ± 4
CPk	26 ± 3	80-130	57 ± 12
CPr	15 ± 3	500-1000	52 ± 5
ABPr	15 ± 3	500-1000	52 ± 5

3.4.2 Probe calibration

First, the absolute method was used to measure the spring constant of the cantilever (k). Then, this parameter k was used in the relative method to estimate the tip radius (R) by measuring the modulus of a reference sample (PS or HOPG). Although the absolute

method also gives an estimation of the tip radius, the relative method avoids the accumulative errors caused by the imperfect tip shape. Thus, the spring constant (the absolute method) and tip radius (the relative method) were used as adjustable parameters to fit the DMT model. To begin with, the deflection sensitivity was calibrated on the sapphire surface as described above. Then, the dimensions of the two probe types were measured using SEM (Figure 3.3a, b). The dimensions, resonant frequency and Q factor were used to calculate the spring constants (k) with Sader's method ('absolute' technique). This method was reported to have the least uncertainty, which mainly comes from the errors of the measurement of the cantilever width.[129] Then, a standardized tip characterization sample was scanned by AFM to estimate the tip radius of the probe using the tip reconstruction model. Next, the relative calibration method was performed. In this approach, PS and HOPG were scanned by RTESPA-300 and RTESPA-525, respectively. The tip radius (R) was adjusted in the NanoScope software until the measured modulus matched the nominal modulus of PS or HOPG. Table 3.3 shows the tip radii measured with the different methods before and after measuring five pollen grains. Before the AFM measurements of pollen samples, the difference in radii comparing the SEM images to the results of absolute or relative calibration is due to wear that occurred during the calibration. The discrepancy between the absolute method and the relative method is mainly because of the imperfect tip shape, which deviates from the spherical tip shape assumption of the DMT model. However, after measuring five pollen grains, SEM images show much higher tip radii than the results measured with the relative method. This is because only a small portion of the blunt tip is contacting the sample during AFM measurement, and the smaller contacting radius is what is relevant to the measurement of modulus values. After

measuring each individual pollen grain, the probe scanned PS or HOPG sample again to check for drift in the modulus that could indicate tip damage. If the average moduli of PS or HOPG was consistent with the nominal value, the probe was used to measure the next pollen grain. Otherwise, the tip radius was adjusted in the software to match the measured moduli of PS or HOPG with the nominal modulus values. Figure 3.4 shows the measured moduli of PS and HOPG before and after the tips were used to characterize five pollen grains. The measured moduli of PS and HOPG drifted from 2.67 GPa and 17.8 GPa to 3.14 GPa and 23.4 GPa, due to the wear on the tip. SEM confirmed the wear on the tip that occurs after measuring five pollen grains (Figure 3.3c, d). The blunter tips lead to a shorter indentation depth (d) and the calculated modulus will be higher according to equation 3-3. Correcting the tip radius to achieve the nominal modulus value accounts for changes in tip radius during measurement. In contrast, the surfaces of the calibration standards and the pollens do not show readily apparent wear following indentation measurements.

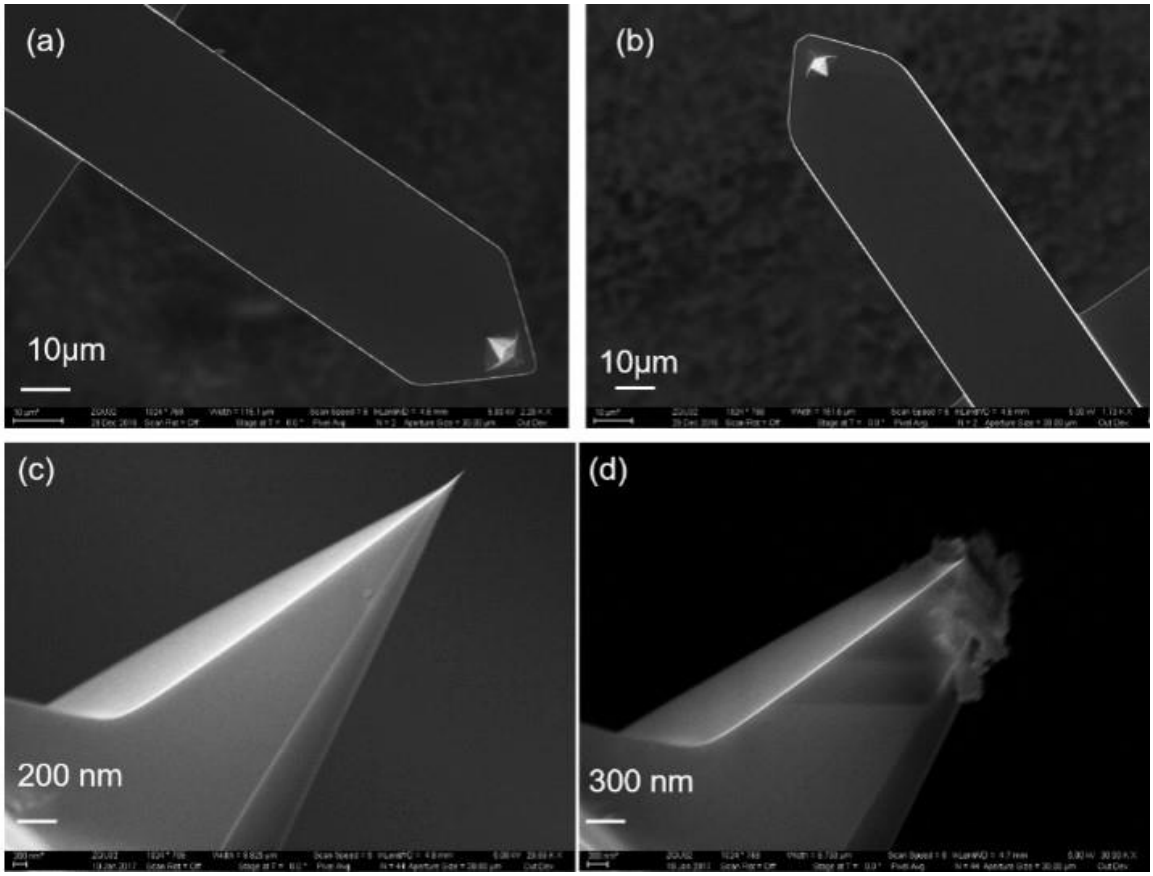

Figure 3.3 SEM images of (a) RTESPA-300 (b) RTESPA-525 probes before measuring 5 pollen grains; (c) the tip of RTESPA-525 before the calibration; (d) the tip of RTESPA-525 after testing 5 pollen grains.

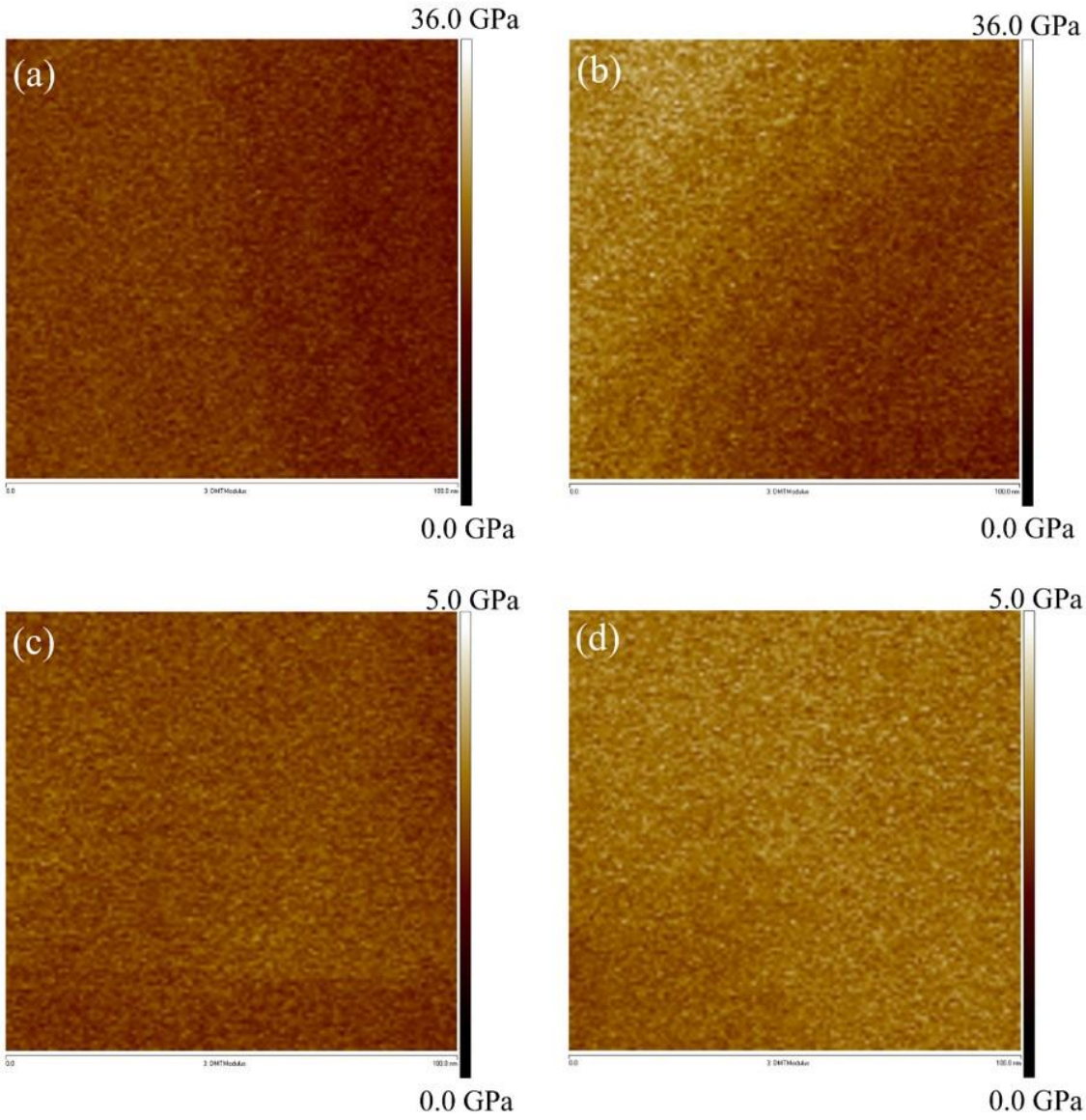

Figure 3.4 The moduli maps of (a) HOPG with new RTESPA-525, (b) HOPG with used RTESPA-525, (c) PS with new RTESPA-300 and (d) PS with used RTESPA-300; all images are 100nm x 100nm.

Table 3.3 Tip radii measured or estimated by different methods before and after AFM measurement of pollens.

	Probe	SEM /nm	Absolute method /nm	Relative method /nm
Before	RTESPA-300	10	20.7	50
	RTESPA-525	10	23.4	60
After	RTESPA-300	N/A	N/A	160
	RTESPA-525	650	N/A	210

3.4.3 Morphology effect

As preliminary experiments, the RTESPA-300 probe was used to scan 5×5 μm^2 areas on CPp, CPk, CPr and ABPr by AFM. Multiple channels were recording the topological and mechanical properties of the sample in real time. For example, Figure 3.5 shows the height, 3-D height, adhesion, deformation and modulus maps of ABPr. The 3-D height image shows 4 intact spines, as well as several half spines at the edges. Moreover, tiny pores and grooves on the pollen surface can even be observed from the 3-D height and deformation images. Correlations can be found between the height images and the other mechanical property maps. For the deformation image, the area surrounding the tips of spines showed larger deformation (lighter color on the map) than the other areas. Consequently, the moduli of those areas were much lower than the other areas according to equation 3-3. This contrast is more likely due to the spiny morphology rather than the intrinsic heterogeneity of the moduli of pollen shell. As shown in Figure 3.5f, the surface near the tip of the spine was much steeper compared to the horizontal surface between spines. When the probe taps this steep surface, it is easy to slip down the surface. The slip can only happen after contact point (point B in Figure 3.1a), thus the slipping distance will be mistakenly accounted for as deformation of the sample by the DMT model. In addition, the DMT model assumes that the interaction is between a sphere and a flat surface. Thus,

the DMT model does not hold when the tip is tapping the steep surfaces around the spines. Adhesion maps also showed remarkable correlations with the spiny morphology.

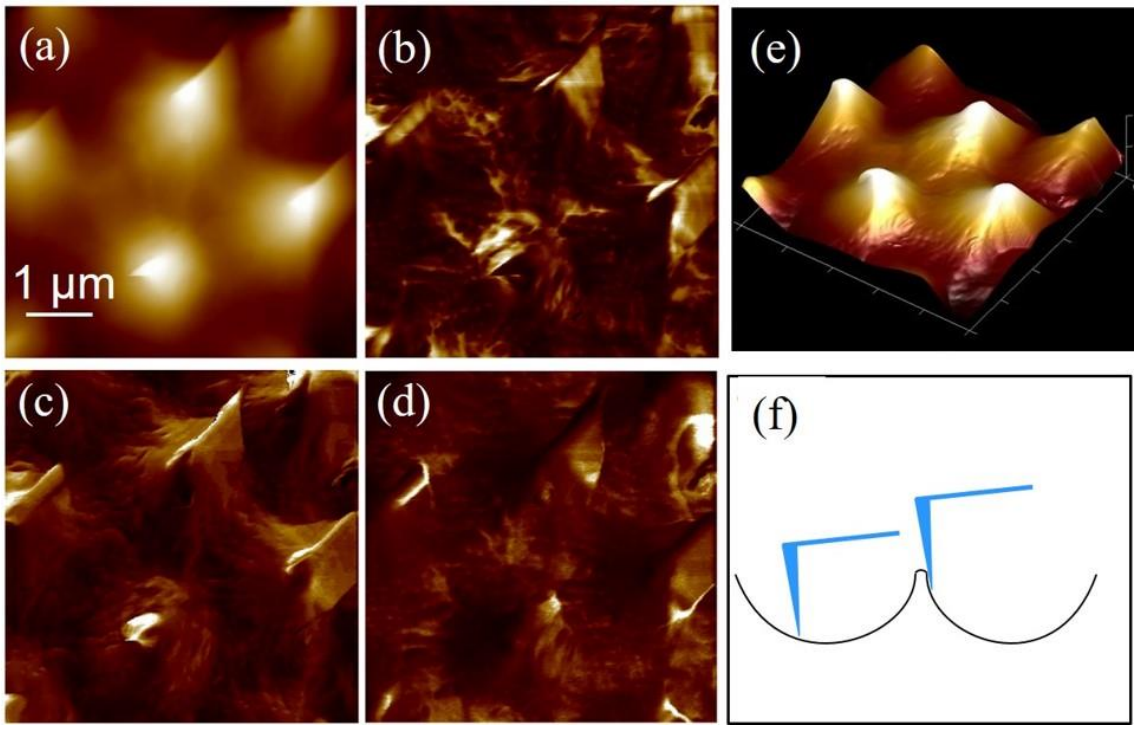

Figure 3.5 AFM images of ABPr: (a) height, (b) deformation, (c) adhesion, (d) modulus, (e) 3-D height and (f) an illustration of the probe-pollen interaction.

The adhesion forces at the area surrounding the tip of the spine are much higher than the adhesion forces at the tip of the spine and the spacing between spines. This may be due to the difference of contact areas formed at different locations. When the probe taps the apex of the spine, the tip of the probe can only make a small contact area, depending on the size of the probe-tip and spine-apex. However, when the probe taps the steep side surface around the spine's apex, it could achieve much larger contact area by contacting with the spine side-by-side. Therefore, the adhesion forces around the spine apex could be larger than the adhesion forces at the apex or the space between spines. It is noted that large adhesion forces were also observed at some grooves or pores of the pollen shell. This could

also be due to the larger contact areas formed when the probe taps and even inserts into those specific morphologies. Similar morphology effects were also reported in the literature for modulus mapping of individual chitin nanorods with PFQNM.[126, 130]

The other three types of pollen also showed similar morphology effects on the mechanical characterization. Although CPp and CPk (Figure 3.2) have less morphology effect due to their smaller bumps than ragweed pollen, the modulus data over spines and bumps are not included in the following data analysis, to avoid potential artifacts caused by the morphology issue. After a 5×5 μm^2 area was scanned first to yield a morphology map, smaller portions of the 5×5 μm^2 area without spines or bumps were rescanned to obtain mechanical properties.

3.4.4 Probe effect

The elastic moduli of pollen shells are still largely unexplored in the literature. Only one paper reported the product of the Young's modulus and wall thickness ($E \cdot h$) of desiccated ragweed pollen as 1653 ± 36 N/m.[60] This value is based upon the mean rupture force and deformation of the ragweed pollen under compression. An accurate average modulus can be obtained only if the wall thickness is known accurately. If the thickness of the pollen shell is taken to be ~1 μm based upon SEM images in the literature, the Young's modulus will be about 1.6 GPa.[61] Therefore, the RTESPA-300 probe, with a suggested sample modulus of 20 to 2000 MPa, was chosen for the characterization. Figure 3.6a shows the average elastic moduli of CPp, CPk, CPr and ABPr measured by using RTESPA-300. ABPr has the lowest modulus of 1.46 ± 0.38 GPa, while CPr shows a much higher modulus of 8.45 ± 0.43 GPa without acid-base treatment. CPk and CPp show

relatively large moduli of 8.70 ± 1.15 GPa and 7.54 ± 2.72 GPa, respectively. The smaller sample size of CPr and ABPr is due to the morphology of ragweed pollen. The long spines make it difficult to get usable data on every ragweed pollen. It is noted that all results except for ABPr exceed the suggested moduli range of RTESPA-300. Moreover, most of the deformation data of these samples are below 2 nm. Small deformation indicates that RTESPA-300 is too soft to make a significant indentation on the pollen shell. Therefore, RTESPA-300 is not a suitable probe for CPr, CPp and CPk.

Since RTESPA-300 was not appropriate, a stiffer probe, RTESPA-525, was used for AFM measurement. Figure 3.6a shows the moduli of the pollen grains measured by RTESPA-300 and RTESPA-525, respectively. The moduli measured by RTESPA-525 are between 1 and 20 GPa, which is the suggested sample moduli range of the probe. The deformations are sufficient and comparable with the deflections for fitting the DMT model (Figure 3.6b). Hence, the results from RTESPA-525 were more reliable than those from RTESPA-300. Overall, higher elastic moduli were obtained with RTESPA-525 for CPp and CPk. With RTESPA-525, the average moduli of CPr, CPk and CPp is 16.2 ± 2.45 GPa, 16.1 ± 3.96 GPa and 9.53 ± 2.33 GPa, respectively. Thus, the moduli of CPr, CPk and CPp are even higher than most non-reinforced polymers.[131] It is interesting that the moduli are close to the elastic moduli of phenolic plastics, and phenolic compounds were found in sporopollenin.[132] The high elastic moduli indicates the great potential of pollen shells to be used as a polymer reinforcing filler with the advantages such as low density, low cost, bio-renewability and ready surface modification.[61] It is noted that these two types of probes give similar results for CPp with a difference of 2 GPa, as well as overlapped error bars. It indicates that RTESPA-300 could be used for some samples (CPp) with higher

moduli than the range suggested by Bruker, even though RTESPA-525 is a better choice in this work.

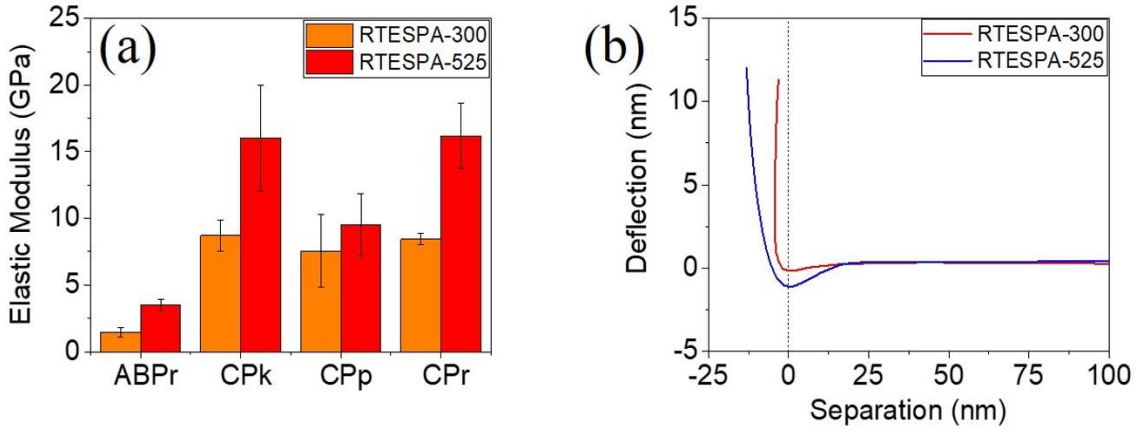

Figure 3.6 (a) The average moduli of ABPr, CPk, CPp and CPr by RTESPA-300 and RTESPA-500. (b) The deflection versus separation curves of RTESPA-300 and RTESPA-525 used to fit the DMT model; data were taken with a clean ragweed pollen as a representative.

3.4.5 Effect of acid-base Treatment

In Figure 3.6a, both RTESPA-300 and RTESPA-525 gave higher moduli for CPr comparing with ABPr. The moduli of ABPr decreased by 82.7% and 78.4% using RTESPA-300 and RTESPA-525, respectively. The results indicate that the acid-base treatment can reduce the stiffness of pollen shells by about 50%, whilst the morphology can be maintained. Synthetic polyester polymer has been reported to show a similar effect with respect to acid-alkali treatment, where the Young's modulus of polyester fiber was reduced by 41% (acid treated) and 28% (alkali treated).[133] Considering the cross-linked structure of sporopollenin by ester bonds, this reduction is presumed to be due to the degradation of the macromolecular network through hydrolysis. Although the acid-base treatment can reduce the elastic moduli of pollen shells, ABPr shows higher moduli than

some common polymers. Therefore, ABPr can still be useful for reinforcing polymer matrices, which is important because the acid-base treatment has been shown to facilitate the surface modification of pollen shells and their compatibilization with polymers. This is consistent with results of Fadiran et al., who used AB treatment of Pr as a precursor to silanization of pollens with vinylsilane coupling agents to prepare Pr-poly(vinylacetate) reinforced composites.[61]

3.4.6 Effect of water vapor exposure

In previous work by Lin et al.,[134] it was shown that cleaned ragweed pollen can become saturated with water as humidity is raised, through both adsorption and absorption. It was found that ragweed gained water in the amount of 16% dry mass at a humidity of 70%. As described above, ragweed pollens are more difficult to be characterized by AFM than pecan and Kentucky bluegrass due to the spiny morphology. Therefore, only CPp and CPk were used to investigate the effect of exposure to water via elevated humidity. The same samples of CPp and CPk that were measured previously by the RTESPA-525 tip at normal room humidity were stored in a 90% relative humidity environment for 24 h. Then, the resulting water-saturated pecan and Kentucky bluegrass pollen (WSPp and WSPk) were measured quickly with AFM while holding RH at 24% RH to avoid water condensation during measurements. WSPp and WSPk were also re-saturated at 90% RH every 30 minutes during the experiment. Figure 3.7 shows the average moduli of WSPp, CPp, WSPk and CPk measured with probe RTESPA-525. CPp and CPk show average moduli higher than 10 GPa. However, both WSPp and WSPk show reduced moduli of 4.37 ± 1.96 GPa and 4.45 ± 1.24 GPa, respectively. In comparison with CPp and CPk, these values correspond to a decrease of 54.1% (WSPp) and 72.3% (WSPk), a result that indicates that while water

saturation reduced the stiffness of the pollen shells, the moduli still exceed 4 GPa. The topological image (Figure 3.8) of WSPk also showed a different morphology comparing with CPk. CPk has a relatively smooth surface compared to WSPk, which may be due to leveling of bumps following the swelling of the sporopollenin with water.

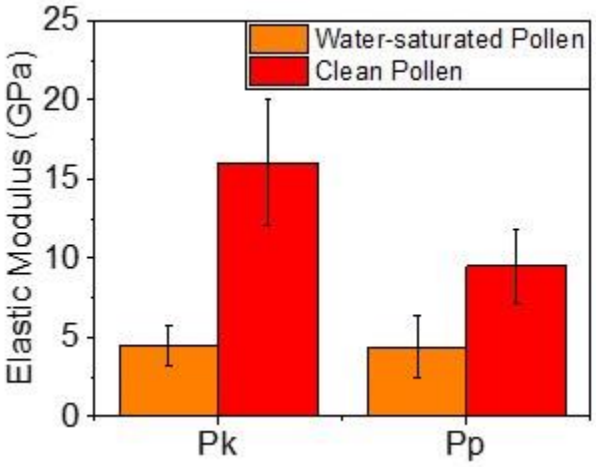

Figure 3.7 The average moduli of WSPk and WSPp compared with the moduli of CPk and CPp.

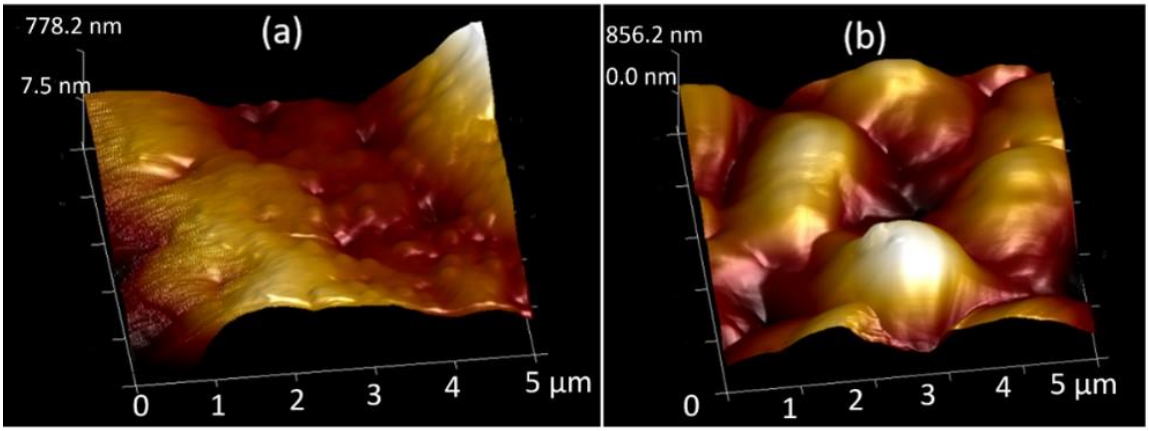

Figure 3.8 3D-height images of (a) CPk and (b) WSPk by RTESPA-525.

One concern for the experiment is whether absorbed water will affect PFQNM by introducing capillary adhesion. At high humidity (70% RH), the water taken up by the

pollen exine is mainly absorbed by the bulk sporopollenin according to Lin et al.[134] Only 25% of water is adsorbed on the surface or condensed in small cavities. However, in this work, pollen shells are only pre-stored in high humidity. The experiments were still conducted in air a 24 % RH, where additional water condensation between tip and pollen is unlikely.[135] Moreover, the loading force of the cantilever is 1~2 μN, whilst the capillary force is only tens of nano-Newton at the most. In other words, even if a capillary or pendular bridge is formed in the probe-sample interaction, it will only have a small effect on the modulus measurement according to equation 3-3.

3.4.7 Comparison with other biomaterials

As non-crystalline materials,[136] sporopollenin showed surprisingly high elastic modulus at dry condition, comparing with other amorphous, neat biomaterials. Table 3.4 shows the Young's moduli of several biomaterials, including protein fibers from animals, hemicellulose and lignin from plants. In general, the plant polymers show higher Young's moduli than the animal ones. At dry condition, sporopollenin has the highest Young's moduli, 16.2 GPa for ragweed and Kentucky Bluegrass, and 9.53 GPa for pecan. The second highest moduli are 6.7 GPa (lignin) and 6.0 GPa (β-glucan), which are 2.7 and 2.4 times less than ragweed pollen exine. Animal proteins (actin, tubulin and collagen) and arabinoxylan have the lowest Young's moduli between 1 and 3 GPa. It is worth noting that sporopollenin bears some resemblance to lignin, where both sporopollenin and lignin have similar precursors (ferulic acid, phenylalanine, etc.) and phenolic ester/ether cross linking. In addition, lignin has the similar effect of elevated water content. The Young's modulus of lignin decreased by 54% (from 6.7 GPa to 3.1 GPa), when the water content increased from 3.2 wt.% to 12 wt.%. Meanwhile, the moduli of pecan and Kentucky bluegrass pollen

exine decreased by 54.1% and 72.3%, when the environment relative humidity increased from 24% to 90%. In addition, the hydration effect of pollen exine indicates the amorphous structure of sporopollenin, which is already confirmed with X-ray diffraction.[136]

Table 3.4 Young's modulus of representative biomaterials.

Material	Young's Modulus /GPa	Method	Reference
Actin Tubulin	1.8 1.2	Nanomanipulation Thermal fluctuation	[137] [138]
Lignin	6.7 (3.2% water) 3.1 (12% water)	Tensile test	[139]
Hemicelluloses Arabinoxylan β-glucan	 1.3, 2.9 6.0	 Tensile test Tensile test	[140], [141] [142]
Collagen	2.7, 4.59	AFM Manipulation	[143], [144]
Sporopollenin	9.5 - 16 (24% RH) 4.4 (90% RH)	AFM PFQNM	This work

3.5 Conclusion

For the first time, the elastic moduli of three types of pollen exine (shells) were measured directly by using AFM peak force quantitative nanomechanical mapping. Kentucky blue grass and ragweed pollens had moduli of 16 GPa, while pecan particles had a lower modulus between 8 and 10 GPa. In addition, sporopollenin was observed to be a very tough material qualitatively, and did not sustain any visible damage by SEM inspection even after multiple indentations with much stiffer silicon AFM tips. In contrast, silicon AFM tips were readily abraded after indentation on sporopollenin. An acid-base treatment commonly used to clean and process pollen reduced the modulus of ragweed pollen from 16 ± 2.5 GPa to 3.5 ± 0.5 GPa. Furthermore, water vapor saturation at elevated

humidity of 90% decreased the moduli of pecan and Kentucky blue grass pollens by 54.1% and 72.3%, respectively. This sensitivity is consistent with prior observations of water absorption by sporopollenin[134] and is similar to that observed for other natural amorphous biological materials[139]. In addition, AFM images indicate the swelling of sporopollenin after water vapor exposure. Overall, we conclude that that sporopollenin is an unusually stiff biomaterial, with a modulus that exceeds most other non-crystalline biomaterials. High stiffness likely supports adhesive functions of pollen exine, particularly when pollens are pressed onto other patterned substrates.[46] For example, it was shown recently that pollen spines can lock onto similarly-sized features on flower stigma surfaces, resulting in pressure-dependent adhesion behavior. Stiff sporopollenin features support the appearance of load-dependent frictional forces as stigma hairs are forced in between the pollen spines. These results also indicate the potential of pollen particle exine shells as relatively stiff materials that can be used in applications such as reinforcing fillers for polymers[61] and protective shells for sensitive materials such as drugs.[110]

CHAPTER 4. ACRYLIC FUNCTIONALIZATION OF CELLULOSE NANOCRYSTALS WITH 2-ISOCYANATOETHYL METHACRYLATE

4.1 Overview

Cellulose nanocrystals (CNCs) exhibit a great potential as a filler for reinforcing polymer matrices due to their superior properties, such as high specific strength, low density, renewability and sustainability. However, CNCs also have drawbacks including hydrophilicity and low thermal stability, which lead to poor particle-matrix adhesion and limit the processing and application in the polymer composites industry. In this chapter, a versatile chemical modification route was investigated to introduce acrylic functional groups on the CNC surface for potential applications with acrylic polymer. The CNC hydroxyl group was utilized to react with a bifunctional molecule possessing both an isocyanate group and an acryloyl group. The resulting modified CNCs (m-CNCs) showed enhanced hydrophobicity and could be dispersed in the polar organic solvent dimethylformamide (DMF). Fourier transform infrared spectrometry, X-ray photoelectron spectroscopy, solid state ^{13}C NMR, and elemental analysis verified the surface modification. X-ray diffraction indicated the retained crystalline structure of m-CNCs, and thermogravimetric analysis showed enhanced thermal stability of m-CNCs relative to unmodified CNCs (um-CNCs). This modification method was an effective approach to covalently attach acrylic moieties to CNCs, which is expected to allow them to be used as reinforcing agents in acrylic or other polymer composites, or stabilizers and rheological modifiers in polymer products.

4.2 Introduction

Cellulose nanocrystals (CNCs), produced by separating crystalline cellulose from amorphous regions via hydrolysis of cotton, wood pulp or other cellulose sources, have many excellent properties, such as high specific mechanical strength and modulus, nanoscale dimensions, low density and a high aspect ratio[66]. The hydrolysis process renders the surface of CNCs with hydroxyl groups, some of which are sulfonated due to the use of sulfuric acid in the process. Although the hydrophilicity of these CNC surfaces is attractive for water-based systems, it raised great challenges in terms of the poor dispersity and poor interfacial adhesion for applications in organic nonpolar solvents and hydrophobic polymer matrices[145]. It can be difficult to disperse charged sulfonated CNCs even in some polar organic solvents.

Due to the superior properties, renewability and sustainability of CNCs, there has been a significant interest in recent years in utilizing CNCs to improve the mechanical properties and durability of polymers, including those based on polyurethanes [146], epoxy [147-150], acrylic/urethanes [151, 152], and UV-cured wood varnishes [153]. For example, it was reported in 2016 that cellulose nanofibers (CNFs) were modified with an aminosilane and then added to a commercial waterborne acrylic/urethane coating [152]. In that work, the CNFs were designed to disperse in an aqueous medium and then become physically incorporated into the coalescing polymer droplets during drying. There is a possibility that the CNFs may have reacted into the final film structure via amine-alkyd coupling, but this is not clear from the published data. The prior art does provide evidence of the promise of incorporating cellulose nanomaterials (CNs) into waterborne acrylic coatings. The cured films with up to 20 wt.% CNF showed 90% transmittance of visible

light, 5x increased modulus, 2x increased hardness, and a 35% improvement in abrasion resistance. In a different study with acrylic/urethane waterborne coatings and unmodified CNCs, these properties showed only minimal improvements, and the CNC was found to act as a matting agent, reducing gloss.[151]

The literature describes many methods for introducing hydrophobic groups to cellulose polymers [154] and more recently to CNF and CNC surfaces [155-157] to promote compatibility with more hydrophobic polymer matrices. The most common surface modification techniques are graft copolymerization by free radical mechanisms [154, 156-158], functionalization via silylation of the –OH group [159-161], and modification by adsorbed surfactants [155]. It was reported in 1960 that vinyl monomer was grafted onto starch, initiated by ceric salt [162]. The primary prior art related to vinyl modification of CNCs is based on using ceric ammonium nitrate to initiate the graft copolymerization of vinyl monomers from the CNC surface [156]. Various monomers can be graft copolymerized onto CNCs including methyl methacrylate, methacrylate, acrylic acid, vinyl acetate and acrylamide. The resulting CNC/acrylic nanocomposites showed enhanced thermal stability and mechanical properties [157]. These grafting methods utilized the polymerization initiated from the cellulose –OH sites with a free radical mechanism. Thus, it is always an oligomer or polymer that is being added to the CNC/CNF surface.

In contrast to the common ceric salt grafting method, in this chapter a chemical surface modification method was developed by grafting a single acrylic functional monomer to the CNC surface, via covalent bonding with an –OH group. This is accomplished by grafting acrylic monomers via an acrylic isocyanate. The acrylic-

modified CNCs are separated as a product with enhanced hydrophobicity and dispersity in organic solvents. The method developed in this chapter is expected to be broadly applicable across many classes of acrylic materials and cellulose-containing particles and polymers.

4.3 Experimental methods

4.3.1 Materials

Freeze-dried CNCs (FD-CNCs) were provided by USDA Forest Products Laboratory and used as received. The CNCs were freeze dried from an aqueous CNC suspension prepared from mixed southern yellow pine dissolving pulp via 64% sulfuric acid digestion as described in detail elsewhere.[65] The FD-CNCs were determined to contain 0.96% sulfur as residual sulfate esters. The counter ion to the sulfate esters was Na^+. The bi-functional modifier molecule, 2-isocyanatoethyl methacrylate (IEM), was purchased from TCI America, stabilized with butyl hydroxytoluene at >98% purity. Dimethyl sulfoxide (DMSO, anhydrous, ≥99.9%), dimethylformamide (DMF, anhydrous, 99.8%), and isocyanate catalyst, DBTDL, were purchased from Sigma-Aldrich and used as received. Molecular sieves (MS, type 3A, EMD Millipore MX 1583D-1) and toluene (ACS, 99.5%) were purchased from Alfa Aesar and used as received. The chemical structures of the primary materials are shown in Figure 4.1.

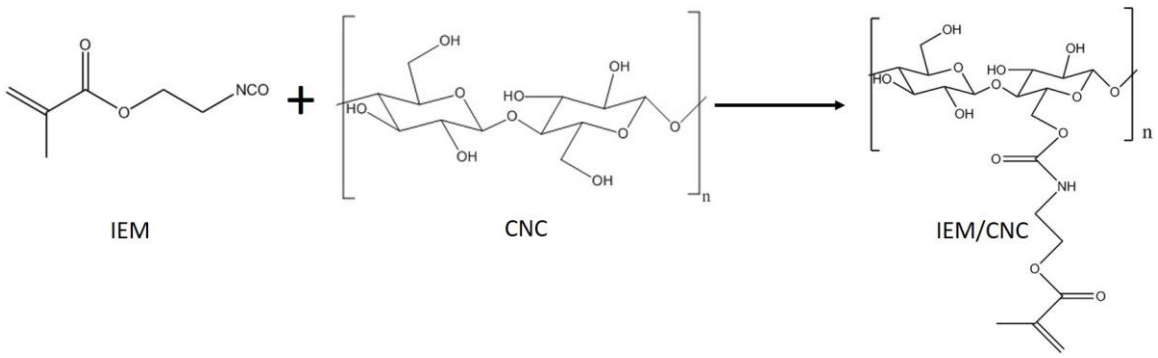

Figure 4.1 Illustration of IEM and CNC reaction.

4.3.2 Preparation of IEM-CNC

The FD-CNCs (0.4 g) were first mixed with anhydrous DMSO (17 g) in a 40-mL glass vial by vortex mixing. DMSO was dried by molecular sieves for 1 h before using. The concentration of FD-CNCs in DMSO was ~2.3 wt%. The suspension of CNCs was then sonicated for 1.5 h in a 2510 Branson bath sonicator. After the sonication, the suspension appeared transparent, which indicated that the CNCs were dispersed homogeneously in DMSO. The suspension was then heated to 60 °C with magnetic stirring. Next, IEM (2.5 g) was added into a separate glass vial to premix with DBTDL (30 µL). The IEM was added in excess at a molar ratio of IEM to AGU of CNCs as 6.5:1. The IEM/DBTDL mixture was added dropwise into the CNC/DMSO suspension. The reaction was then carried out at 60 °C for 2 h. After the reaction was completed, the mixture was separated into four equal parts. Each part was precipitated and washed with toluene and centrifuged at 3000 rpm for 10 min. This process was repeated three times. The IEM/CNC settled down at the bottom of the vial appeared as a smooth and clear organogel (IEM-CNC/Toluene).

4.3.3 Attenuated total reflectance fourier transform infrared spectroscopy (ATR-FTIR).

Unmodified CNCs (um-CNC), modified CNCs (m-CNCs) and IEM were analyzed by ATR-FTIR to characterize their chemical structures. The equipment is a Bruker Vertex 80 V spectrometer with ATR accessory (Bruker Platinum ATR). The wavenumber scan range was from 4000 cm^{-1} to 600 cm^{-1} with a resolution of 4 cm^{-1} and a total of 64 scans. For the um-CNCs and m-CNCs, the spectra were normalized at the 1060 cm^{-1} peak since this absorbance was associated with ether groups, which were assumed to not participate in the reaction.

4.3.4 X-ray photoelectron spectroscopy (XPS).

Both um-CNCs and m-CNCs were analyzed using a Thermo K-Alpha X-ray photoelectron spectrometer. Powder form samples were radiated with a source of monochromatized Al Kα (1486.7 eV) with a 45° takeoff angle, a 400 μm beam size, and a 50 W power. The chemical shifts were taken from the literature, and the spectra were corrected by setting the C−C contribution in the C 1s emission at 285.0 eV.

4.3.5 Solid state ^{13}C NMR

The chemical structure and the degree of substitution were also characterized with solid-state 13C NMR. Approximately 50 mg of um-CNC and m-CNC was packed into a 24 mm OD MAS rotor. CP-MAS spectra were recorded using a Bruker AV3−400 NMR spectrometer operating at a 1 H frequency of 400 MHz. A dual channel BB-MAS probe was operated at a spinning speed of 10 kHz. Cross-polarization was achieved with a trapezoidal shaped contact pulse for 1 H varying in power from 70 to 100% and a length of 2 ms. Repetition delay between scans was 4 s, and at least 12 000 scans were acquired for each sample to measure spectra with an excellent signal to noise ratio. The spectra were

normalized by the peak positioned at $\delta = 75$ ppm, an absorbance that was attributed to the C2, C3, and C5 carbons in the crystalline cellulose, which were assumed to not participate in the reaction.[163]

4.3.6 Elemental analysis.

Elemental analysis was conducted by ALS Environmental in Tuscon, AZ for both um-CNCs and m-CNCs samples. The samples were analysed for C, H, O, and N content. The C, H, and N content was analysed with a PerkinElmer 2400 Series II, and O content was analysed with a Leco Truspec Analyzer. The PerkinElmer instrument was calibrated with acetanilide, and the Leco Truspec was calibrated with benzylic acid. Approximately 2 to 5 mg of sample was weighed and then held in the combustion chamber for about 5 min. The oxygen analyzer was held at 1000 °C and the C, H, N analyser was held at 935 °C. The degree of substitution was calculated based on the nitrogen content.

4.3.7 X-ray diffraction (XRD)

The crystalline structure of CNCs was examined with XRD analysis before and after the modification. XRD analysis was performed on a Panalytical XPert PRO MRD XRD system. Diffractograms were recorded over an angular range of $2\theta = 5{-}70°$ and a step size of 0.008356° with Cu Kα ($\lambda = 1.54$ Å) radiation generated at an anode voltage and current of 45 kV and 40 mA, respectively.

4.3.8 Thermogravimetric analysis (TGA)

Thermal stability and changes in degradation patterns associated with the modification step were assessed with thermogravimetric analysis (TGA; TA Instruments

TGA Q5000). Freeze dried um-CNC and m-CNC were characterized. In addition, the disperse-washing procedure during the modification with DMSO and toluene was also conducted on um-CNCs. The resulted "Washed um-CNC" was also tested to examine the effect of washing process[164]. All samples were dried at 50 °C for 24 h before testing. Samples were heated from 50 °C to 600 °C at a rate of 5 °C/min under a flowing nitrogen atmosphere. The onset temperature (T-onset) was determined with TA Universal Analysis software. The onset temperature of degradation was assessed by TA Universal Analysis software by manually choosing a point before and after the sharp drop in mass loss on the weight loss curve.

4.3.9 Contact angle measurement

In order to characterize the change of hydrophilicity of CNCs associated with the modification, contact angles of um-CNCs and m-CNCs were measured with water as the test liquid at 20 °C using a video contact angle system (Rame-Hart goniometer). Unmodified CNC film was prepared by depositing drops of the aqueous um-CNC suspension onto a piranha-cleaned silicon wafer, followed by drying at ambient condition for 24 h. Modified CNC film was also prepared with the drop coating method with the toluene/m-CNC suspension.

4.4 Results and discussion

4.4.1 Characterizing the chemistry of modified CNCs

To verify the attachment of IEM to CNCs surface with the hydroxyl/isocyanate chemistry as showed in Figure 4.1, ATR-FTIR was used to characterize both um-CNCs

and m-CNC. Figure 4.2 showed the ATR-FTIR spectra of um-CNCs, m-CNCs and IEM, where the spectra of um-CNCs and m-CNCs were normalized at 1060 cm^{-1}[72]. The um-CNCs showed absorbances of characteristic cellulosic functional groups. The strong absorbance at 3000-3600 cm^{-1} and multiple peaks around 900-1100 cm^{-1} are associated with -OH and -C-O-C- vibrations, respectively. In the spectra of IEM, two strong absorption peaks were observed at 2240 cm^{-1} and 1723 cm^{-1}, representing the -N=C=O stretching and -C=O group stretching, respectively. A small peak at 1640 cm^{-1} represents the alkenyl C=C stretch in IEM. Changes were observed for m-CNC in almost all regions of the spectra. First, strong absorptions at 1723 cm^{-1} and 1640 cm^{-1} verified the attachment of C=O and C=C groups on CNCs. In addition, the multiple absorption peaks between 1200 cm^{-1} and 1700 cm^{-1} are associated with urethane linkage. The small increment of the absorption between 2900 cm^{-1} and 3000 cm^{-1} also indicates the increased sp3 C-H stretch by the methyl group of IEM. The results suggested that the acrylic function group has been attached on CNCs surface via a urethane linkage formed by the reaction between hydroxyl and isocyanate group reaction.

Further support for the modification reaction was provided with XPS characterization. Figure 4.3 showed the wide-scan XPS spectra of um-CNCs and m-CNCs. The major components before surface modification were carbon and oxygen with a trace of sulfur from the sulfate half ester groups. A nitrogen peak appeared due to the attachment of IEM

on CNCs surface after the modification reaction. The atomic ratios of C, O, and N were 79.07%, 18.51% and 2.43%, respectively.

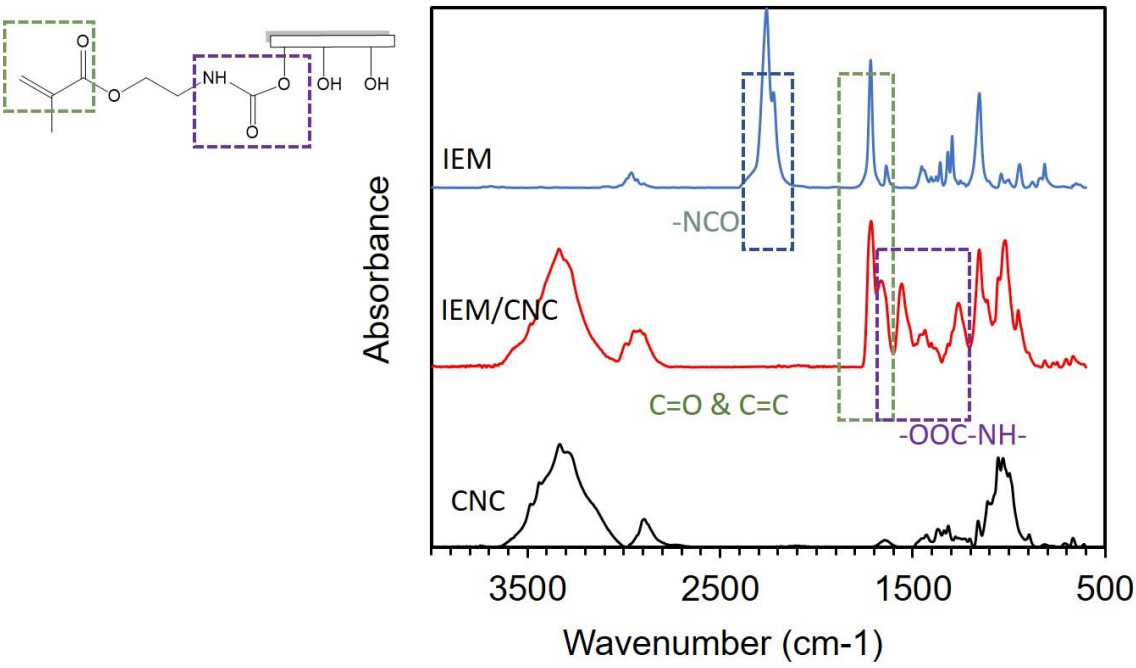

Figure 4.2 ATR-FTIR spectra of um-CNCs, m-CNCs and IEM.

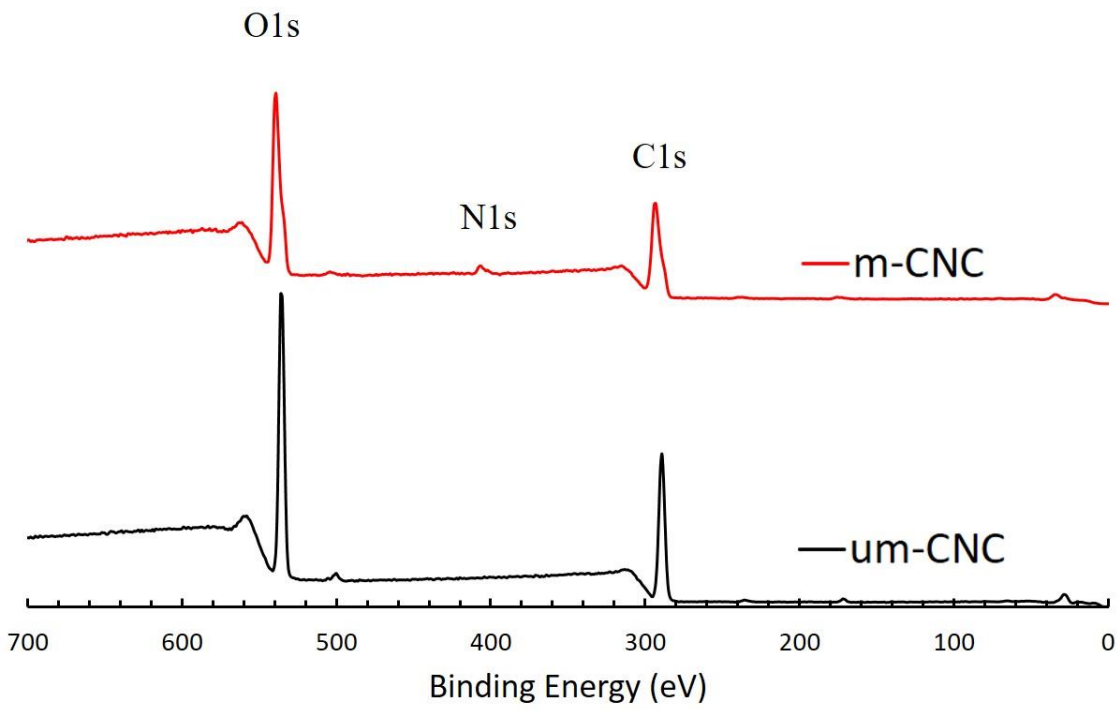

Figure 4.3 XPS wide-scan spectra of um-CNCs and m-CNCs.

Solid state ^{13}C NMR spectra for um-CNCs and m-CNCs were shown in Figure 4.4. The inset in Figure 4.4 showed the corresponding chemical structure of m-CNCs. Both spectra showed the chemical shifts characteristics of the anhydroglucose units (AGU) of cellulose[165], where typical peaks were displayed corresponding to C1 (105.2 ppm), $C4_{cyst}$ (89.2 ppm), $C4_{amorph}$ (83.8 ppm), $C6_{cryst}$ (65.4 ppm) and $C6_{amorph}$ (62.7 ppm). The resonances of C2, C3 and C5 of AGU were located closely between 70 and 80 ppm. After modified with IEM, six new peaks appeared as indicated in the inset, suggesting the attachment of vinyl groups (Ca and Cd at 127.9 ppm and 136.2 ppm), carboxyl groups (Cd at 168.1 ppm) and urethane linkages (Cf at 157.3 ppm). Signals between 10 to 40 ppm are due to the hydrocarbons, specifically the secondary carbon (Cf and Ce at 40.1 and 64.0

ppm) and primary carbon (Cc at 19.8 ppm)[166]. These results further supported the surface modification of CNCs with IEM.

The degree of substitution (DS) was then determined based on NMR spectra. DS is a parameter used to describe the extent of modification as the number of hydroxyl groups that have been modified per AGU, which ranges from 0 to 3.0 (with three hydroxyl groups on each AGU). According to NMR spectra, the content of each carbon atom was represented by the integrated area under the signals. Therefore, the DS can be determined by[167]:

$$DS = \frac{C_{IEM}/N_{IEM}}{C_{AGU}/N_{AGU}} \tag{4-1}$$

where C_{IEM} and C_{AGU} represent the sum of the signal area of all carbon atoms in IEM and AGU, and N_{IEM} and N_{AGU} mean the number of carbon atoms in per IEM and per AGU. Thus, the *DS* of m-CNCs was determined to be 0.14, which is two times higher than the common *DS* for isocyanate modified CNC[168]. Typically, it is more appropriate to consider a surface *DS* since only the surface hydroxyl group of CNCs can participate in the reaction. Eyley et al. provided the equation to calculate the number of hydroxyl groups on the CNC surface in moles per gram, which can be used to convert *DS* to the surface $DS_{surface}$[169]. It is noted that theoretical maximum $DS_{surface}$ is 1.5 due the crystalline structure of CNCs, where one C2, C3, and C6 hydroxyl group point out of the crystal surface for every two AGUs. The $DS_{surface}$ was calculated to be 0.40 according to the dimensions of CNCs used in this work and the crystallographic parameter reported by Wu

et al.[66], which means that 26.7% available hydroxyl groups on CNCs have been converted to acrylic functional groups.

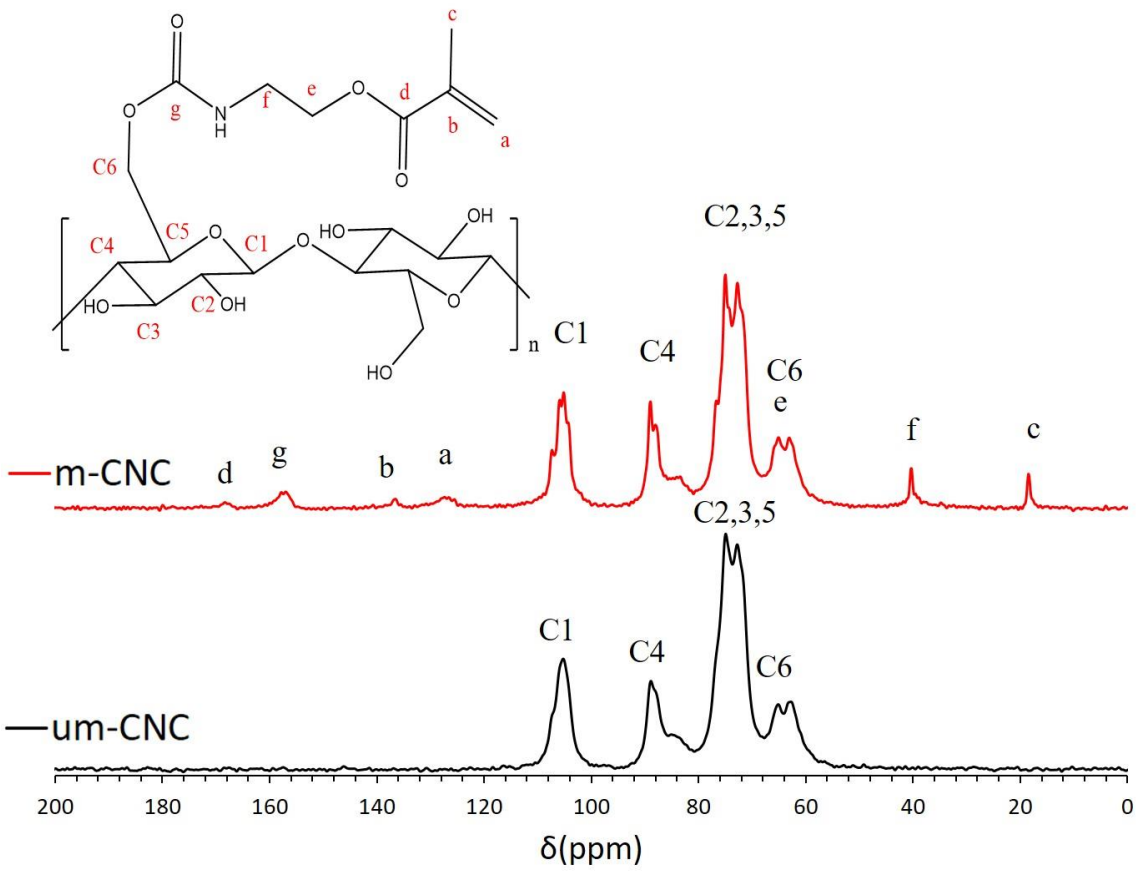

Figure 4.4 13C NMR spectra for um-CNCs and m-CNCs.

Elemental analysis on um-CNCs and m-CNCs further confirmed the modification reaction, and the data were also used to calculate the *DS*. Nitrogen content in um-CNCs is negligible. After the modification, the m-CNCs contained 0.76 wt.% nitrogen, suggesting the attachment of IEM on CNCs. The *DS* can be calculated by following equations:

$$Y = \frac{100M_{IEM} \times DS}{162 + W_S \times DS} = 100 \times (X_N \times \frac{M_{IEM}}{M_N}) \quad (4\text{-}2)$$

where Y is the percent of substituted hydroxyl groups, M_{IEM} is the molecular weight of IEM, M_N is the molecular weight of nitrogen atom, and W_S is the net increase in formula weight from one substituent group per AGU. The resulted DS is 0.10 according to the fDS results between NMR and elemental analysis may raise from the different NMR signal sensitivity for each carbon atoms in the samples.

Table 4.1 Elemental Composition of um-CNCs and m-CNCs

	C	H	N	O
Unmodified CNC (wt.%)	41.1	5.6	<0.05	44.4
Modified CNC (wt. %)	40.5	6.2	0.76	46.8

4.4.2 Crystallinity of um-CNCs and m-CNCs

XRD was used to examine the effect of surface modification on the CNC crystal structure. The um-CNCs showed typical peaks at 22.5 ° and 34.5 °, corresponding to the cellulose I structure[170]. After the modification, the peaks at 34.5 °, 39.2 °, and 47.5 ° showed evident reduction. The crystallinity indexes for um-CNC and m-CNC were calculated according to the method developed by Segal et al.[171] As expected, the crystallinity index decreased from 91.4% for um-CNC to 72.1% after the modification.

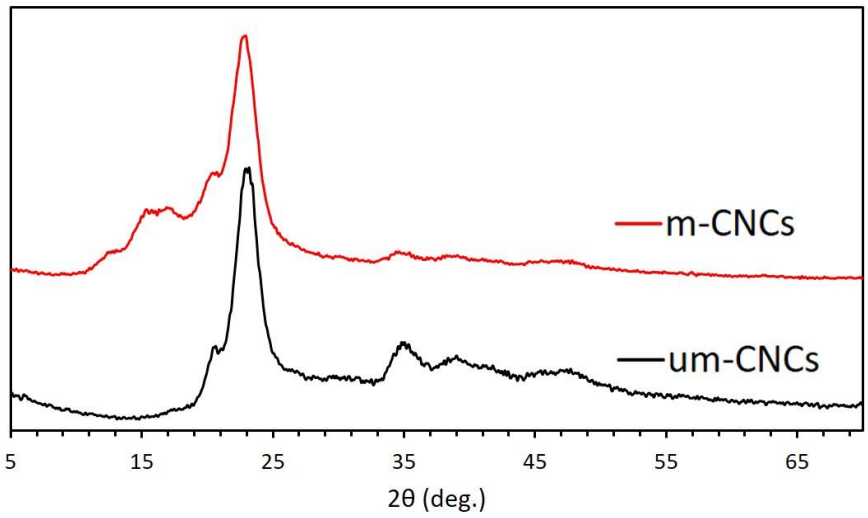

Figure 4.5 XRD spectra of um-CNC and m-CNC.

4.4.3 Thermal stability of um-CNCs and m-CNCs

Thermal stability of unmodified, modified CNCs and washed um-CNC was analysed by thermogravimetric analysis (TGA). The weight loss curves and derivative weight loss curves of the samples were shown in Figure 4.6. First, the sample experienced washing process showed early degradations at around 100 °C, which was attributed to the evaporation of residual toluene. The onset temperature of degradation for three samples is shown in Table 4.2. Unmodified CNCs showed a slightly lower onset temperature than m-CNCs with a difference of 6 °C. However, the washing process reduced the onset temperature of um-CNC from 246 °C to 214 °C. Comparing the washed um-CNC with m-CNC, the results suggested that the modification improve the thermal stability with an enhanced onset temperature from 214 °C to 252 °C.

Table 4.2 The onset temperature of degradation.

	um-CNC	um-CNC	m-CNC
Drying Method	Freeze Dried	Wash and dried	Wash and dried
Onset Temperature ℃	246± 2.3	214 ± 1.2	252 ± 2.1

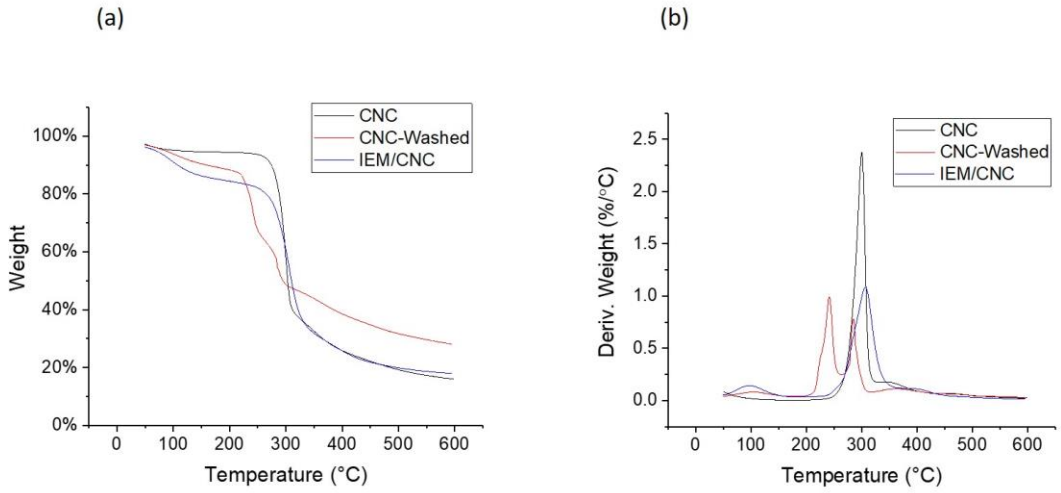

Figure 4.6 (a) Weight loss cures and (b) derivative weight loss curves for um-CNCs, m-CNCs, and washed um-CNCs.

4.4.4 Enhanced hydrophobicity of m-CNCs

Sessile drop water contact angle measurements are used to verify the enhanced hydrophobicity of m-CNCs. Uniform films were prepared with drop coating um-CNC (in water) and m-CNC (in toluene) to piranha-etched silicon wafer. Figure 4.7 shows the water contact angles on um-CNCs was similar to that on silicon wafer, indicating the hydrophilicity of um-CNCs. After the modification with IEM, the water contact angle increased from 27 ° to 62 °. This enhanced hydrophobicity of m-CNCs can be correlated to the better dispersity in DMF as shown in Figure 4.8. The um-CNCs formed a turbid suspension in DMF after 2 h of sonication, while the m-CNCs can form a clear suspension

with only mildly vortex. The highest contact angle of modified CNCs is reported as 94 °, where high density grafting of polystyrene chains was achieved. However, in this work, the grafting agent is only a small bifunctional group.

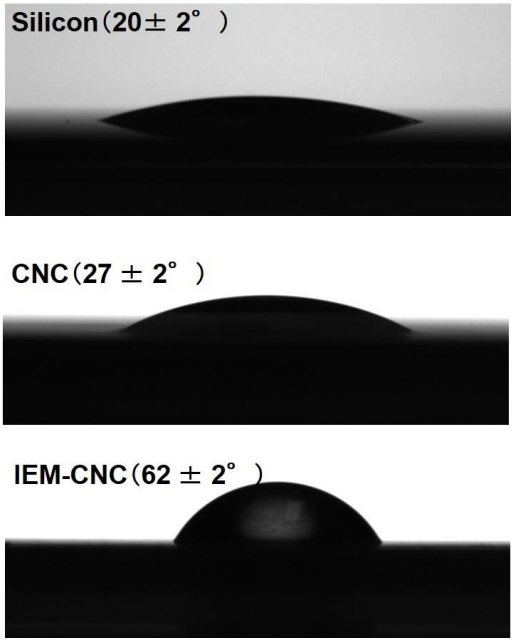

Figure 4.7 Water contact angles for piranha-etched silicon wafer, um-CNCs film and m-CNCs film.

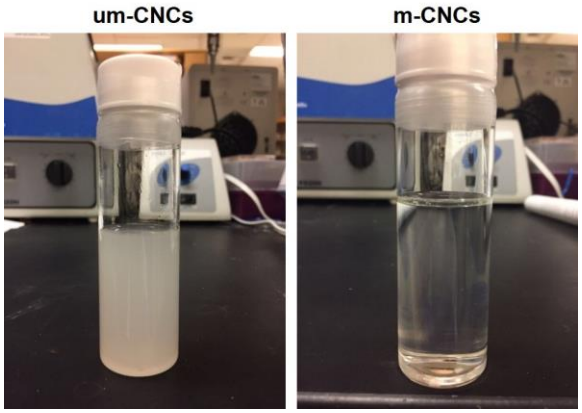

Figure 4.8 A comparison of um-CNC (0.2 g) and m-CNC (0.2 g) dispersed in DMF (~20 g).

4.5 Conclusion

In this chapter, freeze dried CNC was modified with IEM to introduce acrylic functional groups on the surface for potential applications with acrylic polymer. The modification process is optimized to achieve a relatively high density of acryloyl groups on CNCs surface. ATR-FTIR, XPS, solid state ^{13}C NMR and elemental analysis confirmed the attachment of IEM and acrylic groups on CNCs. The presence of vinyl groups was confirmed with NMR spectra. The surface degree of substitution is determined as between 0.28 and 0.40 based on the results of NMR and elemental analysis. XRD showed a slight decrease in the crystallinity index of CNCs from 91.4% to 72.1% after the modification. TGA showed the enhanced thermal stability as an increased onset temperature of degradation from 214 °C to 252 °C. Finally, the enhanced hydrophobicity of m-CNCs was confirmed with sessile water contact angle measurement, where the contact angle increased from 27 ° to 62 °. The resulting m-CNC may serve as reinforcing agents in acrylic polymer matrix with improved dispersity and interfacial adhesion.

CHAPTER 5. MECHANICAL PROPERTIES OF ACRYLIC FUNCTIONALIZED PMMA/CNC COMPOSITES: THE EFFECT OF SURFACE MODIFICATION OF CNC AND OPTIMIZED PREPARATION PROCESS

5.1 Overview

Acrylic polymer is a major class of plastics with a great variety of applications. Polymethylmethacrylate (PMMA) is one of the most important commercial acrylic polymers, which has been used as windows, lenses and other optical devices. However, its application has been limited by the relatively low mechanical properties. In this chapter, acrylic functionalized CNCs were first incorporated into PMMA matrix with the "solution-casting" method to reinforce the mechanical performance. The enhanced dispersity of m-CNCs were verified with polarized light microscopy (PLM) and UV-vis spectrometry. Tensile testing showed the reinforcing effect of m-CNCs. However, the residual DMF issue associated with the "solution-casting" method was identified with the results from ATR-FTIR, DSC and TGA. Two alternative processing methods: the "bulk-pressing" and "solution-pressing" methods were developed and optimized. Although the "bulk-pressing" method increased the molecular weight of PMMA matrix, significantly reduced the residual DMF, and achieved higher tensile strength, the highly energy consuming drying process may neutralize the benefits. Meanwhile, the "solution-pressing" method can effectively remove DMF with a simple precipitation process. It was surprising that the solution-pressing method achieved the highest tensile strength of m-CNCs samples with the lowest molecular weight, compared to the other methods. These results indicated the significant role of the interfacial adhesion in composite materials.

5.2 Introduction

Acrylic polymers represent a major class of commercial plastics and are utilized in a wide range of products and industries. Two of the most significant are the paints and coatings and transparent high-strength plastics for windows (such as Plexiglas® and housewares). For example, acrylic surface coatings are the leading material used in the paint and coatings industry and are utilized in all three major market categories: architectural coatings, OEM product finishes, and special-purpose coatings. For another example, the Europe acrylic sheet market size in 2016 was about $1.41 billion, and increasing demand for infrastructure development as well as residential construction is expected to propel growth in the recent future.

Polymethylmethacrylate (PMMA) is one of the most important commercial acrylic polymers, which has been used as windows, lenses and other optical devices. However, its application has been limited by the relatively low mechanical properties. Many attempts have been made to reinforce its mechanical properties with nano-sized particles[78, 172-174] and micro sized fibers[175, 176]. Meanwhile, cellulose nanocrystals (CNCs) exhibit a great potential of reinforcing polymer matrix with superior properties, such as higher specific strength, low density, renewability and sustainability. More recently, several researches have been reported for using CNCs or modified CNCs as reinforcing materials for PMMA with different preparation method. Liu et al. incorporated CNCs into PMMA matrix through in-situ solution polymerization followed by a solution casting process.[80] Mabrouk et al. prepared nanocomposite film via mini-emulsion polymerization and methyacryloxypropyl triethoxysilane (MPS) was used to functionalize CNCs.[177] Benerjee et al. performed surface treatment on cellulose fibers with methyl methacrylate

(MMA) and performed in-situ suspension polymerization.[70] Sain also used in-situ suspension polymerization method with maleic anhydride treated cellulose micro/nanofibers (CNF).[81] Kedzior et al. combined CNCs with surfactant to stabilize miniemulsion polymerization of PMMA.[178]

In this Chapter, acrylic functionalized CNCs were utilized to reinforce the mechanical performance of PMMA. The modified CNCs (m-CNCs) were in-situ polymerized with PMMA in DMF solution. Two alternative methods were developed to optimize the reinforcing effect of the m-CNCs.

5.3 Experimental methods

5.3.1 Materials

Freeze-dried unmodified CNCs (um-CNCs) were provided by USDA Forest Products Laboratory and used as received. Acrylic functionalized CNCs (or modified CNCs, m-CNCs) were prepared based on the method described in Chapter 4. Methyl methacrylate (MMA) was purchased from Sigma-Aldrich, containing ≤30 ppm 4-methoxyphenol as inhibitor at 99% purity. Inhibitor remover and prepacked column were purchased from Sigma-Aldrich for removing 4-methoxyphenol. Dimethylformamide (DMF, anhydrous, 99.8%), and benzoyl peroxide (BPO, Luperox® A98) were also purchased from Sigma-Aldrich and used as received.

5.3.2 Eliminate toluene from m-CNCs/toluene organogel

Before preparing PMMA/m-CNC composite, the residual toluene was eliminated by rotary evaporation. The m-CNC/toluene mixture with 0.4 g CNC was first dispersed in

DMF (10 g). The m-CNC/toluene/DMF suspension was then evaporated at 60 °C with reduced vacuum in a IKA RV 10 Rotary Evaporator for 15~20 min. The weight of the suspension was tracked and the evaporation was stopped when most of the solvent was gone. The resulted sample is a concentrated m-CNC suspension in DMF, with a clear and transparent looking.

5.3.3 Solution polymerization and solution casting method

PMMA composites were prepared with both um-CNC and m-CNC. Modified CNCs were in-situ polymerized with MMA in DMF to synthesize PMMA/m-CNCs nanocomposites at loadings of 0.5 wt.%, 1 wt.% and 2wt.%. A schematic illustration of the in situ polymerization is shown in Figure 5.1.Modified CNCs were first dispersed in DMF. The suspension was then sonicated for 1 h. MMA was purified by passing through a inhibitor removing column. The purified MMA was added into the mixture and mixed by vortex. The concentration of MMA in DMF was kept as 0.25 g/Ml. The resulted m-CNC/MMA/DMF mixture was divided into two equal parts. A stoichiometric amount of BPO was dissolved in the first part of the mixture. The molar ratio of BPO: MMA was kept as 1:1000 for all samples. The first part was then poured into a 3-neck flask heated with an oil bath. The flask was heated up to 80 °C under mechanical stirring with a Caframo Compact Digital Lab Mixer, and refluxed under flowing nitrogen. After 1 h of the reaction, the second part of the mixture was added dropwise by a separatory funnel within 0.5 h. The reaction continued for 5.5 h. The nanocomposite mixture was then poured into glass Petri dishes. The amount of the mixture was controlled so that the thickness of the resulted film after drying was 0.5 ± 0.1 mm. The glass dishes were covered by aluminum foil with pinholes and placed in a convection oven (BINDER Inc. Germany). The mixture in glass

dishes were dried at 60 °C for 72 h. The films were released from the glass dishes by a blade. The um-CNCs/PMMA sample with the same loadings were also prepared with the same procedure. It is noted that all composite loadings are based on the weight of CNCs only. The procedure for preparing neat PMMA films was identical to the procedure for the composite, except the addition of um-CNCs or m-CNCs.

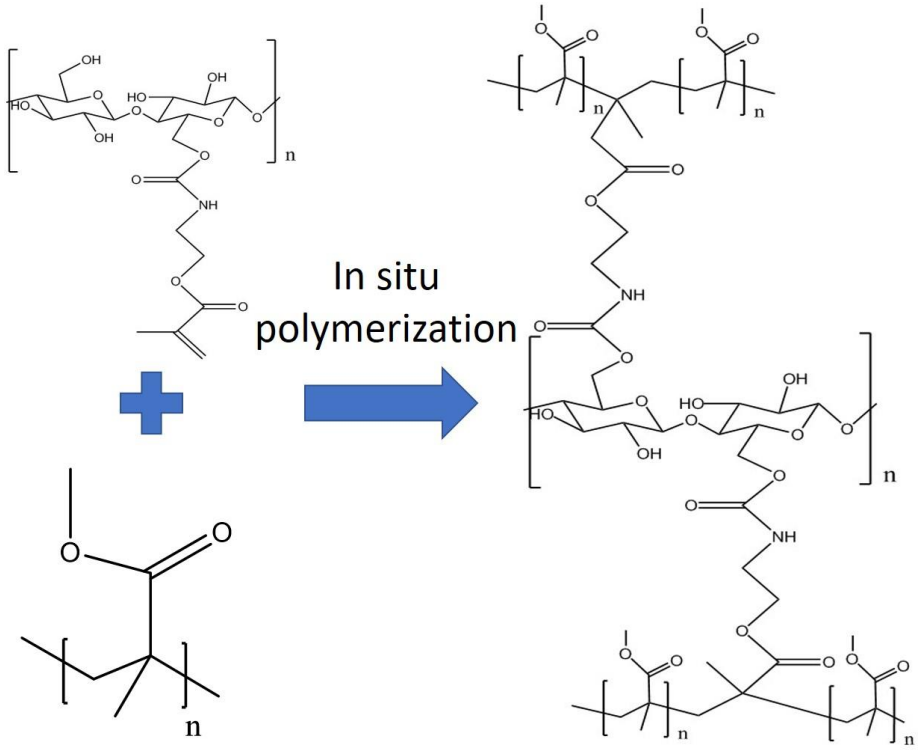

Figure 5.1 A schematic illustration of the in situ polymerization of MMA with m-CNCs.

5.3.4 Bulk polymerization and hot pressing

Bulk polymerization was carried out with a similar way of solution polymerization, instead that only a small amount of DMF was used, where the weight ratio between MMA and DMF was 20:3. To begin with, concentrated m-CNC/DMF suspension was mixed with MMA in a 40-mL glass vial. The mixture was sonicated for 1 h in a 2510 Branson bath

sonicator. Then, BPO was added into the mixture with the same 1:1000 initiator/monomer ratio. After dissolving the BPO in the mixture by mildly vortex (IKA VORTEX 3) and degassing the mixture in the sonicator, the glass vial was sealed and stored in the convection oven at 60 °C for 24 h, followed by 90 °C for one more hour. The resulted bulk neat PMMA, PMMA/um-CNC and PMMA/m-CNC samples were hot pressed down to a film with a thickness around 0.5 mm with a Carver Hydraulic Hot Press system. The film samples were further dried in vacuum at 150 °C for 24 h to eliminate the residual DMF. Samples of the same loadings were prepared for both um-CNC and m-CNC as the solution polymerized samples. For neat PMMA, the samples with and without the same amount of DMF were both prepared as a control.

5.3.5 Solution polymerization and precipitation

A different post processing method was explored with the solution polymerized samples. After the polymerizing reaction was done, the polymer solution was poured into excess DI water with rigorous magnetic stirring, instead of being casted on glass petri dishes. The neat PMMA or PMMA/CNC composites were precipitated and filtered. The solid samples were further washed with DI water for 3 times. The resulted samples were drying in the convection oven at 80 °C for 12 h before hot pressing.

5.3.6 ATR-FTIR

Polymer films were analyzed by ATR-FTIR to characterize their chemical structures. The equipment is a Bruker Vertex 80 V spectrometer with ATR accessory (Bruker Platinum ATR). The wavenumber scan range was from 4000 cm^{-1} to 600 cm^{-1} with a resolution of 4 cm^{-1} and a total of 64 scans. All spectra were normalized at 1730 cm^{-}

^{1} peak, since it is corresponded with the ester groups of acrylates, which were not reactive during the in-situ polymerization[173].

5.3.7 Gel permeation chromatography (GPC)

The molecular weight and polydiversity (PDI) of PMMA and PMMA composites were measured using a Shimadzu gel permeation chromatography setup (GPC equipped with a RID-10A refractive index detector, LC-20A chromatograph pump, and CTO-20A column oven). DMF was used as the eluent at an operating temperature of 35 °C and a flow rate of 1 mL/min. Two 5 mm phenogel 10 E4A columns (molecular weight range: 200 to 2×10^{6} g/mol) were calibrated using linear polystyrene (PS) standards.

5.3.8 Differential scanning calorimetry (DSC)

The glass transition temperature (T_g) of all samples were measured by DSC (TA Instruments DSC Q200). As a first step, samples were annealed in the instrument at 160 °C or 200 °C and then cooled to 0°C at a rate of 20°C/min. The samples were subsequently heated to 160°C at a rate of 10°C/min. This last heating step was used to obtain T_g of the sample. The value of T_g was assigned as the midpoint of the transition region of the heat flow curve using the instrument analysis software. Three tests were performed for each sample and the average value was reported.

5.3.9 TGA

The amount of residual DMF and thermal stability of the composite samples were assessed with thermogravimetric analysis (TGA; TA Instruments TGA Q5000). Samples

were first heated from 25 °C to 150 °C at a rate of 5 °C/min, then held at 150 °C for 30min, and further heated to 600 °C under a flowing nitrogen atmosphere.

5.3.10 Polarized light microscopy (PLM)

CNC dispersion in PMMA matrix was investigated qualitatively with an optical microscope (Olympus BX51) equipped with two polarizers (Olympus U-AN360P). Large CNC aggregates will be observed as birefringence due the crystallinity[71]. Images were captured with an Olympus camera (U-CMAD3) AND processed with PictureFrame software. All images were taken in a transmission mode with a 20X objectives and at full extinction of the polarizer.

5.3.11 UV-vis spectroscopy

The light transmission of neat PMMA and composites were assessed by UV-vis spectroscopy with a SHIMADZU UV-1800 spectrophotometer. The UV-vis absorption of samples was obtained and converted to the light transmission. The transmission was normalized with a film thickness of 0.6 mm according to the Beer-Lambert law. The light transmission at 550 nm wavelength was compared among different um-CNC and m-CNC loadings.

5.3.12 Tensile testing

The tensile strength of all samples was investigated with uniaxial tensile testing on a Instron 5842 Universal testing machine. The samples were prepared by cutting the films with a dog bone die based on the ASTM D1708-13. The test section was approximately 22 mm long, 4.93 mm wide and 0.6 mm thick. The testing speed was set as 1mm/min. The

average tensile strength, elastic modulus, elongation at break were reported based on at least four specimens for each composition.

5.3.13 Scanning electron microscopy (SEM)

Both tensile fracture surface and cryofracture surface were examined with a Zeiss Ultra-60 FE-SEM to reveal the surface morphology and fracture mechanisms. Fractured composite films were mounted on sample holders, where the fracture surface is facing upward. Then, samples were sputter-coated with Au/Pd in a Hummer sputtering system to prevent charge build-up during measurement. All images were obtained under an accelerating voltage of 5.0 kV.

5.4 Results and discussion

5.4.1 Solution-casting method

5.4.1.1 Chemistry of PMMA/m-CNC Composites

The chemical structure of the polymer composites was also characterized with ATR-FTIR, shown in Figure 3. For all CNC loadings tested here, the absorption at 1723 cm^{-1} represented the acrylate carboxyl group. The distinct absorption bands from 1150 cm^{-1} to 1250 cm^{-1} corresponded to the C-O-C stretching vibration. The band at 1444 cm^{-1} can be assigned to the bending vibration of the C-H bonds of the $–CH_3$ group. The two bands at 2997 cm^{-1} and 2952 cm^{-1} can be attributed to the C-H bond stretching vibrations of the $–CH_3$ and $–CH_2$ groups, respectively. It was noted that the weak absorption at 1680 cm^{-1} indicated the residual DMF in the sample. However, no new peaks were observed with ATR-FTIR due to the addition of CNCs.

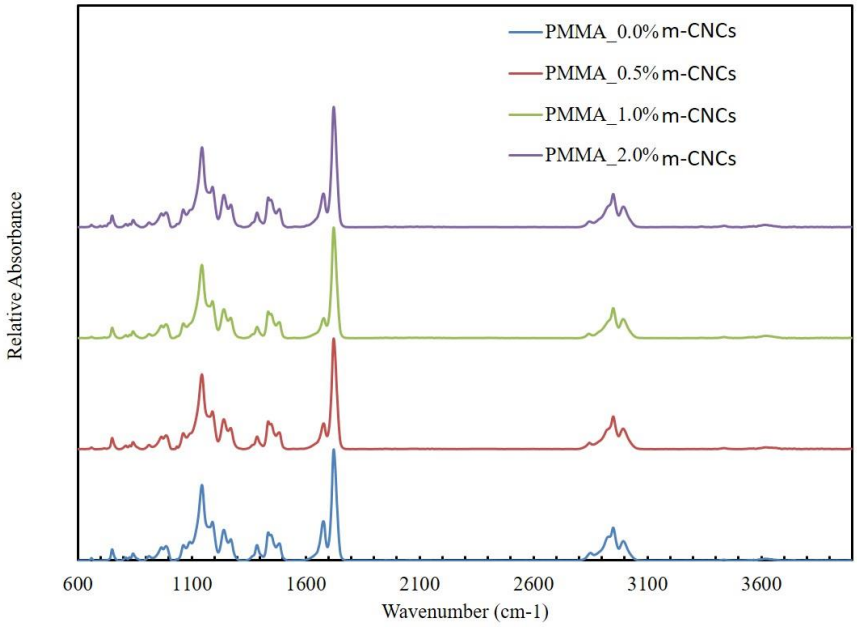

Figure 5.2 ATR-FTIR spectra of neat PMMA and PMMA composites with m-CNC, at CNC loadings of 0, 0.5, 1.0 and 2.0 wt.%.

The molecular weight and PDI of the in-situ polymerization product were measured with gel permeation chromatography, as shown in Figure 5.3. The results were summarized in

Table 5.1. For the m-CNC composite, two peaks were detected at the retention times of 8 min and 12.5 min, respectively. The second peak was identified as free PMMA chains according to the result of neat PMMA. Given the specific reaction condition described above, the number-averaged molecular weight (M_n) ranges from 60 kDa to 70 kDa. The composite sample showed lower molecular weight, indicating the exist of um-CNCs or m-CNCs may hinder the length of free PMMA chains, considering that MMA monomer also reacted with m-CNC. However, the M_n of 1.0% m-CNCs composite is much lower than the others. Some factors like oxygen exposure, reaction time or initiator content may affect the final M_n. More interestingly, an additional peak at around 8 min was detected

with all m-CNCs composites, while the neat PMMA and um-CNCs composites didn't show this peak. This early peak indicated an extremely large M_n, which was not reasonable for PMMA chains. Moreover, the area percentage of the first peak increased with the increasing m-CNC loading. The results suggested that the first peak may associated with the nanoscale m-CNCs and/or PMMA grafted m-CNCs, which can pass through the membrane filter for sample purification. The unmodified CNCs were filtered out with 0.45 μm pore size of the filter. Thus, this peak was not shown in PMMA/um-CNC samples. The results also indicated that the surface modification enhanced the dispersity of CNCs and achieved nanoscale particle dispersion. It was worth noting that the M_n results may be a little different from the real value since the GPC is calibrated with a linear polystyrene standard, while PMMA chains may have branches and different configurations.

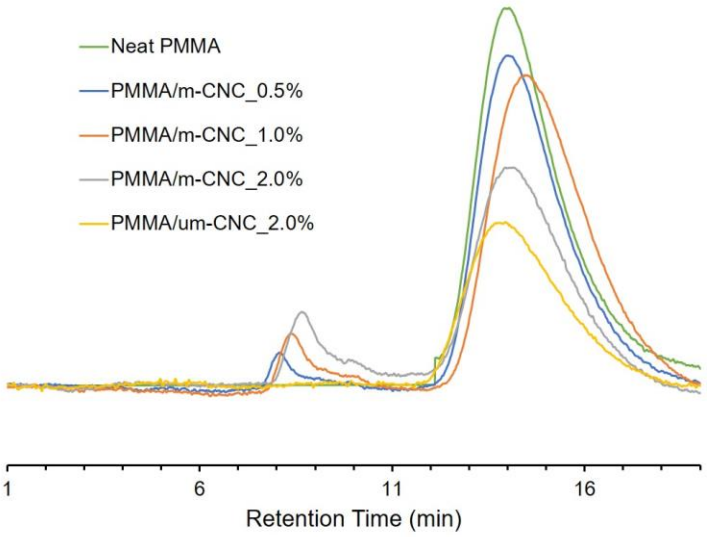

Figure 5.3 GPC curves of PMMA/m-CNC at loadings of 0.5, 1.0 and 2.0%, and PMMA/um-CNC at 2.0% loading.

Table 5.1 The molecular weight of PMMA composite with 0.5, 1.0, 2.0% m-CNC, and 2.0% um-CNC.

	Peak	Mn	Area Percentage %
Neat PMMA	a	0	0
	b	70422	100
0.5% m-CNC_PMMA	a	377073810	3.3
	b	60697	96.7
1.0% m-CNC_PMMA	a	103014856	6.6
	b	46908	93.4
2.0% m-CNC_PMMA	a	89864458	11.0
	b	63239	89.0
2.0% um-CNC_PMMA	a	0	0.0
	b	66725	100.0

5.4.1.2 Dispersion of CNCs in PMMA matrix with solution polymerization

PLM is a useful tool for analyzing CNC dispersions in transparent/amorphous matrix[150]. The crystalline nature of CNCs can give rise to obvious birefringence when viewed under polarized light due to their optical anisotropy. Conversely, if the PLM images showed non-

birefringence, it can be concluded that the CNCs are well dispersed at this length scale. PLM also enables the assessment of dispersion in large scale, compared with electron microscopy techniques. Both bright field (normal) and dark field (PLM) images of um-CNC and m-CNC composite are shown in Figure 5.4a. Modified CNC composite at all loadings showed completely dark images, which suggesting an amorphous materials and well dispersed m-CNC. While the um-CNC composite with 2.0% CNC loading showed birefringent regions across the whole observed area. This result indicated that um-CNC tends to aggregate in PMMA matrix, and m-CNC were likely dispersed more homogeneously with enhanced compatibility with PMMA matrix. Moreover, the reactivity of acrylic groups on m-CNCs surface can also facilitate the dispersion during the in-situ polymerization process. In addition to microscopic images, the bulk composite materials also showed a great contrast in light transmission. Figure 5.4b highlighted the optical properties of neat PMMA, 2.0% m-CNC and 2.0% um-CNC composites. The m-CNC composite samples showed similar transparency with neat PMMA, while the um-CNC composite showed hazy looking with a white color of um-CNC powders. The light transmission of neat PMMA and composite samples were quantitatively assessed by using UV-vis spectroscopy as shown in Figure 5.5. At 550 nm wavelength, the light transmission of 0.5, and 1.0 % m-CNC composite remained 100%. It came to 92.3% when the m-CNC loading was further increased to 2.0%. In contrast, the um-CNC composite showed reduced light transmission as 92.1%, 77.1% and 85.5% for 0.5, 1.0 and 2.0% loadings. Combining the results form PLM and UV-vis spectroscopy, it was concluded that the modified CNCs were well dispersed in PMMA matrix with in-situ solution polymerization.

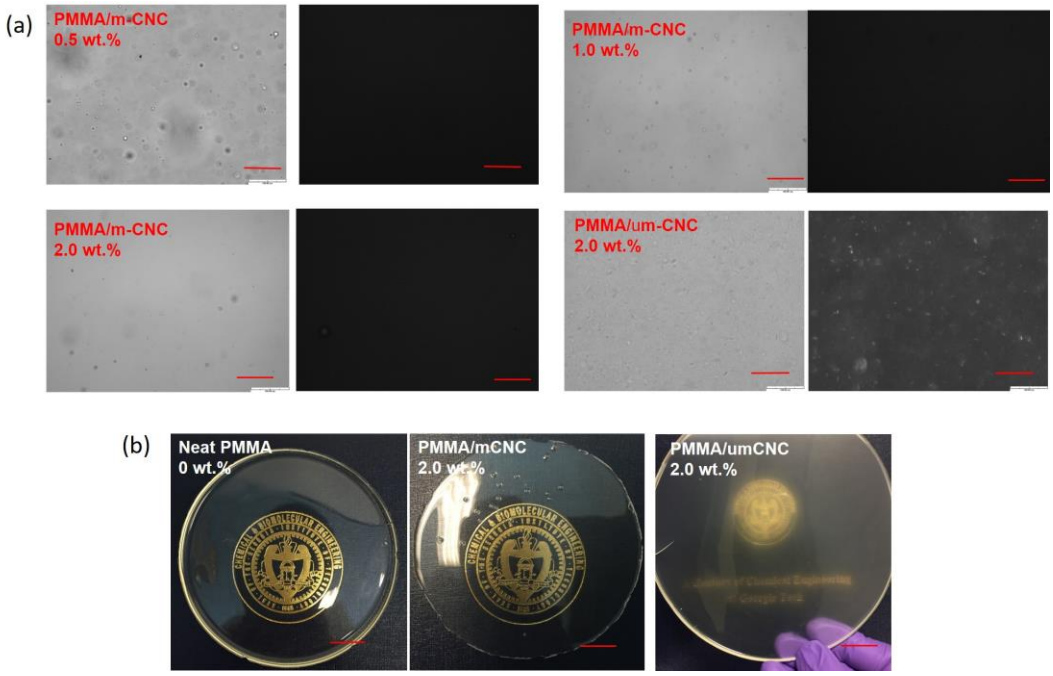

Figure 5.4 (a) PLM images of PMMA/m-CNC with 0.5, 1.0, and 2.0 wt.% CNC loading, and PMMA/um-CNC with 2.0% CNC loading, scale bars are 100 µm (b) Photographs of neat PMMA, PMMA/m-CNC_2.0%, and PMMA/um-CNC_2.0% composites, scale bar: 2 cm.

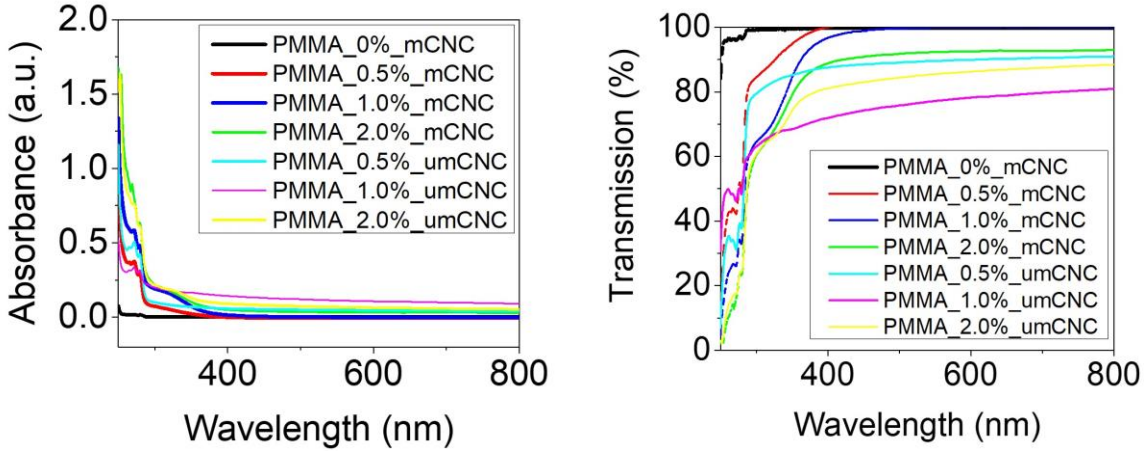

Figure 5.5 UV-vis light absorbance (left) and transmission (right) of PMMA composites.

5.4.1.3 Mechanical and thermal properties of PMMA/CNC Composites.

The mechanical performance of the composites and neat PMMA was assessed with uniaxial tensile testing as shown in Figure 5.6. In general, m-CNCs showed better performance than um-CNCs in terms of the reinforcing effect. For the tensile strength, both um-CNC and m-CNC composite improved the tensile strength at 0.5 and 1.0% loadings, while the samples containing m-CNCs performed better than samples loaded with um-CNC. For example, at 1.0% CNC loading, PMMA/m-CNC exhibited a tensile strength of 26.2 MPa, which is 17.5% higher than that of PMMA/um-CNC composites, and 63.8% higher than that of neat PMMA. When the CNC loading further increased to 2.0%, um-CNC composite showed significant reduction in tensile strength as 13.4 MPa, which is even lower than that of neat PMMA. In the contrast, m-CNC composite maintained a 54.4 % increase of tensile strength compared to neat PMMA. Although the ASTM 1708 standard is not capable to give quantitative elastic modulus results, the elastic modulus was calculated based on the initial slope of the stress-strain curves as shown in Figure 5.6b. Although, it was expected that the incorporation of highly rigid CNCs can stiffen the PMMA matrix, the m-CNCs still showed better stiffening effect than um-CNCs. It was worth noting that 0.5% m-CNC showed better reinforcing performance than 1.0% um-CNC. Therefore, less m-CNC is needed to achieve equivalent or even better performance than um-CNCs. In addition, m-CNCs composite beard longer elongation before break than um-CNC composite, even though the composites samples all have less elongations at break. Assuming the particle size and particle loading are similar at given concentration of m-CNC or um-CNC, these results implied that the increase in tensile strength is due to a better particle-matrix adhesion[9], which is improved by achieving covalent bonding with modified CNC surface chemistry.

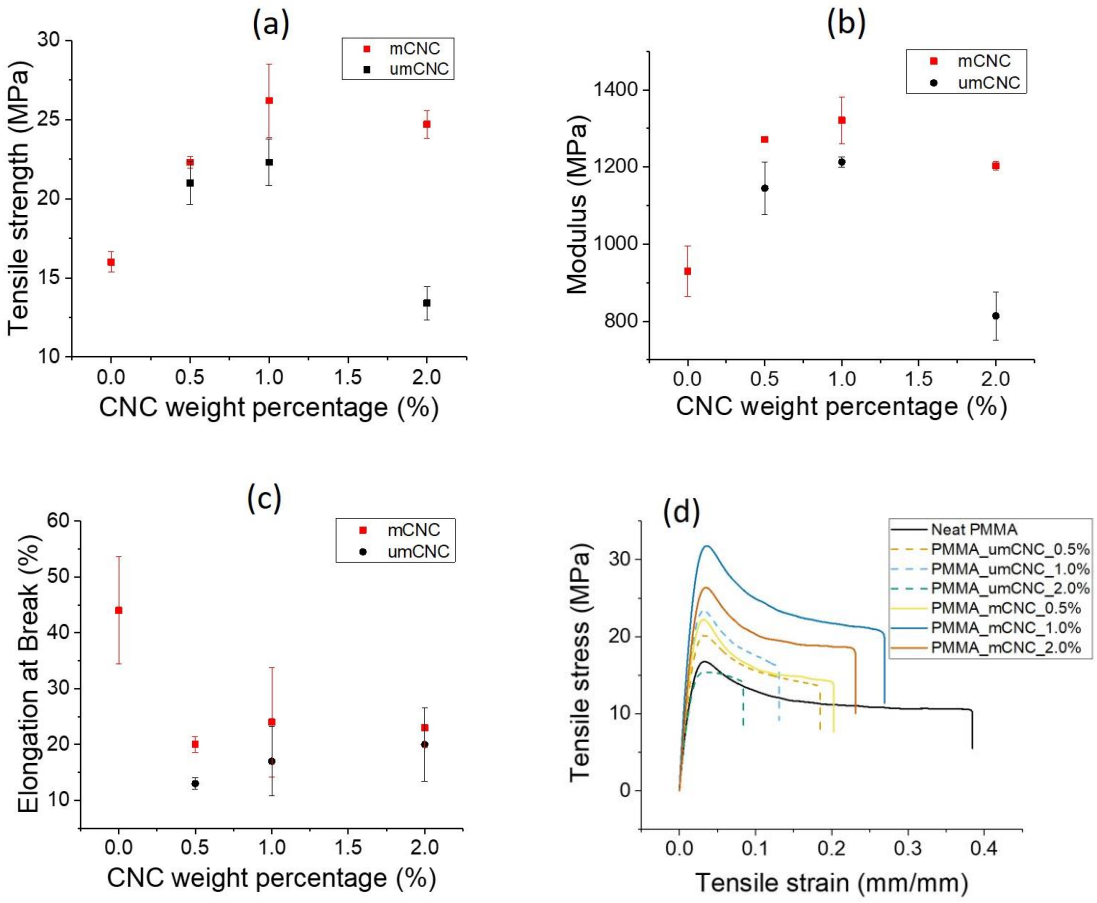

Figure 5.6 (a) Tensile strength, (b) Elastic modulus, (c) Elongation at break of um- and m-CNC composite and neat PMMA and (d) representative tress-strain curves of all solution-casting samples.

Nevertheless, it was noted that the tensile strength range of all samples were sitting at the lower bound of commercial PMMA materials, which is between 25 MPa and 70 MPa dependent on molecular weight and/or configuration[70, 77, 179, 180]. Moreover, the maximum elongation that the glassy PMMA can withstand without failure is 30%, which is even lower than that of the neat PMMA in this work. Coupling with the results of ATR-FTIR, it was believed that the residual DMF in PMMA matrix resulted in the lower tensile strength and higher elongation at break than common bulk PMMA materials.

DSC characterization was performed to analyze the glass transition temperature of the composite material, as well as to verify the effect of residual DMF. The DSC tests were first performed on neat PMMA and um-CNC composite in between 20 °C and 160 °C. The results are summarized in Table 5.2. Neat PMMA had glass transition temperature at 70.48^{o}C, while the composites had decreasing T_g along with increasing um-CNC loading. The shift of T_g to a lower temperature suggested an increase of the mobility of polymer chains. It was believed that the presence of um-CNC can induce the mobility of polymer chains by forming hydrogen bonds at the interface[80]. However, all T_g were also lower than the common PMMA materials with the similar molecular weight. It was hypothesized that the lower T_g may be also due to the residual DMF, which can improve PMMA chain mobility. To verify the hypothesis, a wider heating range (20^{o}C to 200^{o}C) was adopted to eliminate the residual DMF. Firstly, a significant endothermal peak appeared at around 150^{o}C during the first heating run. The endothermal peak can be corresponded with the evaporation of residual DMF, which has a boiling point between 152^{o}C and 154^{o}C. Then, the glass transition temperature was measured from the second heating run as shown in Table 5.3. The glass transition temperature measured with the wider heating range fell in between 100 ^{o}C and 120 ^{o}C, which is consistent with the literature values. The shift to lower T_g was still observed with increasing um-CNC or m-CNC loading, which could result from the short PMMA chains on the m-CNC surface.

Combined with the results of FTIR, DSC and tensile testing, it was clear that DMF was not eliminated during the drying process after solution casting. DMF was locked within bulk PMMA matrix and compromised the mechanical and thermal properties of PMMA composites. Alternative preparation were explored and discussed as following.

Table 5.2 Tg of neat PMMA and um-CNC composite, the heating range is from 20ºC to 160ºC

CNC [%]	T_g [ºC]
0	70.48
0.5	70.25
1	68.31
2	64.36

Table 5.3 Tg of neat PMMA, um-CNC and m-CNC composite, the heating range is from 20 ºC to 200 ºC

CNC loading	um-CNC Tg	m-CNC Tg
Neat	111.88 ± 4.40	
0.5%	116.46 ± 2.09	116.40 ± 0.30
1.0%	106.85 ± 6.78	104.63 ± 5.11
2.0%	102.92 ± 2.43	104.84 ± 1.48

5.4.2 Bulk-pressing method

An alternative way to avoid residual DMF is in-situ bulk polymerization. The advantages of bulk polymerization make it a primary manufacturing method for PMMA sheets, including simple system, pure product, and especially high optical clarity. However, it also leads to a broad molecular weight distribution due to the high viscosity and lack of good molecule diffusion and heat transfer. Nevertheless, although m-CNCs were granted acrylic groups on surface and showed improved hydrophobicity, it was still difficult to achieve as good dispersion in MMA as in DMF. Thus, the reduced amount of DMF (15wt.%) was used with bulk polymerization to improve the dispersion of m-CNC.

GPC results showed that bulk polymerized samples had significantly higher number averaged molecular weights than the solution polymerized samples. For example, bulk polymerized neat PMMA (without DMF) had a M_n as 172 kDa, with a PDI as 1.87. Bulk polymerized PMMA/m-CNC composite with 0.5% loaded CNC and 15 wt.% DMF (Bulk_PMMA/m-CNC_0.5%) presented *Mn* as 122 kDa. Compared with the neat PMMA prepared without DMF, the lower M_n of Bulk_PMMA/m-CNC_0.5% and solution polymerized sample resulted from the chain transfer effect to the solvent (DMF).

Tensile testing was performed with the bulk polymerized neat PMMA and PMMA/m-CNC composites before and after the vacuum drying process. Figure 5.7 presented the tensile strength for all bulk polymerized samples with reduced amount of DMF. The blue columns represent the samples before vacuum drying, while the orange columns represent the post-dried samples. First, comparing the blue columns with the orange columns, the tensile strength increased significantly after the vacuum drying process for all samples. Secondly, the bulk polymerized samples showed higher tensile strength than the solution polymerized ones, mainly due to the improved molecular weight. For example, the pre-dried neat PMMA had a tensile strength as 34.6 MPa, which is 116% higher than the solution polymerized counterpart. It was noted that the pre-dried 2.0% m-CNC loaded samples had a much lower tensile strength than 0.5 and 1.0%. This is because that twice amount (30 wt.%) of DMF was needed during the bulk polymerization to provide sufficient dispersion of 2.0% m-CNC loading. As for post-dried samples, a continuous improvement in tensile strength was observed. The highest tensile strength was achieved at 1.0% m-CNC loading with a 15% increase (from 43.1 MPa to 49.62 MPa) compared to the neat samples.

Unmodified CNCs were also incorporated in PMMA with the bulk-pressing method. However, um-CNCs cannot be homogenously dispersed in MMA even with 15% or 30% DMF, due to the incompatibility between hydrophilic CNCs and hydrophobic MMA. The um-CNC precipitated at the bottom of the glass vials after 2 h of sonication as shown in Figure 5.8a. The resulted bulk samples also presented a heterogeneous distribution and severe aggregation of um-CNCs.

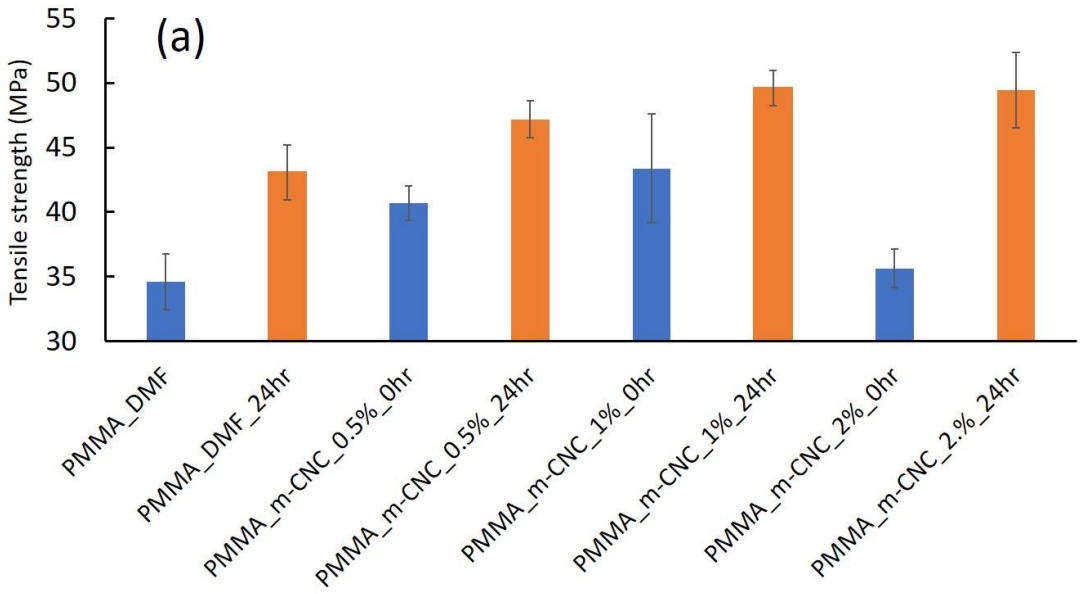
(a)
Tensile strength (MPa)
55
50
45
40
35
30
PMMA_DMF
PMMA_DMF_24hr
PMMA_m-CNC_0.5%_0hr
PMMA_m-CNC_0.5%_24hr
PMMA_m-CNC_1%_0hr
PMMA_m-CNC_1%_24hr
PMMA_m-CNC_2%_0hr
PMMA_m-CNC_2.%_24hr

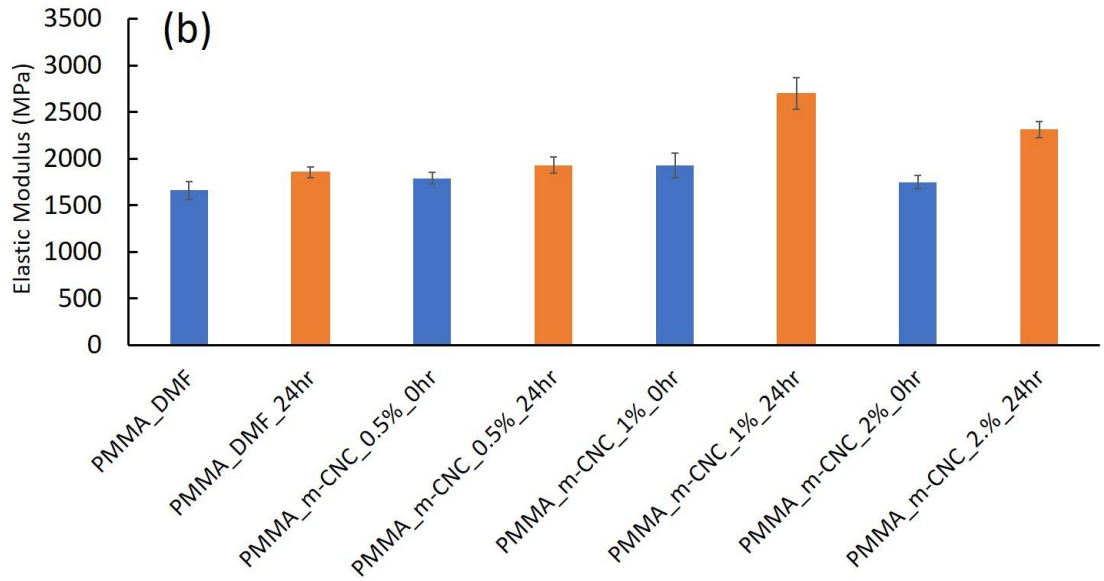
(b)
Elastic Modulus (MPa)
3500
3000
2500
2000
1500
1000
500
0
PMMA_DMF
PMMA_DMF_24hr
PMMA_m-CNC_0.5%_0hr
PMMA_m-CNC_0.5%_24hr
PMMA_m-CNC_1%_0hr
PMMA_m-CNC_1%_24hr
PMMA_m-CNC_2%_0hr
PMMA_m-CNC_2.%_24hr

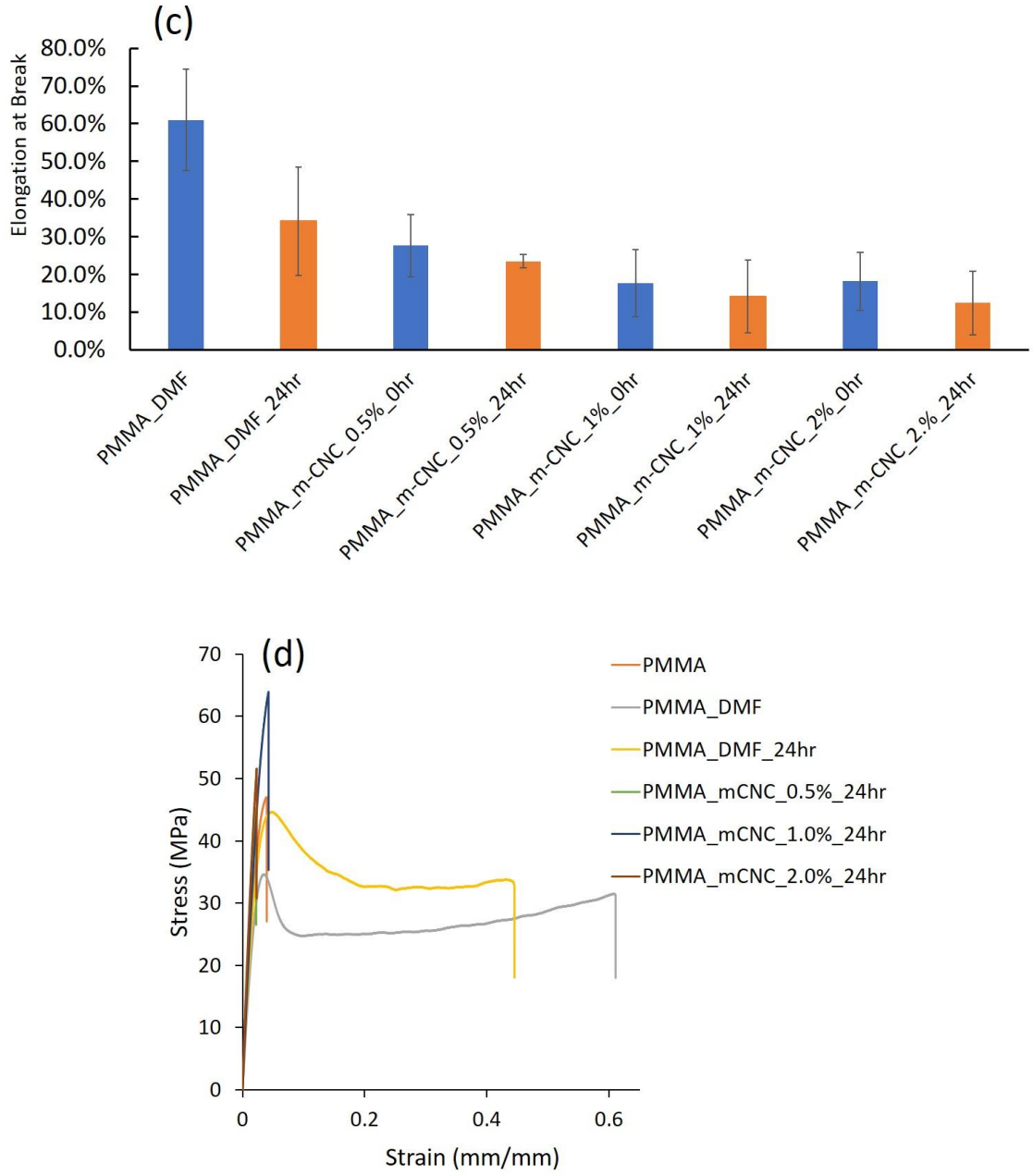

Figure 5.7 (a)The tensile strength, (b) elongation at break, and (c) elastic modulus of neat PMMA and m-CNC composite before and after vacuum drying. and (d) representative tress-strain curves of all bulk-pressing samples.

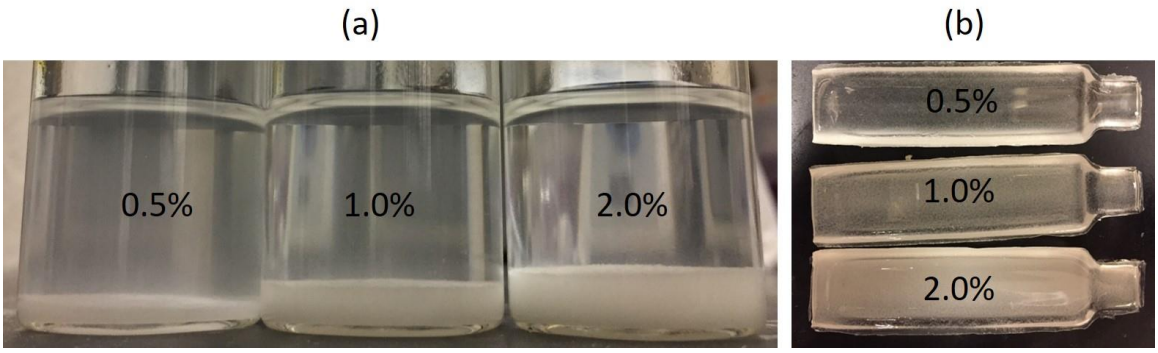

Figure 5.8 (a) Unmodified CNCs dispersed in MMA at loadings of 0.5, 1.0 and 2.0%. (b) PMMA/um-CNC composites prepared by bulk polymerization from MMA/um-CNC suspension.

TGA results further confirmed the effect of vacuum drying process and the residual DMF.

Figure 5.9 The weight loss curve of neat PMMA (bulk polymerized without DMF), and PMMA/m-CNC composite at 0.5% loading (prepared with 15 wt.% DMF) before and after 24 h vacuum drying at 150 °C.

compared the weight loss curves of three bulk polymerized samples, including neat PMMA (prepared without DMF), pre- and post-dried PMMA/m-CNC composite (0.5% loading). Neat PMMA sample showed 1.220% weight loss during the 30-min isothermal at 150°C, which is primarily the moisture loss. In contrast, the pre-dried m-CNC composites lost 14.290% weight during the isothermal. This significant weight loss is associated with the evaporation of DMF, which is supported by the amount of pre-added DMF (15 wt.%). After vacuum drying for 24 h, the post-dried composites samples had a weight loss of 1.688%, which is close to but slightly higher than that of neat PMMA samples.

TGA results combined with GPC and tensile testing supported the conclusion that the bulk-pressing method effectively removed the amount of residual DMF by reducing

the used amount of DMF and vacuum drying at high temperature. However, the economic and environmental benefits of the reduced DMF usage might be neutralized by the energy consumption.

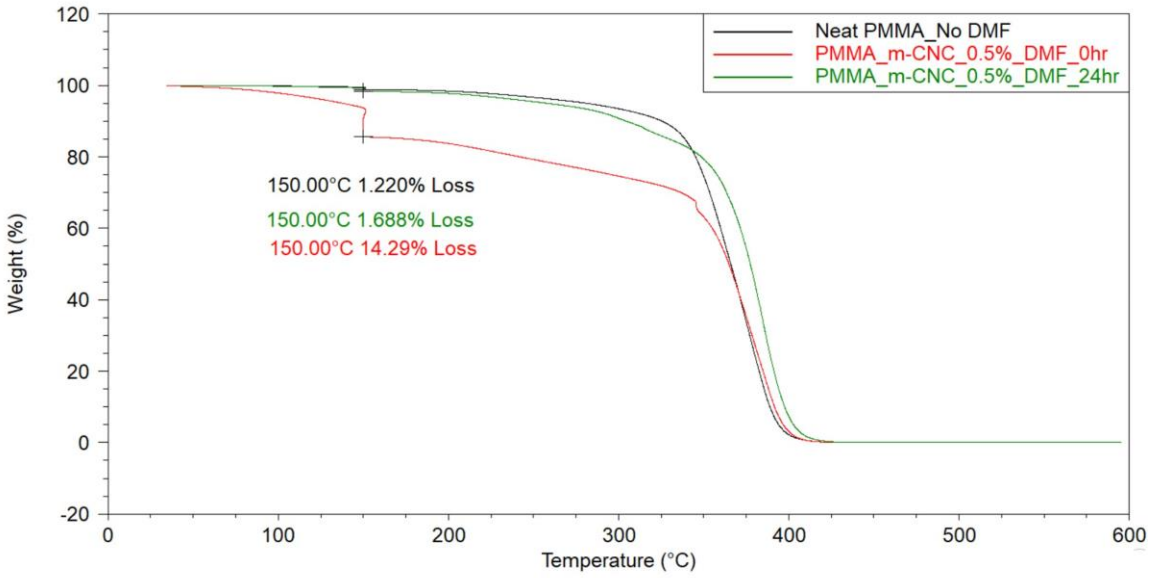

Figure 5.9 The weight loss curve of neat PMMA (bulk polymerized without DMF), and PMMA/m-CNC composite at 0.5% loading (prepared with 15 wt.% DMF) before and after 24 h vacuum drying at 150 °C.

5.4.3 Solution-pressing method

5.4.3.1 Mechanical properties

Although the post drying process has proved significant reduction of DMF and enhanced tensile strength, it is still a low efficiency method considering the low diffusivity of DMF in solid state PMMA matrix[181]. It will be more effective to remove DMF at early stage when PMMA has not been converted to bulk materials. Therefore, the solution-pressing method was used to precipitate PMMA composites in DI water, followed by hot pressing flake and powder form composites to film. Figure 5.10 showed the composite

flakes after precipitation and washing processes. The resulted flakes were then dried at 80°C for 12 h before hot pressing.

The tensile strength of solution-pressing sample was shown in Figure 5.11. All samples have a consistent M_n between 40 kDa and 44 kDa. For m-CNCs samples, the largest tensile strength was achieved by 2.0% loading samples as 53.7 MPa, which is 87.3% higher than the neat PMMA. The um-CNC samples showed lower reinforcing effect at 0.5% loading. When the um-CNC loading was further increased to 2.0%, the composites became too brittle to be cut into a tensile testing specimen as shown in Figure 5.11. In fact, it was also difficult to prepare specimens with the 0.5% um-CNC loading samples, and about 50% attempts were failed. The brittleness of um-CNC composites and the excellent reinforcing effect of m-CNC composite were attributed to the enhanced interfacial adhesion by the surface modification in Chapter 4. However, it was worth noting that the solution-casting method didn't cause this brittleness issue on um-CNC composites samples, where DMF plasticized the PMMA matrix and the samples showed a relatively high elongation at break around 20%. While the solution-pressing method give elongation at break between 15% and 5% as shown in Figure 5.11(b). Therefore, the high tensile strength of m-CNCs composites and the brittleness of um-CNCs composites demonstrated that DMF was effectively removed with this solution-pressing method. In addition, it was impressive that the solution-pressing method achieved higher tensile strength with even lower molecular weight, compared to the solution-casting method and the bulk-pressing method. Finally, the removed DMF can be recycled from water to create more economic and environmental benefits.

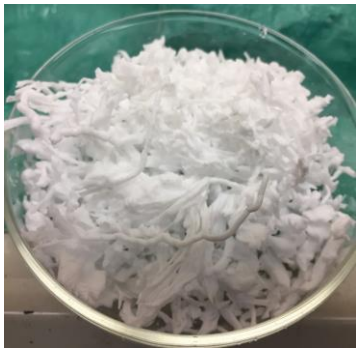

Figure 5.10 Flakes of PMMA/m-CNC (0.5%) composite precipitated in water.

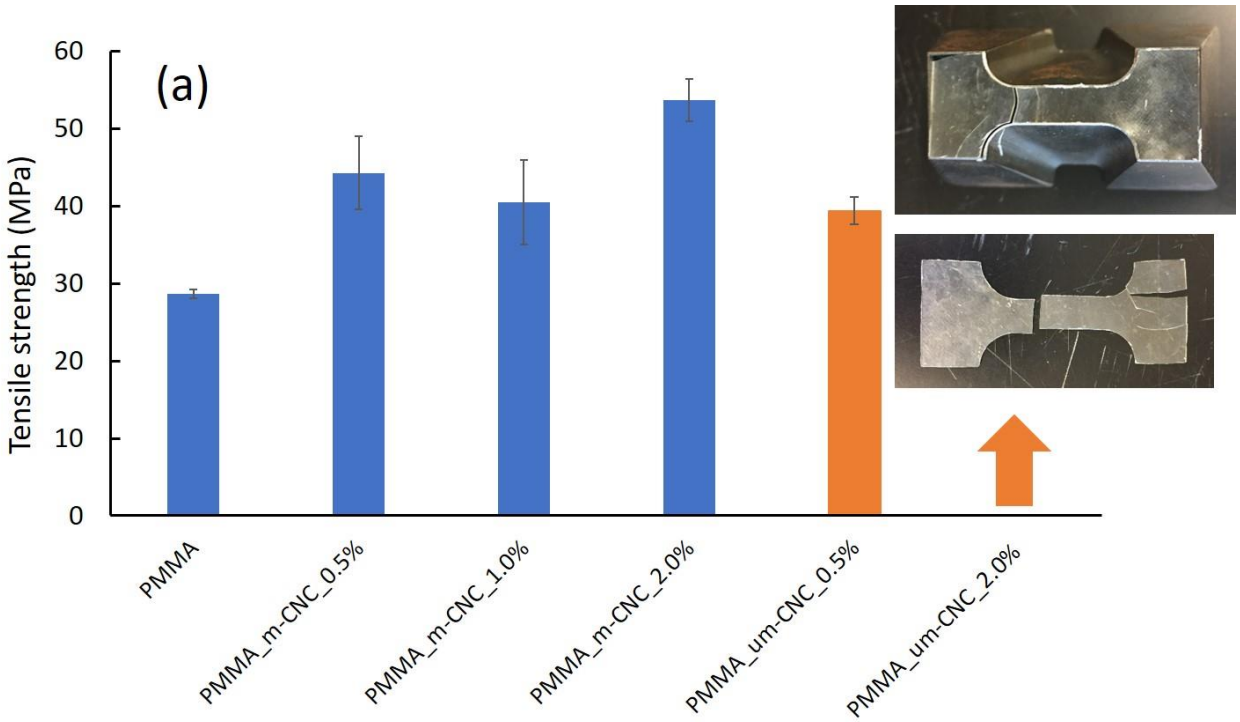

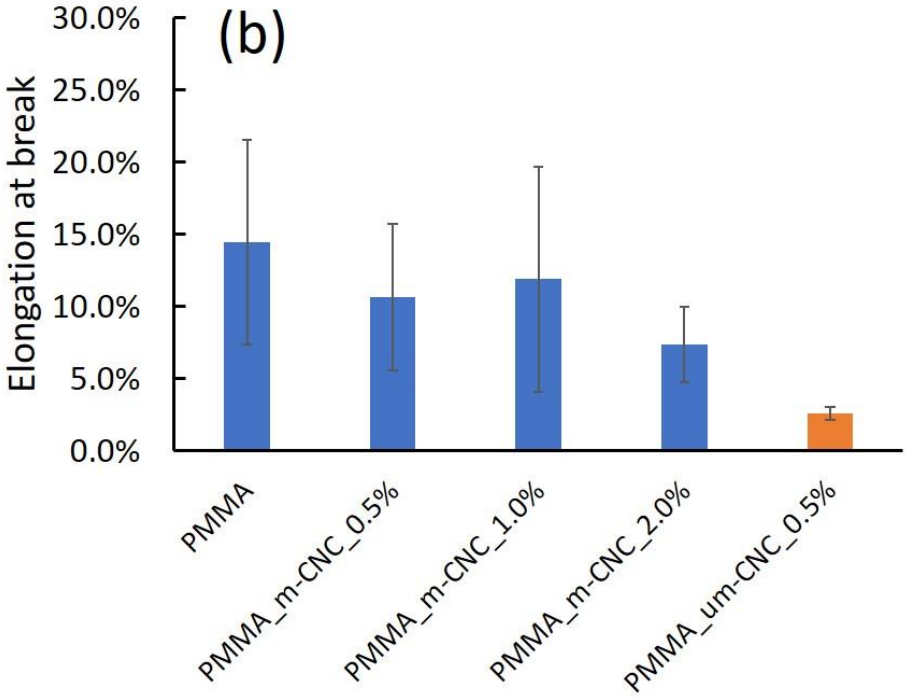
(b)
Elongation at break
30.0%
25.0%
20.0%
15.0%
10.0%
5.0%
0.0%
PMMA
PMMA_m-CNC_0.5%
PMMA_m-CNC_1.0%
PMMA_m-CNC_2.0%
PMMA_um-CNC_0.5%

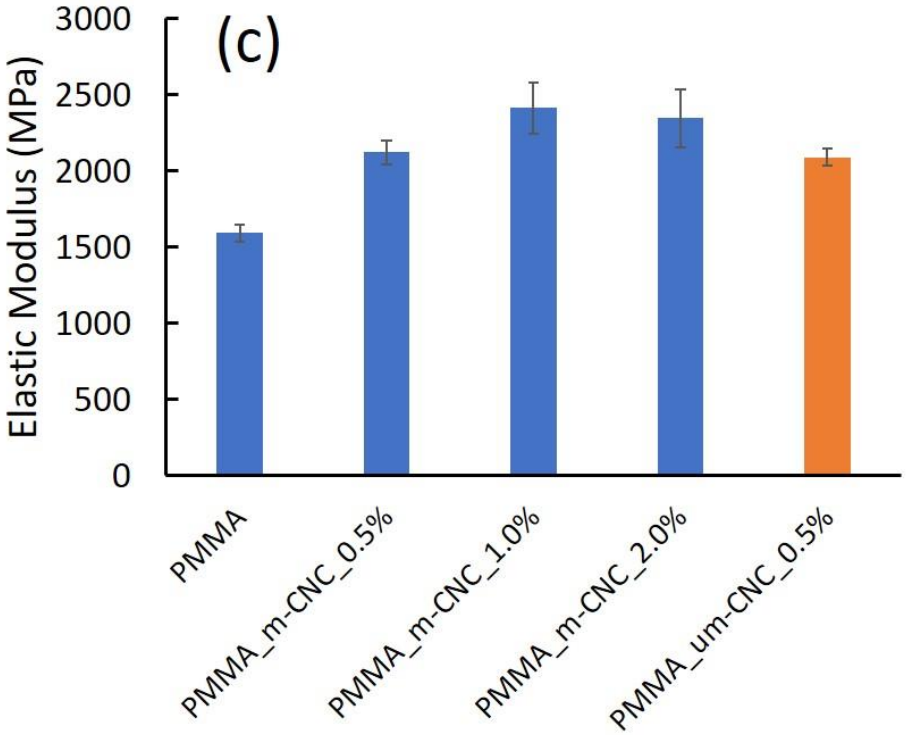
(c)
Elastic Modulus (MPa)
3000
2500
2000
1500
1000
500
0
PMMA
PMMA_m-CNC_0.5%
PMMA_m-CNC_1.0%
PMMA_m-CNC_2.0%
PMMA_um-CNC_0.5%

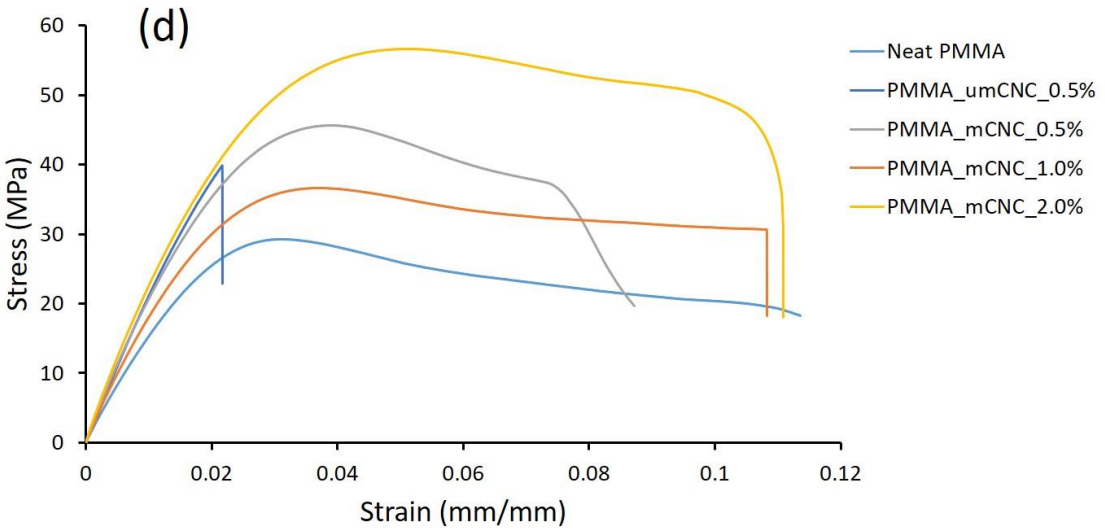

Figure 5.11 (a)The tensile strength, (b) elongation at break, (c) elastic modulus of neat PMMA, and (d) representative stress-strain curves of PMMA/m-CNC (0.5, 1.0 and 2.0%) and PMMA/um-CNC_0.5%. The inset in (a) showed the brittleness of PMMA/um-CNC composite at 2.0% loading.

5.4.3.2 SEM analysis

Both cryo-fracture surface and tensile fracture surface were examined with SEM to reveal the surface morphology and fracture mechanism. As shown in Figure 5.12, all samples have relatively smooth surfaces and debris at the edges of films. This kind of morphology indicates the brittleness of neat PMMA and PMMA composites.[182] It was noted that some micro/sub-micro sized voids were found. Considering those films were prepared by hot-pressing PMMA powders, those voids may result from the hot-pressing procedure, where air was trapped in the polymer matrix. Stress may concentrate around these voids or defects under tensile testing.

Figure 13 showed the tensile fractured surfaces of neat PMMA and composite materials. While PMMA and PMMA_umCNC showed similar fracture surface

morphologies, PMMA_mCNC exhibited interesting features around the micro sized voids. Strong contrasts were observed around voids as showed in the inset of Figure 5.13b. The area near the void showed fibril-like structures pointing out of the fracture surface. The outer area showed a darker color, where fibril-like structures seem to be embedded in the bulk material parallel to the fracture surface. This contrast indicates that the vicinity of the void undergoes ductile deformation before fracture, while the outer area still has brittle fracture behavior. However, similar effect was not observed in neat PMMA or PMMA_umCNC.

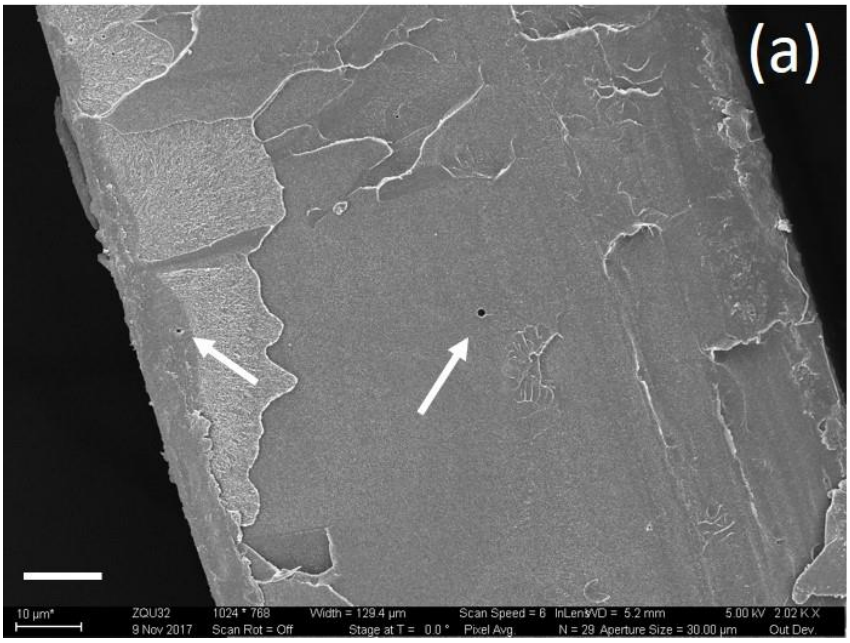

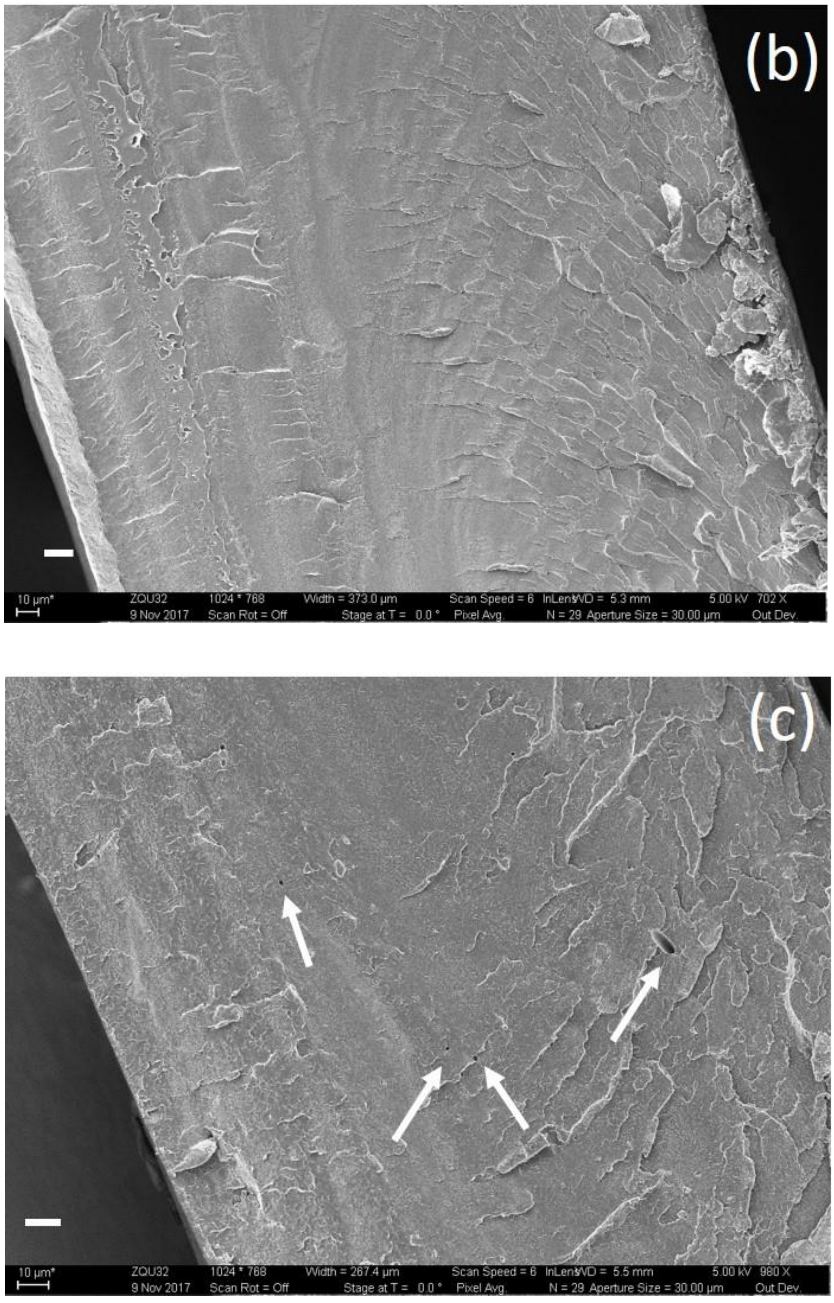

Figure 5.12 SEM images of cryofracture surfaces of (a) neat PMMA, (b) PMMA_mCNC_2.0% and (c) PMMA_umCNC_2.0%. Scale bars are 10µm.

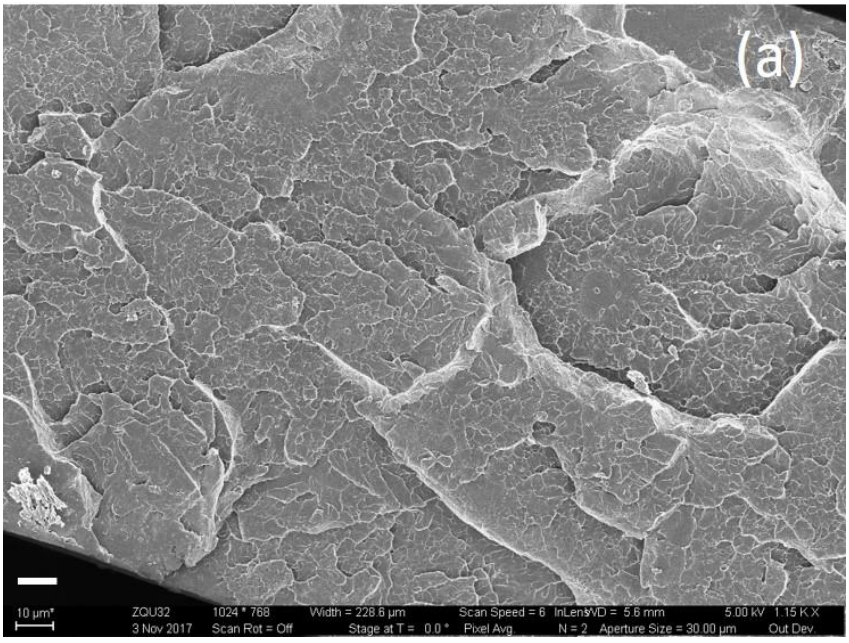
(a)
10 µm*
ZOU32
3 Nov 2017
1024 * 768
Scan Rot = Off
Width = 228.6 µm
Stage at T = 0.0 °
Scan Speed = 6
Pixel Avg.
InLens
N = 2
WD = 5.6 mm
Aperture Size = 30.00 µm
5.00 kV
Out Dev.
1.15 K X

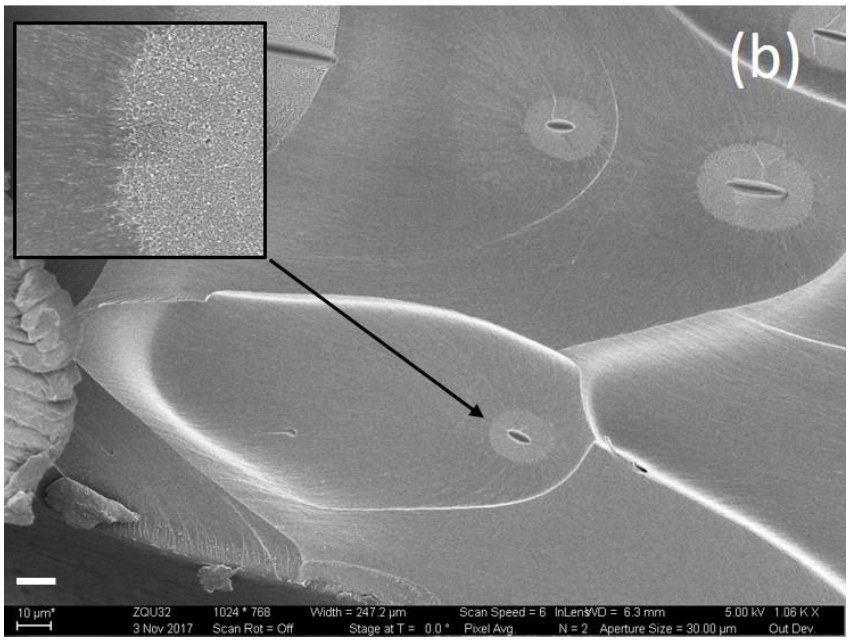
(b)
10 µm*
ZOU32
3 Nov 2017
1024 * 768
Scan Rot = Off
Width = 247.2 µm
Stage at T = 0.0 °
Scan Speed = 6
Pixel Avg.
InLens
N = 2
WD = 6.3 mm
Aperture Size = 30.00 µm
5.00 kV
Out Dev.
1.06 K X

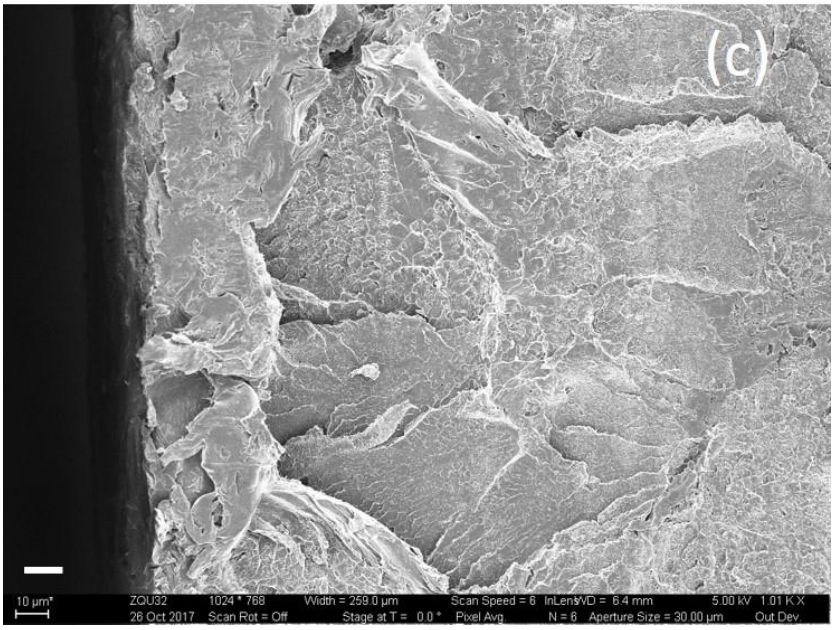

Figure 5.13 SEM images of tensile fracture surfaces of (a) neat PMMA, (b) PMMA_mCNC_2.0% and (c) PMMA_umCNC_2.0%. Scale bars are all 10 µm.

5.5 Conclusion

In this chapter, acrylic functionalized CNCs were first incorporated into PMMA matrix with the solution-casting method to reinforce the mechanical performance. The modified surface chemistry contributed to the enhanced dispersion of m-CNCs in PMMA matrix and improved tensile strength. However, the residual DMF issue associated with the solution-casting method was identified with the results from ATR-FTIR, DSC and TGA. Two alternative processing methods in terms of polymerization and separation were developed and optimized. Although the bulk-pressing method increased the molecular weight of PMMA matrix, significantly reduced the residual DMF, and achieved higher tensile strength, the energy consuming drying process may neutralize these benefits. Meanwhile, the solution-pressing method can effectively remove DMF with a simple precipitation process. The resulted 2.0% m-CNC composite showed an 87.2% increase in

tensile strength compared to the neat PMMA samples. It was surprising that the solution-pressing method achieved the highest tensile strength (53.7 MPa) of m-CNC composite samples with the lowest molecular weight of PMMA (40 kDa), while the solution-casting method gave the highest tensile strength as 26.2 MPa with a M_n of 47 kDa, and the bulk-pressing method gave the highest tensile strength as 49.6 MPa with a M_n of 97 kDa. These results indicated the significant role of the interfacial adhesion in composite materials.

CHAPTER 6. CONCLUSIONS AND RECOMMENDATIONS

6.1 Summary and Conclusions

This work presents new insights for the effects of surface physical (morphology and mechanical property) and chemical properties on particle-particle and particle-matrix adhesion. The results demonstrate the successful completion of the specific objectives outlined in Chapter 1. The key findings for each objective are summarized as follows:

6.1.1 Investigate micro particle-particle adhesion with a complex morphology

In Chapter 2, we successfully quantified the interaction between two sunflower pollens with atomic force microscopy and customized pollen colloidal probes. The interaction between pollen grains showed distinctive behavior, compared with smooth particle-particle interaction or pollen-smooth surface interaction. The wide range of pollen-pollen adhesion force suggested that pollen-pollen adhesion was highly dependent on the spine orientation. Five typical force-distance curves were identified from pollen-pollen interactions, suggesting that multiple adhesion mechanisms may govern the interactions between spiny microparticles.

A hybrid model was developed based the Hamaker approach and Amontons' law of friction to capture the unique pollen-pollen interaction. The Hamaker method was used to calculate the vertical adhesion between spines and bulk pollens as well as the lateral adhesion between two spines. The lateral adhesion was then used as the applied loading to calculate the friction between two spines with Amontons' law. Thus, a combination of adhesion and friction between pollen spines was introduced to explain and predict the

unique interaction behavior, such as reduced force-distance slope and plateau pull-off force upon particle separation.

In addition to the morphology effect, the elastic modulus of micro particles can also influence the interaction forces between complex, spiny particles. For example, the deformation of pollen surface may increase the contact area and lead to larger adhesion. However, the modulus of sporopollenin, the polymer comprising the exine (outer solid shell) of pollens, is rarely reported. In order to characterize the mechanical properties of sporopollenin, pollen exines from three plant species were investigated in Chapter 3, including ragweed (*Ambrosia artemisiifolia*), pecan (*Carya illinoinensis*) and Kentucky bluegrass (*Poa pratensis*). Modulus was determined with atomic force microscopy by using direct nanomechanical mapping of the pollen shell surface. The moduli were atypically high for noncrystalline organic biomaterials, with average values of 16 ± 2.5 GPa (ragweed), 9.5 ± 2.3 GPa (pecan) and 16 ± 4.0 GPa (Kentucky bluegrass). The amorphous pollen exine has a modulus exceeding all non-crystalline biomaterials, such as lignin (6.7 GPa) and actin (1.8 GPa). In addition to native pollens, it is also investigated that the effects of exposure to a common preparative acid-base chemical treatment and elevated humidity on modulus. Acid-base treatment reduced the ragweed modulus by up to 58% and water vapor exposure at 90% relative humidity reduced the modulus by 54% (pecan) and 72% (Kentucky bluegrass). The results suggested that sporopollenin is hard to be deformed by other amorphous biomaterials, which supported the protection function of pollen exnie to mechanical damage. Therefore, the interaction between pollen grains is unlikely to be affected by large deformation.

6.1.2 Investigate nano particle-matrix adhesion with tailored surface chemistry

In Chapter 4, a surface modification route was developed for cellulose nanocrystals to improve the particle-matrix adhesion and compatibility. Freeze dried CNC was modified with IEM to introduce acrylic functional groups on the surface for potential applications with acrylic polymer. The modification process is optimized to achieve a relatively high density of acryloyl groups on CNC surfaces. ATR-FTIR, XPS, solid state ^{13}C NMR and elemental analysis confirmed the attachment of IEM and acrylic groups on CNCs. The surface degree of substitution is determined as between 0.28 and 0.40 based on the results of NMR and elemental analysis. XRD showed a slight decrease in the crystallinity index of CNCs from 91.4% to 72.1% after the modification. TGA showed the enhanced thermal stability with an increased onset temperature of degradation from 214 °C to 252 °C. Finally, the enhanced hydrophobicity of m-CNCs was confirmed with sessile water contact angle measurement, where the contact angle increased from 27 ° to 62 °. The m-CNCs showed better dispersion than um-CNCs in dimethyl formamide (DMF) and formed a clear suspension, while um-CNCs aggregated in DMF and resulted in a turbid suspension. The resulted m-CNC may serve as reinforcing agents in acrylic polymer matrix with improved dispersity and interfacial adhesion.

In Chapter 5, we demonstrated the enhanced interfacial adhesion between the m-CNCs and PMMA matrix with enhanced tensile strength. Both um-CNCs and m-CNCs were incorporated into PMMA matrix to investigate the reinforcement effect of m-CNCs in acrylic polymer. In general, polarized light microscopy (PLM) confirmed the enhanced dispersion of m-CNCs in PMMA matrix, while um-CNCs were visualized as micrometer-sized aggregates. Therefore, PMMA/m-CNC composites retained high light transmission

(> 92%) with 2.0 wt% loading, while PMMA/um-CNC composites exhibited reduced light transmission down to around 75% with the same CNC loading. Three preparation processes of the composites were explored to optimize the mechanical performance of PMMA/CNC composites, including 1) in situ solution polymerization followed by solution casting (solution-casting); 2) in situ bulk polymerization followed by hot pressing (bulk-pressing); 3) in situ solution polymerization followed by precipitation and hot pressing (solution-pressing). The solution-casting route showed a 63.8% increment in tensile strength (26.2 MPa) with m-CNCs at 1.0 wt% loading. However, residual DMF in the composite material compromised the mechanical properties due to its action as a chain transfer agent and plasticizer, which is confirmed with FTIR, thermal gravimetric analysis (TGA), and gel permeation chromatography (GPC). Bulk-pressing reduced the amount of residual DMF and increased the molecular weight, leading to 89.4% higher tensile strength (49.6 MPa) than the solution-casting route at 1.0 wt% loading. However, the dispersion of m-CNCs in the bulk-pressed composites was depressed due to the insufficient compatibility of m-CNCs with the monomer in the initial suspension. The energy-consuming drying process also neutralized some benefits of the bulk-pressing method. The solution-pressing route, compared to the solution-casting method, further removed residual DMF early in the processing (during precipitation and washing), and achieved excellent dispersion of m-CNCs in the PMMA as well. At 2.0 wt% loading modified CNCs increased tensile strength by 87.2% (from 28.7 MPa to 53.7MPa) with the solution-pressing route, which is 8.5% and 117.2% higher than those of the bulk-pressing sample and the solution-casting samples, respectively. It was also surprising that the solution-pressing method achieved the highest tensile strength (53.7 MPa) of m-CNC composite samples with the lowest molecular

weight of PMMA (40 kDa), while the solution-casting method gave the highest tensile strength as 26.2 MPa with a M_n of 47 kDa, and the bulk-pressing method gave the highest tensile strength as 49.6 MPa with a M_n of 97 kDa. These results indicated the significant role of the interfacial adhesion in composite materials. The surface modification method could extend the application of CNCs to more acrylic products.

6.2 Recommendation and future work

Based on the findings of this work, several key scientific questions have been raised. The following sections seeks to provide possible directions for future studies.

6.2.1 Investigate the effect of different morphology on particle-particle adhesion

The first part of this work in pollen-pollen interaction successfully revealed that morphology effect on sunflower pollen interaction. In the preliminary experiments, two configurations, pollen to pollen and pollen (single spine) to flat surface, were compared to reveal the morphology effect. However, these two configurations are not sufficient to comprehensively interpret the morphology effect and the pollen-pollen interaction. In comparison with a flat and smooth surface (roughness<2nm), the substrate pollen not only has the echinate morphology, but also a non-zero curvature as well as a rougher surface between the spines. All characteristics mentioned above are expected to have an influence on the adhesion between pollen grains. To further identify these effects, other configurations need to be considered. The interaction between a pollen and a smooth spherical silica particle could be measured to isolate the effect of the curvature of the core of the pollen compared to the flat surface. Furthermore, pollen grains will also interact with a rough spherical particle. This configuration could reflect the effect of the roughness of

the pollen core on the pollen-pollen interaction. The nanoscale roughness can be fabricated and finely tuned by coating nanoparticles onto a silica microparticle,[183] which could be used to prepared rough particles with a comparable overall size to pollens. By introducing these new configurations of interacting, the morphology effect on the adhesion can be showed with an evolutionary configuration, from pollen-plane interaction, to pollen-smooth spherical microparticle, pollen-rough spherical particle and pollen-pollen interaction.

In addition, to further investigate the effect of the echinate morphology, we can take advantage of the diversity of pollen morphologies. Sunflower pollens have relatively long spines, while there are some species having shorter spines and relatively smaller nanoscale roughness, such as ragweed pollen and olive pollen. The length of spines, the packing density of spines and the overall radius of pollens could be altered by choosing pollens of different species. Characteristic parameters may be introduced to illustrate the echinate morphology such as the spine length, the spacing between spines or the packing density of spines, and the overall radius of the pollen, and to more quantitatively interpret the effect of micro-/nano-structures on the interaction.

6.2.2 Hybrid modification of CNCs

The work in Chapter 4 and Chapter 5 demonstrated the enhanced dispersion of the IEM-modified CNCs and improved interfacial adhesion in PMMA matrix due to the covalent bonds formed at the interfaces. However, the m-CNCs would still form aggregates and turbid suspension when they are dispersed in MMA monomer alone (without DMF) for bulk polymerization. This insufficient dispersity in MMA could be expected, since only

acrylic monomers were grafted onto the CNC surfaces without any long chains facilitating the dispersion. In addition, the degree of substitution is also relatively lower than the other modification method, such as esterification. Esterification is reported to have the highest degree of substitution in the literature.[169] Some esterification of um-CNCs with long alkyl chains can remarkably increase the compatibility with non-polar solvents. The ideal improvement for the work in Chapter 4 and 5 would be having long alkyl chains grafted on um-CNCs at one end, and have acrylic functional group at the other end, as well as a relatively high degree of substitution. However, this kind isocyanate compound is accessible from commercial supplies. An alternative way might be first graft the acrylic group on um-CNCs, then followed by another esterification step to further enhance the hydrophobicity. To the best of our knowledge, this kind of hybrid modification has not been reported for CNCs modification. Several problems may arise with this proposed method. Firstly, the process of the hybrid modification might be tedious, especially if two modification steps need to be done in different phases (organic and aqueous phases). The grafted long alkyl chains may affect the reactivity of the grafted acrylic group due to steric effects.

REFERENCES

(1) Edlund, A. F.; Swanson, R.; Preuss, D., Pollen and Stigma Structure and Function: The Role of Diversity in Pollination. *Plant Cell* **2004,** 16, S84-S97.

(2) Watson, G. S.; Cribb, B. W.; Watson, J. A., Particle Adhesion Measurements on Insect Wing Membranes Using Atomic Force Microscopy. *ISRN Biophysics* **2012,** 2012, 5.

(3) Watson, G. S.; Cribb, B. W.; Schwarzkopf, L.; Watson, J. A., Contaminant Adhesion (Aerial/Ground Biofouling) on the Skin of a Gecko. *Journal of The Royal Society Interface* **2015,** 12, (108).

(4) Beng Joo Reginald, T.; Jung-Hyun, L. E. E.; Carson, M., Characterization of Ragweed Pollen Adhesion to Polyamides and Polystyrene Using Atomic Force Microscopy. *Environmental Science & Technology* **2009,** 43, (12), 4308-4313.

(5) Tsuda, A.; Henry, F. S.; Butler, J. P., Particle Transport and Deposition: Basic Physics of Particle Kinetics. *Comprehensive Physiology* **2013,** 3, (4), 1437-1471.

(6) Williams, D. R., Particle Engineering in Pharmaceutical Solids Processing: Surface Energy Considerations. *Current Pharmaceutical Design* **2015,** 21, (19), 2677-2694.

(7) Santos, A.; Guzmán, R.; Ramirez, Z. Y., Influence on the Wear Resistance of the Particle Size Used in Coatings of Alumina. *Journal of Physics: Conference Series* **2017,** 786, (1), 012012.

(8) Lestiani, R.; Batchelor, W.; Banham, P., Investigation of Lint Particle Adhesion in Offset Printing Using Weibull Statistics. *Journal of Adhesion Science and Technology* **2013,** 27, (4), 339-353.

(9) Fu, S.-Y.; Feng, X.-Q.; Lauke, B.; Mai, Y.-W., Effects of Particle Size, Particle/Matrix Interface Adhesion and Particle Loading on Mechanical Properties of Particulate–Polymer Composites. *Composites Part B: Engineering* **2008,** 39, (6), 933-961.

(10) Bowling, R. A., A Theoretical Review of Particle Adhesion. In *Particles on Surfaces 1: Detection, Adhesion, and Removal*, Mittal, K. L., Ed. Springer US: Boston, MA, 1988; pp 129-142.

(11) Girouard, N. M.; Xu, S.; Schueneman, G. T.; Shofner, M. L.; Meredith, J. C., Site-Selective Modification of Cellulose Nanocrystals with Isophorone Diisocyanate and Formation of Polyurethane-Cnc Composites. *ACS Applied Materials and Interfaces* **2016,** 8, (2), 1458-1467.

(12) Rong, M. Z.; Zhang, M. Q.; Ruan, W. H., Surface Modification of Nanoscale Fillers for Improving Properties of Polymer Nanocomposites: A Review. *Materials Science and Technology* **2006,** 22, (7), 787-796.

(13) Hamaker, H. C., The London—Van Der Waals Attraction between Spherical Particles. *Physica* **1937,** 4, (10), 1058-1072.

(14) Gu, Y.; Li, D., The Van Der Waals Interaction between a Spherical Particle and a Cylinder. *Journal of Colloid and Interface Science* **1999,** 217, (1), 60-69.

(15) Hartmann, U., Van Der Waals Interactions between Sharp Probes and Flat Sample Surfaces. *Phys. Rev. B* **1991,** 43, (3), 2404-2407.

(16) Rafael, T., The London-Van Der Waals Interaction Energy between Objects of Various Geometries. *Journal of Physics: Condensed Matter* **2001,** 13, (9), L195.

(17) Bhagabati, P.; Chaki, T. K.; Khastgir, D., One-Step in Situ Modification of Halloysite Nanotubes: Augmentation in Polymer–Filler Interface Adhesion in Nanocomposites. *Industrial & Engineering Chemistry Research* **2015,** 54, (26), 6698-6712.

(18) Romero-Sánchez, M. D.; Walzak, M. J.; Torregrosa-Maciá, R.; Martín-Martínez, J. M., Surface Modifications and Adhesion of Sbs Rubber Containing Calcium Carbonate Filler by Treatment with Uv Radiation. *International Journal of Adhesion and Adhesives* **2007,** 27, (6), 434-445.

(19) Autumn, K.; Liang, Y. A.; Hsieh, S. T.; Zesch, W.; Chan, W. P.; Kenny, T. W.; Fearing, R.; Full, R. J., Adhesive Force of a Single Gecko Foot-Hair. *Nature* **2000,** 405, (6787), 681-685.

(20) Cai, S.; Bhushan, B., *Meniscus and Viscous Forces During Separation of Hydrophilic and Hydrophobic Smooth/Rough Surfaces with Symmetric and Asymmetric Contact Angles*. 2008; Vol. 366, p 1627-1647.

(21) Izadi, H.; Golmakani, M.; Penlidis, A., Enhanced Adhesion and Friction by Electrostatic Interactions of Double-Level Teflon Nanopillars. *Soft Matter* **2013,** 9, (6), 1985-1996.

(22) Israelachvili, J. N., 6 - Van Der Waals Forces. In *Intermolecular and Surface Forces (Third Edition)*, Israelachvili, J. N., Ed. Academic Press: San Diego, 2011; pp 107-132.

(23) Israelachvili, J. N., Chapter 13 - Van Der Waals Forces between Particles and Surfaces. In *Intermolecular and Surface Forces (Third Edition)*, Israelachvili, J. N., Ed. Academic Press: San Diego, 2011; pp 253-289.

(24) Zhou, Y.; Robinson, A.; Steiner, U.; Federle, W., *Insect Adhesion on Rough Surfaces: Analysis of Adhesive Contact of Smooth and Hairy Pads on Transparent Microstructured Substrates*. 2014; Vol. 11.

(25) Leite, F. L.; Bueno, C. C.; Da Roz, A. L.; Ziemath, E. C.; Oliveira, O. N., Theoretical Models for Surface Forces and Adhesion and Their Measurement Using Atomic Force Microscopy. *Int. J. Mol. Sci.* **2012,** 13, (10), 12773-12856.

(26) Lifshitz, E. M., The Theory of Molecular Attractive Forces between Solids. *Journal Name: Soviet Phys. JETP; Journal Volume: Vol: 2; Other Information: Zhur. Eksptl.' i Teoret. Fiz. 29, 94-110(1955) July. (In Russian). Orig. Receipt Date: 31-DEC-56* **1956**, Medium: X; Size: Pages: 73-83.

(27) Ramakrishna, S. N.; Clasohm, L. Y.; Rao, A.; Spencer, N. D., Controlling Adhesion Force by Means of Nanoscale Surface Roughness. *Langmuir* **2011,** 27, (16), 9972-9978.

(28) You, S.; Wan, M. P., Mathematical Models for the Van Der Waals Force and Capillary Force between a Rough Particle and Surface. *Langmuir* **2013,** 29, (29), 9104-17.

(29) Zhang, D.; Chen, X.-q.; Wang, Y.; Zhang, F.-h.; Gan, Y., Relationship between Asperity-Mediated Surface Forces and Topography Alteration of Silica Microspheres Sliding on Mica, Sapphire, and Glass Substrates under Ambient Conditions: Atomic Force Microscopy and Theoretical Studies. *Langmuir* **2014,** 30, (13), 3729-3740.

(30) Rumpf, H., Die Wissenschaft Des Agglomerierens. *Chem. Ing. Tech.* **1974,** 46, (1), 1-11.

(31) Rabinovich, Y. I.; Adler, J. J.; Ata, A.; Singh, R. K.; Moudgil, B. M., Adhesion between Nanoscale Rough Surfaces: I. Role of Asperity Geometry. *Journal of Colloid and Interface Science* **2000,** 232, (1), 10-16.

(32) Rabinovich, Y. I.; Adler, J. J.; Ata, A.; Singh, R. K.; Moudgil, B. M., Adhesion between Nanoscale Rough Surfaces: Ii. Measurement and Comparison with Theory. *Journal of Colloid and Interface Science* **2000,** 232, (1), 17-24.

(33) Prokopovich, P.; Starov, V., Adhesion Models: From Single to Multiple Asperity Contacts. *Advances in Colloid and Interface Science* **2011,** 168, (1), 210-222.

(34) Derjaguin, B., Untersuchungen Über Die Reibung Und Adhäsion, Iv. *Kolloid-Zeitschrift* **1934,** 69, (2), 155-164.

(35) Johnson, K. L.; Kendall, K.; Roberts, A. D., *Surface Energy and the Contact of Elastic Solids*. 1971; Vol. 324, p 301-313.

(36) Derjaguin, B. V.; Muller, V. M.; Toporov, Y. P., Effect of Contact Deformations on the Adhesion of Particles. *Journal of Colloid and Interface Science* **1975,** 53, (2), 314-326.

(37) Maugis, D., Adhesion of Spheres: The Jkr-Dmt Transition Using a Dugdale Model. *Journal of Colloid and Interface Science* **1992,** 150, (1), 243-269.

(38) Khoshkava, V.; Kamal, M. R., Effect of Surface Energy on Dispersion and Mechanical Properties of Polymer/Nanocrystalline Cellulose Nanocomposites. *Biomacromolecules* **2013,** 14, (9), 3155-3163.

(39) Lee, J.-H.; Thio, B. J. R.; Bae, T.-H.; Meredith, J. C., Role of Lewis Basicity and Van Der Waals Forces in Adhesion of Silica Mfi Zeolites (010) with Polyimides. *Langmuir* **2009,** 25, (16), 9101-9107.

(40) Horn, E., A Summer Hay Fever Plant Survey of Manhattan, Kansas. *Transactions of the Kansas Academy of Science (1903-)* **1933,** 36, 91-97.

(41) Schulte, F.; Lingott, J.; Panne, U.; Kneipp, J., Chemical Characterization and Classification of Pollen. *Analytical Chemistry* **2008,** 80, (24), 9551-9556.

(42) Blackmore, S.; Wortley, A. H.; Skvarla, J. J.; Rowley, J. R., Pollen Wall Development in Flowering Plants. *The New phytologist* **2007,** 174, (3), 483-98.

(43) Travaglini, A.; Ravaziol, D.; Caiola, M. G., A Meteorological Station and a Pollen Trap at the Botanical Garden and Arboretum of the University of Rome Tor Vergata. *Aerobiologia* **2000,** 16, (2), 303-307.

(44) Thio, B. J. R.; Lee, J.-H.; Meredith, J. C., Characterization of Ragweed Pollen Adhesion to Polyamides and Polystyrene Using Atomic Force Microscopy. *Environmental Science & Technology* **2009,** 43, (12), 4308-4313.

(45) Lin, H.; Gomez, I.; Meredith, J. C., Pollenkitt Wetting Mechanism Enables Species-Specific Tunable Pollen Adhesion. *Langmuir* **2013,** 29, (9), 3012-3023.

(46) Lin, H.; Qu, Z.; Meredith, J. C., Pressure Sensitive Microparticle Adhesion through Biomimicry of the Pollen-Stigma Interaction. *Soft Matter* **2016,** 12, (11), 2965-75.

(47) Gomez, I. J.; Goodwin, W. B.; Sabo, D.; Zhang, Z. J.; Sandhage, K. H.; Meredith, J. C., Three-Dimensional Magnetite Replicas of Pollen Particles with Tailorable and Predictable Multimodal Adhesion. *Journal of Materials Chemistry C* **2015,** 3, (3), 632-643.

(48) William Brandon, G.; Donglee, S.; Daniel, S.; SungHwan, H.; Zhang, Z. J.; Meredith, J. C.; Kenneth, H. S., Tunable Multimodal Adhesion of Three-Dimensional, Nanocrystalline $Cofe_2o_4$ Pollen Replicas. *Bioinspiration & Biomimetics* **2017**.

(49) Lin, H.; Allen, M. C.; Wu, J.; deGlee, B. M.; Shin, D.; Cai, Y.; Sandhage, K. H.; Deheyn, D. D.; Meredith, J. C., Bioenabled Core/Shell Microparticles with Tailored Multimodal Adhesion and Optical Reflectivity. *Chemistry of Materials* **2015,** 27, (21), 7321-7330.

(50) Johnstone, L. R.; Gomez, I. J.; Lin, H.; Fadiran, O. O.; Chen, V. W.; Meredith, J. C.; Perry, J. W., Adhesion Enhancements and Surface-Enhanced Raman Scattering Activity

of Ag and Ag@Sio2 Nanoparticle Decorated Ragweed Pollen Microparticle Sensor. *ACS Applied Materials & Interfaces* **2017,** 9, (29), 24804-24811.

(51) Hemsley, A. J.; Ferguson, I. K., Pollen Morphology of the Genus Erythrina (Leguminosae: Papilionoideae) in Relation to Floral Structure and Pollinators. *Annals of the Missouri Botanical Garden* **1985,** 72, (3), 570-590.

(52) Domínguez, E.; Mercado, J. A.; Quesada, M. A.; Heredia, A., Pollen Sporopollenin: Degradation and Structural Elucidation. *Sexual Plant Reproduction* **1999,** 12, (3), 171-178.

(53) Guilford, W. J.; Schneider, D. M.; Labovitz, J.; Opella, S. J., High Resolution Solid State (13)C Nmr Spectroscopy of Sporopollenins from Different Plant Taxa. *Plant Physiology* **1988,** 86, (1), 134-136.

(54) Niester-Nyveld, C.; Haubrich, A.; Kampendonk, H.; Gubatz, S.; Tenberge, K. B.; Rittscher, M.; Wilmesmeier, S.; Wiermann, R., Immunocytochemical Localization of Phenolic Compounds in Pollen Walls Using Antibodies Againstp-Coumaric Acid Coupled to Bovine Serum Albumin. *Protoplasma* **1997,** 197, (3), 148-159.

(55) Ahlers, F.; Lambert, J.; Wiermann, R., Acetylation and Silylation of Piperidine Solubilized Sporopollenin from Pollen of Typha Angustifolia L. *Zeitschrift fur Naturforschung. C, Journal of biosciences* **2003,** 58, (11-12), 807-11.

(56) Bubert, H.; Lambert, J.; Steuernagel, S.; Ahlers, F.; Wiermann, R., Continuous Decomposition of Sporopollenin from Pollen of Typha Angustifolia L. By Acidic Methanolysis. *Zeitschrift fur Naturforschung. C, Journal of biosciences* **2002,** 57, (11-12), 1035-41.

(57) Rozema, J.; Broekman, R. A.; Blokker, P.; Meijkamp, B. B.; de Bakker, N.; van de Staaij, J.; van Beem, A.; Ariese, F.; Kars, S. M., Uv-B Absorbance and Uv-B Absorbing Compounds (Para-Coumaric Acid) in Pollen and Sporopollenin: The Perspective to Track Historic Uv-B Levels. *Journal of Photochemistry and Photobiology B: Biology* **2001,** 62, (1), 108-117.

(58) van Bergen, P. F.; Blokker, P.; Collinson, M. E.; Sinninghe Damsté, J.; de Leeuw, J. W., Structural Biomacromolecules in Plants: What Can Be Learnt from the Fossil Record. *Evolution of plant physiology. Elsevier, Amsterdam* **2004**, 133-154.

(59) Katifori, E.; Alben, S.; Cerda, E.; Nelson, D. R.; Dumais, J., Foldable Structures and the Natural Design of Pollen Grains. *Proceedings of the National Academy of Sciences* **2010,** 107, (17), 7635-7639.

(60) Liu, T.; Zhang, Z., Mechanical Properties of Desiccated Ragweed Pollen Grains Determined by Micromanipulation and Theoretical Modelling. *Biotechnology and Bioengineering* **2004,** 85, (7), 770-775.

(61) Fadiran, O. O.; Meredith, J. C., Surface Treated Pollen Performance as a Renewable Reinforcing Filler for Poly(Vinyl Acetate). *Journal of Materials Chemistry A* **2014,** 2, (40), 17031-17040.

(62) Binnig, G.; Quate, C. F.; Gerber, C., Atomic Force Microscope. *Physical Review Letters* **1986,** 56, (9), 930-933.

(63) Kappl, M.; Butt, H. J., The Colloidal Probe Technique and Its Application to Adhesion Force Measurements. *Particle & Particle Systems Characterization* **2002,** 19, (3), 129-143.

(64) Butt, H.-J.; Cappella, B.; Kappl, M., Force Measurements with the Atomic Force Microscope: Technique, Interpretation and Applications. *Surface Science Reports* **2005,** 59, (1–6), 1-152.

(65) Beck-Candanedo, S.; Roman, M.; Gray, D. G., Effect of Reaction Conditions on the Properties and Behavior of Wood Cellulose Nanocrystal Suspensions. *Biomacromolecules* **2005,** 6, (2), 1048-1054.

(66) Moon, R. J.; Martini, A.; Nairn, J.; Simonsen, J.; Youngblood, J., Cellulose Nanomaterials Review: Structure, Properties and Nanocomposites. *Chemical Society Reviews* **2011,** 40, (7), 3941-3994.

(67) Junior de Menezes, A.; Siqueira, G.; Curvelo, A. A. S.; Dufresne, A., Extrusion and Characterization of Functionalized Cellulose Whiskers Reinforced Polyethylene Nanocomposites. *Polymer* **2009,** 50, (19), 4552-4563.

(68) Bahar, E.; Ucar, N.; Onen, A.; Wang, Y.; Oksüz, M.; Ayaz, O.; Ucar, M.; Demir, A., Thermal and Mechanical Properties of Polypropylene Nanocomposite Materials Reinforced with Cellulose Nano Whiskers. *Journal of Applied Polymer Science* **2012,** 125, (4), 2882-2889.

(69) Wang, T.; Drzal, L. T., Cellulose-Nanofiber-Reinforced Poly(Lactic Acid) Composites Prepared by a Water-Based Approach. *ACS Applied Materials & Interfaces* **2012,** 4, (10), 5079-5085.

(70) Banerjee, M.; Sain, S.; Mukhopadhyay, A.; Sengupta, S.; Kar, T.; Ray, D., Surface Treatment of Cellulose Fibers with Methylmethacrylate for Enhanced Properties of in Situ Polymerized Pmma/Cellulose Composites. *Journal of Applied Polymer Science* **2014,** 131, (2), n/a-n/a.

(71) Xu, S.; Girouard, N.; Schueneman, G.; Shofner, M. L.; Meredith, J. C., Mechanical and Thermal Properties of Waterborne Epoxy Composites Containing Cellulose Nanocrystals. *Polymer* **2013,** 54, (24), 6589-6598.

(72) Girouard, N. M.; Xu, S.; Schueneman, G. T.; Shofner, M. L.; Meredith, J. C., Site-Selective Modification of Cellulose Nanocrystals with Isophorone Diisocyanate and Formation of Polyurethane-Cnc Composites. *ACS Appl Mater Interfaces* **2016,** 8, (2), 1458-67.

(73) Abdul Khalil, H. P. S.; Davoudpour, Y.; Islam, M. N.; Mustapha, A.; Sudesh, K.; Dungani, R.; Jawaid, M., Production and Modification of Nanofibrillated Cellulose Using Various Mechanical Processes: A Review. *Carbohydrate Polymers* **2014,** 99, (Supplement C), 649-665.

(74) Ifuku, S.; Nogi, M.; Abe, K.; Handa, K.; Nakatsubo, F.; Yano, H., Surface Modification of Bacterial Cellulose Nanofibers for Property Enhancement of Optically Transparent Composites: Dependence on Acetyl-Group Ds. *Biomacromolecules* **2007,** 8, (6), 1973-1978.

(75) Mabrouk, A. B.; Salon, M. C. B.; Magnin, A.; Belgacem, M. N.; Boufi, S., Cellulose-Based Nanocomposites Prepared Via Mini-Emulsion Polymerization: Understanding the Chemistry of the Nanocellulose/Matrix Interface. *Colloids and Surfaces A: Physicochemical and Engineering Aspects* **2014,** 448, 1-8.

(76) Siqueira, G.; Bras, J.; Dufresne, A., Cellulose Whiskers Versus Microfibrils: Influence of the Nature of the Nanoparticle and Its Surface Functionalization on the Thermal and Mechanical Properties of Nanocomposites. *Biomacromolecules* **2009,** 10, (2), 425-432.

(77) Nikolaidis, A. K.; Achilias, D. S.; Karayannidis, G. P., Synthesis and Characterization of Pmma/Organomodified Montmorillonite Nanocomposites Prepared by in Situ Bulk Polymerization. *Industrial & Engineering Chemistry Research* **2011,** 50, (2), 571-579.

(78) Khaled, S. M.; Sui, R.; Charpentier, P. A.; Rizkalla, A. S., Synthesis of Tio2−Pmma Nanocomposite: Using Methacrylic Acid as a Coupling Agent. *Langmuir* **2007,** 23, (7), 3988-3995.

(79) Demir, M. M.; Memesa, M.; Castignolles, P.; Wegner, G., Pmma/Zinc Oxide Nanocomposites Prepared by in-Situ Bulk Polymerization. *Macromolecular Rapid Communications* **2006,** 27, (10), 763-770.

(80) Liu, H.; Liu, D.; Yao, F.; Wu, Q., Fabrication and Properties of Transparent Polymethylmethacrylate/Cellulose Nanocrystals Composites. *Bioresource Technology* **2010,** 101, (14), 5685-5692.

(81) Sain, S.; Ray, D.; Mukhopadhyay, A., Improved Mechanical and Moisture Resistance Property of in Situ Polymerized Transparent Pmma/Cellulose Composites. *Polymer Composites* **2015,** 36, (9), 1748-1758.

(82) Terminology for Biorelated Polymers and Applications (Iupac Recommendations 2012). *Pure and Applied Chemistry* **2012,** 84, (2), 377-410.

(83) Liquid–Gas Boundary Catalysis by Using Gold/Polystyrene-Coated Hollow Titania. *Journal of Colloid and Interface Science* **2013,** 394, 490497.

(84) Lu, Z.; Liu, N.; Lee, H.-W.; Zhao, J.; Li, W.; Li, Y.; Cui, Y., Nonfilling Carbon Coating of Porous Silicon Micrometer-Sized Particles for High-Performance Lithium Battery Anodes. *ACS Nano* **2015,** 9, (3), 2540-2547.

(85) Kokkinis, G.; Keplinger, F.; Giouroudi, I., On-Chip Microfluidic Biosensor Using Superparamagnetic Microparticles. *Biomicrofluidics* **2013,** 7, (5), 14.

(86) Kang, M. L.; Ko, J. Y.; Kim, J. E.; Im, G. I., Intra-Articular Delivery of Kartogenin-Conjugated Chitosan Nano/Microparticles for Cartilage Regeneration. *Biomaterials* **2014,** 35, (37), 9984-9994.

(87) Aqel, A.; Yusuf, K.; Alothman, Z. A.; Badjah-Hadj-Ahmed, A. Y., Sporopollenin Microparticle-Based Monolithic Capillary Columns for Liquid Chromatography. *Chromatographia* **2015,** 78, (7-8), 481-486.

(88) Luu, D. T.; Marty-Mazars, D.; Trick, M.; Dumas, C.; Heizmann, P., Pollen-Stigma Adhesion in Brassica Spp Involves Slg and Slr1 Glycoproteins. *The Plant Cell* **1999,** 11, (2), 251-262.

(89) Yu, C.; Ma, J.; Zhang, J.; Lou, J.; Wen, D.; Li, Q., Modulating Particle Adhesion with Micro-Patterned Surfaces. *ACS Appl. Mater. Interfaces* **2014,** 6, (11), 8199-8207.

(90) Hays, D. A., Toner Adhesion. *The Journal of Adhesion* **1995,** 51, (1-4), 41-48.

(91) Rimai, D. S.; Dejesus, M. C.; Weiss, D. S., The Effect of Surface-Adhering Nanoclusters on the Adhesion and Cohesion of Micrometer-Size Particles. *Journal of Adhesion Science and Technology* **2008,** 22, (5-6), 529-543.

(92) Götzinger, M.; Peukert, W., Particle Adhesion Force Distributions on Rough Surfaces. *Langmuir* **2004,** 20, (13), 5298-5303.

(93) Brambilla, S.; Speckart, S.; Brown, M. J., Adhesion and Aerodynamic Forces for the Resuspension of Non-Spherical Particles in Outdoor Environments. *Journal of Aerosol Science* **2017,** 112, (Supplement C), 52-67.

(94) Decuzzi, P.; Ferrari, M., The Adhesive Strength of Non-Spherical Particles Mediated by Specific Interactions. *Biomaterials* **2006,** 27, (30), 5307-5314.

(95) Rabinovich, Y. I.; Adler, J. J.; Esayanur, M. S.; Ata, A.; Singh, R. K.; Moudgil, B. M., Capillary Forces between Surfaces with Nanoscale Roughness. *Advances in Colloid and Interface Science* **2002,** 96, (1–3), 213-230.

(96) Heim, L. O.; Ecke, S.; Preuss, M.; Butt, H. J., Adhesion Forces between Individual Gold and Polystyrene Particles. *Journal of Adhesion Science and Technology* **2002,** 16, (7), 829-843.

(97) Jallo, L. J.; Chen, Y.; Bowen, J.; Etzler, F.; Dave, R., Prediction of Inter-Particle Adhesion Force from Surface Energy and Surface Roughness. *Journal of Adhesion Science and Technology* **2011,** 25, (4-5), 367-384.

(98) Kumar, A.; Staedler, T.; Jiang, X., Role of Relative Size of Asperities and Adhering Particles on the Adhesion Force. *J Colloid Interface Sci* **2013,** 409, 211-8.

(99) Wang, L. M.; McCarthy, T. J., Capillary-Bridge-Derived Particles with Negative Gaussian Curvature. *Proc. Natl. Acad. Sci. U. S. A.* **2015,** 112, (9), 2664-2669.

(100) Pang, C.; Kim, T. I.; Bae, W. G.; Kang, D.; Kim, S. M.; Suh, K. Y., Bioinspired Reversible Interlocker Using Regularly Arrayed High Aspect-Ratio Polymer Fibers. *Advanced materials (Deerfield Beach, Fla.)* **2012,** 24, (4), 475-9.

(101) Lee, C.; Kim, S. M.; Kim, Y. J.; Choi, Y. W.; Suh, K. Y.; Pang, C.; Choi, M., Robust Microzip Fastener: Repeatable Interlocking Using Polymeric Rectangular Parallelepiped Arrays. *Acs Applied Materials & Interfaces* **2015,** 7, (4), 2561-2568.

(102) Champion, J. A.; Mitragotri, S., Role of Target Geometry in Phagocytosis. *Proc. Natl. Acad. Sci. U. S. A.* **2006,** 103, (13), 4930-4934.

(103) Heidi, E. M. D., Survey of Pollen and Pollenkitt Lipids -- Chemical Cues to Flower Visitors? *American Journal of Botany* **1988,** 75, (2), 170-182.

(104) Burnham, N. A.; Chen, X.; Hodges, C. S.; Matei, G. A.; Thoreson, E. J.; Roberts, C. J.; Davies, M. C.; Tendler, S. J. B., Comparison of Calibration Methods for Atomic-Force Microscopy Cantilevers. *Nanotechnology* **2003,** 14, (1), 1.

(105) Hutter, J. L.; Bechhoefer, J., Calibration of Atomic - Force Microscope Tips. *Review of Scientific Instruments* **1993,** 64, (7), 1868-1873.

(106) Heim, L. O.; Blum, J.; Preuss, M.; Butt, H. J., Adhesion and Friction Forces between Spherical Micrometer-Sized Particles. *Physical Review Letters* **1999,** 83, (16), 3328-3331.

(107) Rahe, P.; Bechstein, R.; Kühnle, A., Vertical and Lateral Drift Corrections of Scanning Probe Microscopy Images. *Journal of Vacuum Science & Technology B, Nanotechnology and Microelectronics: Materials, Processing, Measurement, and Phenomena* **2010,** 28, (3), C4E31-C4E38.

(108) Bergström, L., Hamaker Constants of Inorganic Materials. *Advances in Colloid and Interface Science* **1997,** 70, (0), 125-169.

(109) Israelachvili, J. N., 10 - Unifying Concepts in Intermolecular and Interparticle Forces. In *Intermolecular and Surface Forces (Third Edition)*, Israelachvili, J. N., Ed. Academic Press: San Diego, 2011; pp 191-204.

(110) Diego-Taboada, A.; Beckett, S.; Atkin, S.; Mackenzie, G., Hollow Pollen Shells to Enhance Drug Delivery. *Pharmaceutics* **2014,** 6, (1), 80-96.

(111) Piffanelli, P.; Ross, J. H. E.; Murphy, D. J., Biogenesis and Function of the Lipidic Structures of Pollen Grains. *Sexual Plant Reproduction* **1998,** 11, (2), 65-80.

(112) Brooks, J.; Shaw, G., Sporopollenin: A Review of Its Chemistry, Palaeochemistry and Geochemistry. *Grana* **1978,** 17, (2), 91-97.

(113) Mackenzie, G.; Boa, A. N.; Diego-Taboada, A.; Atkin, S. L.; Sathyapalan, T., Sporopollenin, the Least Known yet Toughest Natural Biopolymer. *Frontiers in Materials* **2015,** 2, (66), 1-5.

(114) Chiappe, C.; Demontis, G. C.; Di Bussolo, V.; Rodriguez Douton, M. J.; Rossella, F.; Pomelli, C. S.; Sartini, S.; Caporali, S., From Pollen Grains to Functionalized Microcapsules: A Facile Chemical Route Using Ionic Liquids. *Green Chemistry* **2017,** 19, (4), 1028-1033.

(115) Heinz, W. F.; Hoh, J. H., Spatially Resolved Force Spectroscopy of Biological Surfaces Using the Atomic Force Microscope. *Trends in Biotechnology* **1999,** 17, (4), 143-150.

(116) Gaboriaud, F.; Parcha, B. S.; Gee, M. L.; Holden, J. A.; Strugnell, R. A., Spatially Resolved Force Spectroscopy of Bacterial Surfaces Using Force-Volume Imaging. *Colloids and Surfaces B: Biointerfaces* **2008,** 62, (2), 206-213.

(117) Rosa-Zeiser, A.; Weilandt, E.; Hild, S.; Marti, O., The Simultaneous Measurement of Elastic, Electrostatic and Adhesive Properties by Scanning Force Microscopy: Pulsed-Force Mode Operation. *Measurement Science and Technology* **1997,** 8, (11), 1333.

(118) Pittenger, B.; Erina, N.; Su, C., Quantitative Mechanical Property Mapping at the Nanoscale with Peakforce Qnm. *Application Note Veeco Instruments Inc* **2010**.

(119) Hu, Y.; Hu, S.; Su, C.; Shi, J.; Ma, J., Method and Apparatus of Operating a Scanning Probe Microscope. In Google Patents: 2011.

(120) Heu, C.; Berquand, A.; Elie-Caille, C.; Nicod, L., Glyphosate-Induced Stiffening of Hacat Keratinocytes, a Peak Force Tapping Study on Living Cells. *Journal of Structural Biology* **2012,** 178, (1), 1-7.

(121) Pletikapić, G.; Berquand, A.; Radić, T. M.; Svetličić, V., Quantitative Nanomechanical Mapping of Marine Diatom in Seawater Using Peak Force Tapping Atomic Force Microscopy. *Journal of Phycology* **2012,** 48, (1), 174-185.

(122) Xavier, P.; Bose, S., Nanomechanical Mapping, Hierarchical Polymer Dynamics, and Miscibility in the Presence of Chain-End Grafted Nanoparticles. *Macromolecules* **2016,** 49, (3), 1036-1048.

(123) Wengui Li, J. X., Shiho Kawashima, Gajendra S. Shekhawat,; Shah, S. P., Experimental Investigation on Quantitative Nanomechanical Properties of Cement Paste. *Materials Journal* **2015,** 112, (2).

(124) Morales-Rivas, L.; González-Orive, A.; Garcia-Mateo, C.; Hernández-Creus, A.; Caballero, F. G.; Vázquez, L., Nanomechanical Characterization of Nanostructured Bainitic Steel: Peak Force Microscopy and Nanoindentation with Afm. *Scientific Reports* **2015,** 5, 17164.

(125) Ducker, W. A.; Senden, T. J.; Pashley, R. M., Direct Measurement of Colloidal Forces Using an Atomic Force Microscope. *Nature* **1991,** 353, (6341), 239-241.

(126) Smolyakov, G.; Pruvost, S.; Cardoso, L.; Alonso, B.; Belamie, E.; Duchet-Rumeau, J., Afm Peakforce Qnm Mode: Evidencing Nanometre-Scale Mechanical Properties of Chitin-Silica Hybrid Nanocomposites. *Carbohydrate Polymers* **2016,** 151, 373-380.

(127) Hopcroft, M. A.; Nix, W. D.; Kenny, T. W., What Is the Young's Modulus of Silicon? *Journal of Microelectromechanical Systems* **2010,** 19, (2), 229-238.

(128) Sader, J. E.; Chon, J. W. M.; Mulvaney, P., Calibration of Rectangular Atomic Force Microscope Cantilevers. *Review of Scientific Instruments* **1999,** 70, (10), 3967-3969.

(129) Song, Y.; Wu, S.; Xu, L.; Fu, X., Accurate Calibration and Uncertainty Estimation of the Normal Spring Constant of Various Afm Cantilevers. *Sensors (Basel, Switzerland)* **2015,** 15, (3), 5865-5883.

(130) Dokukin, M. E.; Sokolov, I., Quantitative Mapping of the Elastic Modulus of Soft Materials with Harmonix and Peakforce Qnm Afm Modes. *Langmuir* **2012,** 28, (46), 16060-16071.

(131) Kalpakjian, S.; Schmid, S., Manufacturing Processes for Engineering Materials–5th Edition. *agenda* **2014,** 12, 1.

(132) Ulusoy, E.; Kolayli, S., Phenolic Composition and Antioxidant Properties of Anzer Bee Pollen. *Journal of Food Biochemistry* **2014,** 38, (1), 73-82.

(133) Bal, S.; Behera, R., Structural Investigation of Chemical Treated Polyester Fibers Using Saxs and Other Techniques. *Journal of Minerals and Materials Characterization and Engineering* **2006,** 5, (2), 179-198.

(134) Lin, H.; Lizarraga, L.; Bottomley, L. A.; Carson Meredith, J., Effect of Water Absorption on Pollen Adhesion. *Journal of Colloid and Interface Science* **2015,** 442, (0), 133-139.

(135) Weeks, B. L.; Vaughn, M. W.; DeYoreo, J. J., Direct Imaging of Meniscus Formation in Atomic Force Microscopy Using Environmental Scanning Electron Microscopy. *Langmuir* **2005,** 21, (18), 8096-8098.

(136) Wang, Y.; Len, T.; Huang, Y.; Diego Taboada, A.; Boa, A. N.; Ceballos, C.; Delbecq, F.; Mackenzie, G.; Len, C., Sulfonated Sporopollenin as an Efficient and Recyclable Heterogeneous Catalyst for Dehydration of D-Xylose and Xylan into Furfural. *ACS Sustainable Chemistry & Engineering* **2017,** 5, (1), 392-398.

(137) Kojima, H.; Ishijima, A.; Yanagida, T., Direct Measurement of Stiffness of Single Actin Filaments with and without Tropomyosin by in Vitro Nanomanipulation. *Proceedings of the National Academy of Sciences* **1994,** 91, (26), 12962-12966.

(138) Gittes, F.; Mickey, B.; Nettleton, J.; Howard, J., Flexural Rigidity of Microtubules and Actin Filaments Measured from Thermal Fluctuations in Shape. *The Journal of cell biology* **1993,** 120, (4), 923-34.

(139) Cousins, W., Elastic Modulus of Lignin as Related to Moisture Content. *Wood science and technology* **1976,** 10, (1), 9-17.

(140) Höije, A.; Gröndahl, M.; Tømmeraas, K.; Gatenholm, P., Isolation and Characterization of Physicochemical and Material Properties of Arabinoxylans from Barley Husks. *Carbohydrate Polymers* **2005,** 61, (3), 266-275.

(141) Zhang, P.; Whistler, R. L., Mechanical Properties and Water Vapor Permeability of Thin Film from Corn Hull Arabinoxylan. *Journal of applied polymer science* **2004,** 93, (6), 2896-2902.

(142) Skendi, A.; Biliaderis, C.; Lazaridou, A.; Izydorczyk, M., Structure and Rheological Properties of Water Soluble B-Glucans from Oat Cultivars of Avena Sativa and Avena Bysantina. *Journal of Cereal Science* **2003,** 38, (1), 15-31.

(143) van der Rijt, J. A.; van der Werf, K. O.; Bennink, M. L.; Dijkstra, P. J.; Feijen, J., Micromechanical Testing of Individual Collagen Fibrils. *Macromolecular bioscience* **2006,** 6, (9), 697-702.

(144) Buehler, M. J., Nano-and Micromechanical Properties of Hierarchical Biological Materials and Tissues. *Journal of Materials Science* **2007,** 42, (21), 8765-8770.

(145) Siqueira, G.; Bras, J.; Dufresne, A., Cellulosic Bionanocomposites: A Review of Preparation, Properties and Applications. *Polymers* **2010,** 2, (4), 728.

(146) Patricio, P. S. D.; Pereira, I. M.; da Silva, N. C. F.; Ayres, E.; Pereira, F. V.; Orefice, R. L., Tailoring the Morphology and Properties of Waterborne Polyurethanes by the Procedure of Cellulose Nanocrystal Incorporation. *Eur Polym J* **2013,** 49, (12), 3761-3769.

(147) Wu, G. M.; Liu, D.; Liu, G. F.; Chen, J.; Huo, S. P.; Kong, Z. W., Thermoset Nanocomposites from Waterborne Bio-Based Epoxy Resin and Cellulose Nanowhiskers. *Carbohyd Polym* **2015,** 127, 229-235.

(148) Girouard, N.; Schueneman, G. T.; Shofner, M. L.; Meredith, J. C., Exploiting Colloidal Interfaces to Increase Dispersion, Performance, and Pot-Life in Cellulose Nanocrystal/Waterborne Epoxy Composites. *Polymer* **2015,** 68, 111-121.

(149) Girouard, N. M.; Xu, S. H.; Shofner, M. L.; Meredith, J. C., Thermal Stability and Mechanical Reinforcement of Cellulose Nanocrystal/Waterborne Epoxy Composites. *Abstr Pap Am Chem S* **2014,** 247.

(150) Xu, S. H.; Girouard, N.; Schueneman, G.; Shofner, M. L.; Meredith, J. C., Mechanical and Thermal Properties of Waterborne Epoxy Composites Containing Cellulose Nanocrystals. *Polymer* **2013,** 54, (24), 6589-6598.

(151) Veigel, S.; Grull, G.; Pinkl, S.; Obersriebnig, M.; Muller, U.; Gindl-Altmutter, W., Improving the Mechanical Resistance of Waterborne Wood Coatings by Adding Cellulose Nanofibres. *React Funct Polym* **2014,** 85, 214-220.

(152) Tan, Y.; Liu, Y.; Chen, W.; Liu, Y.; Wang, Q.; Li, J.; Yu, H., Homogeneous Dispersion of Cellulose Nanofibers in Waterborne Acrylic Coatings with Improved Properties and Unreduced Transparency. *ACS Sustainable Chemistry and Engineering* **2016**, in press.

(153) Vardanyan, V.; Poaty, B.; Chauve, G.; Landry, V.; Galstian, T.; Riedl, B., Mechanical Properties of Uv-Waterborne Varnishes Reinforced by Cellulose Nanocrystals. *J Coat Technol Res* **2014,** 11, (6), 841-852.

(154) Gaylord, N. G., Compatibilization of Polymers by Adding Graft Copolymers. In Google Patents: 1969.

(155) Hu, Z.; Cranston, E., Surface Modification of Cellulose Nanocrystals. In Google Patents: 2015.

(156) HAMAD, W. Y.; Su, S., Thermoplastic Nanocomposite Material Based on Nanocrystalline Cellulose (Ncc). In Google Patents: 2013.

(157) Hamad, W. Y.; Su, S., Ncc-Based Supramolecular Materials for Thermoplastic and Thermoset Polymer Composites. In Google Patents: 2013.

(158) Kedzior, S. A.; Graham, L.; Moorlag, C.; Dooley, B. M.; Cranston, E. D., Poly(Methyl Methacrylate)-Grafted Cellulose Nanocrystals: One-Step Synthesis, Nanocomposite Preparation, and Characterization. *The Canadian Journal of Chemical Engineering* **2016,** 94, (5), 811-822.

(159) Dooley, B. M.; Qi, Y.; Moorlag, C.; Zhang, Q., Methods for Preparing Reinforced Fluoropolymer Composites Comprising Surface Functionalized Nanocrystalline Cellulose. In Google Patents: 2014.

(160) Goussé, C.; Chanzy, H.; Excoffier, G.; Soubeyrand, L.; Fleury, E., Stable Suspensions of Partially Silylated Cellulose Whiskers Dispersed in Organic Solvents. *Polymer* **2002,** 43, (9), 2645-2651.

(161) Massonne, K.; Stegmann, V.; D'andola, G.; Mormann, W.; Wezstein, M.; Leng, W., Process for Silylating Cellulose. In Google Patents: 2009.

(162) Kimura, S.; Imoto, M., Polymerization of Acrylonitrile by Ceric Salt in the Presence of Starch. Vinyl Polymerization. L1. *Die Makromolekulare Chemie* **1960,** 42, (1), 140-150.

(163) Gårdebjer, S.; Bergstrand, A.; Idström, A.; Börstell, C.; Naana, S.; Nordstierna, L.; Larsson, A., Solid-State Nmr to Quantify Surface Coverage and Chain Length of Lactic Acid Modified Cellulose Nanocrystals, Used as Fillers in Biodegradable Composites. *Composites Science and Technology* **2015,** 107, (Supplement C), 1-9.

(164) Peng, Y.; Gardner, D. J.; Han, Y.; Kiziltas, A.; Cai, Z.; Tshabalala, M. A., Influence of Drying Method on the Material Properties of Nanocellulose I: Thermostability and Crystallinity. *Cellulose* **2013,** 20, (5), 2379-2392.

(165) Hu, Z.; Berry, R. M.; Pelton, R.; Cranston, E. D., One-Pot Water-Based Hydrophobic Surface Modification of Cellulose Nanocrystals Using Plant Polyphenols. *ACS Sustainable Chemistry & Engineering* **2017,** 5, (6), 5018-5026.

(166) Cui, J.; Campo, A. d., Multivalent H-Bonds for Self-Healing Hydrogels. *Chemical Communications* **2012,** 48, (74), 9302-9304.

(167) Capitani, D.; Porro, F.; Segre, A. L., High Field Nmr Analysis of the Degree of Substitution in Carboxymethyl Cellulose Sodium Salt. *Carbohydrate Polymers* **2000,** 42, (3), 283-286.

(168) Siqueira, G.; Bras, J.; Dufresne, A., New Process of Chemical Grafting of Cellulose Nanoparticles with a Long Chain Isocyanate. *Langmuir* **2010,** 26, (1), 402-411.

(169) Eyley, S.; Thielemans, W., Surface Modification of Cellulose Nanocrystals. *Nanoscale* **2014,** 6, (14), 7764-7779.

(170) Kargarzadeh, H.; M. Sheltami, R.; Ahmad, I.; Abdullah, I.; Dufresne, A., Cellulose Nanocrystal: A Promising Toughening Agent for Unsaturated Polyester Nanocomposite. *Polymer* **2015,** 56, (Supplement C), 346-357.

(171) Segal, L.; Creely, J. J.; A.E. Martin, J.; Conrad, C. M., An Empirical Method for Estimating the Degree of Crystallinity of Native Cellulose Using the X-Ray Diffractometer. *Textile Research Journal* **1959,** 29, (10), 786-794.

(172) Ayre, D. S.; Bucknall, C. B., Particle Cavitation in Rubber-Toughened Pmma: Experimental Testing of the Energy-Balance Criterion. *Polymer* **1998,** 39, (20), 4785-4791.

(173) Maeda, S.; Fujita, M.; Idota, N.; Matsukawa, K.; Sugahara, Y., Preparation of Transparent Bulk Tio2/Pmma Hybrids with Improved Refractive Indices Via an in Situ Polymerization Process Using Tio2 Nanoparticles Bearing Pmma Chains Grown by Surface-Initiated Atom Transfer Radical Polymerization. *ACS Applied Materials & Interfaces* **2016,** 8, (50), 34762-34769.

(174) Nussbaumer, R. J.; Caseri, W. R.; Smith, P.; Tervoort, T., Polymer-Tio2 Nanocomposites: A Route Towards Visually Transparent Broadband Uv Filters and High Refractive Index Materials. *Macromolecular Materials and Engineering* **2003,** 288, (1), 44-49.

(175) Chen, L.-S.; Huang, Z.-M.; Dong, G.-H.; He, C.-L.; Liu, L.; Hu, Y.-Y.; Li, Y., Development of a Transparent Pmma Composite Reinforced with Nanofibers. *Polymer Composites* **2009,** 30, (3), 239-247.

(176) Tang, E.; Cheng, G.; Ma, X., Preparation of Nano-Zno/Pmma Composite Particles Via Grafting of the Copolymer onto the Surface of Zinc Oxide Nanoparticles. *Powder Technology* **2006,** 161, (3), 209-214.

(177) Ben Mabrouk, A.; Kaddami, H.; Magnin, A.; Belgacem, M. N.; Dufresne, A.; Boufi, S., Preparation of Nanocomposite Dispersions Based on Cellulose Whiskers and Acrylic Copolymer by Miniemulsion Polymerization: Effect of the Silane Content. *Polymer Engineering & Science* **2011,** 51, (1), 62-70.

(178) Kedzior, S. A.; Marway, H. S.; Cranston, E. D., Tailoring Cellulose Nanocrystal and Surfactant Behavior in Miniemulsion Polymerization. *Macromolecules* **2017,** 50, (7), 2645-2655.

(179) Spasojevic, P.; Zrilic, M.; Panic, V.; Stamenkovic, D.; Seslija, S.; Velickovic, S., The Mechanical Properties of a Poly(Methyl Methacrylate) Denture Base Material Modified with Dimethyl Itaconate and Di-N-Butyl Itaconate. *International Journal of Polymer Science* **2015,** 2015, 9.

(180) Cheng, W. M.; Miller, G. A.; Manson, J. A.; Hertzberg, R. W.; Sperling, L. H., Mechanical Behaviour of Poly(Methyl Methacrylate). *Journal of Materials Science* **1990,** 25, (4), 1917-1923.

(181) Eriksson, M.; Goossens, H.; Peijs, T., Influence of Drying Procedure on Glass Transition Temperature of Pmma Based Nanocomposites. *Nanocomposites* **2015,** 1, (1), 36-45.

(182) Yu Zhang, Y.-y. C., Li Huang, Zhi-guo Chai, Li-juan Shen & Yu-hong Xiao, The Antifungal Effects and Mechanical Properties of Silver Bromide/Cationic Polymer Nano-Composite-Modified Poly-Methyl Methacrylate-Based Dental Resin. *Scientific Reports* **2017,** 7.

(183) San-Miguel, A.; Behrens, S. H., Influence of Nanoscale Particle Roughness on the Stability of Pickering Emulsions. *Langmuir* **2012,** 28, (33), 12038-12043.